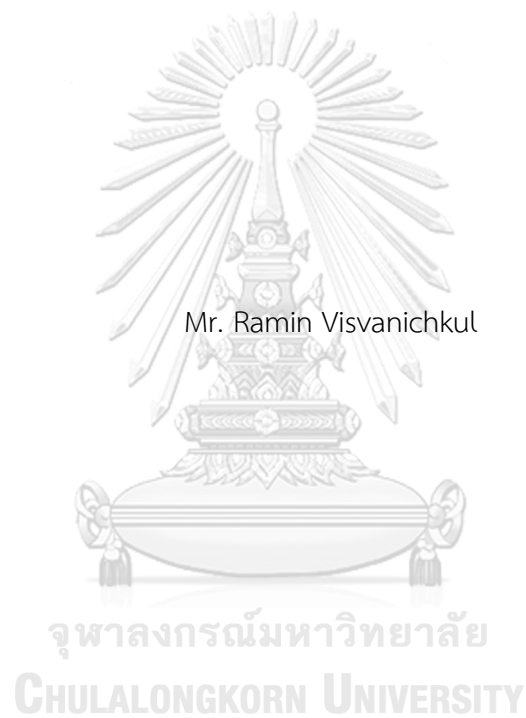


Fabrication and electrochemical performance of nickel-alloy-foam-supported solid
oxide electrolysis cell for hydrogen production from steam



A Thesis Submitted in Partial Fulfillment of the Requirements
for the Degree of Master of Engineering in Chemical Engineering

Department of Chemical Engineering

FACULTY OF ENGINEERING

Chulalongkorn University

Academic Year 2019

Copyright of Chulalongkorn University

การขึ้นรูปและความสามารถทางไฟฟ้าเคมีของเซลล์อิเล็กโทรไลซิสแบบออกไซด์ของแข็งที่มีโพรมานิก
เกิลอัลลอยด์เป็นตัวรองรับเพื่อการผลิตไฮโดรเจนจากไอน้ำ



วิทยานิพนธ์นี้เป็นส่วนหนึ่งของการศึกษาตามหลักสูตรปริญญาวิศวกรรมศาสตรมหาบัณฑิต
สาขาวิชาวิศวกรรมเคมี ภาควิชาวิศวกรรมเคมี
คณะวิศวกรรมศาสตร์ จุฬาลงกรณ์มหาวิทยาลัย
ปีการศึกษา 2562
ลิขสิทธิ์ของจุฬาลงกรณ์มหาวิทยาลัย

Thesis Title	Fabrication and electrochemical performance of nickel-alloy-foam-supported solid oxide electrolysis cell for hydrogen production from steam
By	Mr. Ramin Visvanichkul
Field of Study	Chemical Engineering
Thesis Advisor	Assistant Professor Pattaraporn Kim, Ph.D.

Accepted by the FACULTY OF ENGINEERING, Chulalongkorn University in Partial Fulfillment of the Requirement for the Master of Engineering

----- Dean of the FACULTY OF ENGINEERING
(Professor SUPOT TEACHAVORASINSKUN)

THESIS COMMITTEE

----- Chairman
(Associate Professor KASIDIT NOOTONG)

----- Thesis Advisor
(Assistant Professor Pattaraporn Kim, Ph.D.)

----- Examiner
(Professor SUTTICHAJ ASSABUMRUNGRAT)

----- External Examiner
(Pramote Puengjinda)

จุฬาลงกรณ์มหาวิทยาลัย
CHULALONGKORN UNIVERSITY

รามิล วิศวะวานิชย์กุล : การขึ้นรูปและความสามารถทางไฟฟ้าเคมีของเซลล์อิเล็กโทรไลซิสแบบออกไซด์ของแข็งที่มีโฟม निकเกิลอัลลอยด์เป็นตัวรองรับเพื่อการผลิตไฮโดรเจนจากไอน้ำ. (Fabrication and electrochemical performance of nickel-alloy-foam-supported solid oxide electrolysis cell for hydrogen production from steam) อ.ที่ปรึกษาหลัก : ผศ. ดร.ภัทรพร คิม

CuO ร้อยละ 0.5 โดยน้ำหนัก ถูกใช้เป็นสารช่วยเผาผนึกในกระบวนการเผาผนึกอิเล็กโทรไลต์ชนิด $Sc_{0.1}Ce_{0.05}Gd_{0.05}Zr_{0.85}O_2$ (SCGZ) สำหรับเซลล์อิเล็กโทรไลซิสแบบออกไซด์ของแข็งโดยมีอิเล็กโทรไลต์เป็นตัวรองรับ (Pt/SCGZ/Pt) จากการศึกษาผลการเติม CuO เป็นสารช่วยเผาผนึกอันได้แก่ การเปลี่ยนแปลงวัฏภาคของแข็งในโครงสร้างผลึก ความหนาแน่นสัมพัทธ์และค่าการนำไฟฟ้าของเซลล์ไฟฟ้าเคมีภายหลังการเผาผนึกอุณหภูมิต่างๆกัน (1373 -1673 K) เป็นเวลา 4 ชั่วโมง พบว่าการเติมสารช่วยเผาผนึกดังกล่าวส่งผลต่อการเผาผนึกของ SCGZ อย่างมีนัยสำคัญ กล่าวคือ เซลล์ไฟฟ้าเคมีแสดงความหนาแน่นสัมพัทธ์สูงถึง ร้อยละ 95 ณ อุณหภูมิการเผาผนึก 1573 K ในขณะที่ SCGZ ที่ไม่มีการเติมสารช่วยเผาผนึกให้ความหนาแน่นสัมพัทธ์ต่ำ แม้ว่าการเผาผนึกถูกดำเนินการ ณ อุณหภูมิสูง 1673 K ในขณะที่โครงสร้างผลึกภายหลังการเผา SCGZ โดยการเติม CuO ไม่พบการปนเปื้อนของวัฏภาคแปลกปลอมในโครงสร้างผลึก อีกทั้งการประเมินความสามารถทางไฟฟ้าเคมีที่อุณหภูมิการทำงาน 873 K ถึง 1173 K ภายใต้อัตราส่วนไอน้ำต่อไฮโดรเจนที่ 70:30 พบว่าการใช้ CuO ร้อยละ 0.5 โดยน้ำหนัก ไม่ส่งผลต่อความสามารถทางไฟฟ้าเคมีของเซลล์ โดยพลังงานกระตุ้นของการนำไฟฟ้า (E_a) ของเซลล์ SCGZ และ SCGZ ที่มีการใช้ CuO มีค่าเท่ากับ 72.34 kJmol^{-1} และ 74.93 kJmol^{-1} ตามลำดับ ภายหลังการศึกษานิกเกิลอิเล็กโทรไลต์ชนิด SCGZ ที่มีการเติม CuO เป็นสารช่วยเผาผนึกถูกนำมาใช้งานในการขึ้นรูปเซลล์อิเล็กโทรไลซิสแบบออกไซด์ของแข็งที่มีโฟม निकเกิลอัลลอยด์ชนิด निकเกิลเหล็ก (Ni-Fe) ที่ความพรุน 5-130 ppi เป็นตัวรองรับเพื่อการผลิตไฮโดรเจนจากไอน้ำโดยมี Ni-SCGZ และ $Ba_{0.5}Sr_{0.5}Co_{0.8}Fe_{0.2}O_{3-\delta}$ (BSCF) เป็นชั้นแคโทดและแอโนด ตามลำดับ การขึ้นรูปเซลล์ไฟฟ้าเคมีบนตัวรองรับดังกล่าวใช้วิธีการชุบเคลือบแบบเปียกด้วยสารละลายต่างๆ โดยชั้นแคโทดถูกขึ้นรูปด้วยสารละลายแคโทดที่มีความหนืดและค่าสัมประสิทธิ์การขยายตัวทางความร้อนไล่ระดับตามลำดับการชุบเคลือบ ภายหลังการชุบเคลือบชั้นแคโทด ชิ้นงานดังกล่าวถูกนำไปเผาที่อุณหภูมิ 1373 K เป็นเวลา 2 ชั่วโมง จากนั้นชิ้นงานจะถูกชุบเคลือบแบบจุ่มด้วยสารละลายอิเล็กโทรไลต์ตามด้วยการเผาผนึกที่อุณหภูมิ 1623 K เป็นเวลา 4 ชั่วโมง ด้วยกรรมวิธีทางความร้อนที่เหมาะสม ซึ่งพบว่า การใช้อัตราการทำความร้อนแบบหลายขั้นตอนและการให้แรงกดอัดคงที่ระหว่างการเผาประสบความสำเร็จในการขึ้นรูปเซลล์ ผลการขึ้นรูปพบว่าความหนาแน่นของชั้นแคโทด อิเล็กโทรไลต์และแอโนด คือ 150 25 และ 30 ไมโครเมตร ตามลำดับ โดยเซลล์อิเล็กโทรไลซิสชนิดดังกล่าวแสดงความหนาแน่นกระแสไฟฟ้าที่มีค่าสูงเท่ากับ 0.95 Acm^{-2} ที่ 1.1 V ภายใต้อัตราส่วนไอน้ำต่อไฮโดรเจนที่ 70:30 อุณหภูมิ 1073 K โดยคิดเป็นอัตราการผลิตไฮโดรเจนได้เท่ากับ $4.95 \times 10^{-6} \text{ mols}^{-1}$ อย่างไรก็ตามความทนทานของเซลล์ในระยะยาวยังคงมีประสิทธิภาพต่ำ โดยมีอัตราการสลายตัวของเซลล์ที่ 0.08 Vh^{-1}

สาขาวิชา	วิศวกรรมเคมี	ลายมือชื่อนิสิต
ปีการศึกษา	2562	ลายมือชื่อ อ.ที่ปรึกษาหลัก

6170255021 : MAJOR CHEMICAL ENGINEERING

KEYWORD: Metal supported solid oxide electrolysis cell, Alloy foam support, Wet-chemical coating, Solid oxide electrolysis cell, hydrogen production, steam electrolysis, sintering additive, CuO

Ramin Visvanichkul : Fabrication and electrochemical performance of nickel-alloy-foam-supported solid oxide electrolysis cell for hydrogen production from steam. Advisor: Asst. Prof. Pattaraporn Kim, Ph.D.

The effect of CuO as a sintering additive on the electrolyte of solid oxide electrolysis cell (SOEC) was investigated. 0.5 wt.% CuO was added into $\text{Sc}_{0.1}\text{Ce}_{0.05}\text{Gd}_{0.05}\text{Zr}_{0.89}\text{O}_2$ (SCGZ) electrolyte as a sintering additive. An electrolyte-supported cell (Pt/SCGZ/Pt) was fabricated. Phase formation, relative density, and electrical conductivity were investigated. The cells were sintered at 1373 K to 1673 K for 4 h. The CuO significantly affected the sinterability of SCGZ. The SCGZ with 0.5 wt.% CuO achieved 95% relative density at 1573 K while the SCGZ without CuO could not be densified even at 1673 K. Phase transformation and impurity after CuO addition were not detected from XRD patterns. The electrochemical performance was evaluated at the operating temperature from 873 K to 1173 K under steam to hydrogen ratio at 70:30. Adding 0.5 wt.% CuO insignificantly affected the electrochemical performance of the cell. The activation energy of conduction (E_a) was $72.34 \text{ kJ mol}^{-1}$ and $74.93 \text{ kJ mol}^{-1}$ for SCGZ and SCGZ with CuO, respectively. A thin-cell composed of nickel- $\text{Sc}_{0.1}\text{Ce}_{0.05}\text{Gd}_{0.05}\text{Zr}_{0.89}\text{O}_2$ (Ni-SCGZ) cathode, SCGZ electrolyte and $\text{Ba}_{0.5}\text{Sr}_{0.5}\text{Co}_{0.8}\text{Fe}_{0.2}\text{O}_{3-\delta}$ (BSCF) anode, having Ni-iron (Ni-Fe) alloy foam (porosity: 5-130 ppi) as a support is successfully fabricated by the sequence wet-chemical coating. The cathode green tape is deposited on the support with viscosity and thermal expansion coefficient (TEC) gradient multi-layers. Two-step firing processes are applied - pre-cathode firing (1373 K, 2 h) and electrolyte sintering (1623 K, 4 h) with multi heating rate and compressive loading. The thickness of functional cathode layer, electrolyte, and anode is 150, 25 and 30 μm , respectively. The fabricated cell of the alloy foam supported SOEC shows excellent current density with 0.95 Acm^{-2} operated at 1.1 V with $\text{H}_2\text{O}:\text{H}_2 = 70:30$, 1073 K, providing hydrogen production rate at $4.95 \times 10^{-6} \text{ mols}^{-1}$. However, the durability of the cell is rather poor under prolong operation with the degradation rate of 0.08 Vh^{-1} .

Field of Study: Chemical Engineering

Student's Signature

Academic Year: 2019

Advisor's Signature

ACKNOWLEDGEMENTS

I would like to express my really great appreciation to my thesis advisor, Asst. Prof. Dr. Pattaraporn Kim-lohsoontorn for all invaluable encouragement and understand in any deep down situation during the thesis course. This thesis has not completed without her guidance and intensive care. The deeply thank is made to PTT hydrogen SOEC project's staff and other students for great discussion and help in any problem with my experiment.

The acknowledgment is also made to PTT public company limited for funding and supporting this research. My sincere thanks are also to scientists, officer, and lecturers in Center of Excellence on Catalysis and Catalytic Reaction Engineering (CECC), Department of chemical engineering, Chulalongkorn University.

I would like to express my thanks to my parent, friends, and my secret love who are the deepest encouragement, and my brightest light when the darkness time had arrived.

Finally, I would like to appreciate myself, my tears, and my hard effort that made me stronger than the old one of me. This prolongs research realized that all of the failures are the way to the great success which was made by those who never give up. To all disheartened people, just believe in yourself and always told that you can make it. If it is done, you will found that all of the bad situations were a piece of cake suddenly. Now, this is my time to spread the wings for the new chapter of my life. I hope this work can be developed the new innovation or technology for Thailand's society.



จุฬาลงกรณ์มหาวิทยาลัย
CHULALONGKORN UNIVERSITY

Ramin Visvanichkul

TABLE OF CONTENTS

	Page
.....	iii
ABSTRACT (THAI)	iii
.....	iv
ABSTRACT (ENGLISH)	iv
ACKNOWLEDGEMENTS	v
TABLE OF CONTENTS	vi
LIST OF TABLES	ix
LIST OF FIGURES.....	xi
CHAPTER I INTRODUCTION	1
1.1 Motivation	1
1.2 Research objective.....	4
1.3 Research scope	5
1.4 Expected benefit.....	5
CHAPTER II LITERATURE REVIEW.....	8
2.1 Hydrogen production	8
2.1.1 Steam Reforming	8
2.1.2 Partial Oxidation.....	9
2.2 Steam Electrolysis Reaction.....	10
2.3 Solid Oxide Electrolysis Cell (SOEC)	13
2.3.1 General principles.....	13
2.3.2 Materials selection	14

2.3.3 Metal supported SOEC.....	24
2.4 Characterization	40
2.4.1 Cell Characterization.....	40
CHAPTER III EXPERIMENTAL	51
3.1 Fabrication and characterization of electrolyte-supported SOEC	51
3.2 Fabrication and characterization of Ni-Fe-alloy-foam-supported SOEC.....	53
3.2.1 Preparation of alloy foam support	53
3.2.2 Preparation of cathode slurry and fabrication of the cathode layer	54
3.2.3 Preparation of electrolyte slurry and fabrication of the electrolyte layer	54
3.2.4 Preparation of anode slurry and fabrication of the anode layer.....	55
3.3 Fabrication and characterization of cathode-supported SOEC.....	56
3.4 Electrochemical performance measurement.....	56
3.4.1 Electrochemical performance measurement of electrolyte-supported SOEC Fabrication	56
3.4.2 Electrochemical performance measurement of Ni-Fe-alloy-foam-supported SOEC.....	58
CHAPTER IV RESULTS AND DISCUSSION	63
4.1 Effect of CuO as sintering additive in different sintering temperature on the electrolyte densification	63
4.1.1 Densification of the electrolyte-supported SOEC.....	63
4.1.2 Phase identification.....	68
4.1.3 Activation Energy of Conduction	69
4.2 Fabrication of Ni-alloy-foam-supported solid oxide electrolysis cell (SOEC).....	71
4.2.1 Thermal behavior of the cathode and electrolyte layers.....	71

4.2.2 Degree of oxidation of the Ni-Fe-alloy foam supports	75
4.2.3 Fabrication of alloy-foam supported SOEC.....	79
4.2.4 Microstructure of alloy-foam-supported SOEC	85
4.3 Electrochemical performance of Ni alloy-foam-supported solid oxide electrolysis cell (SOEC).....	87
4.3.1 I-V curve and EIS measurement.....	87
4.3.2 Comparison of the electrochemical performance between the Ni-Fe- alloy-foam-support and the cathode-support SOEC	90
CHAPTER V CONCLUSIONS	97
5.1 Conclusion	97
5.2 Recommendation.....	98
REFERENCES.....	100
APPENDICES	108
APPENDIX A: CALCULATION.....	110
APPENDIX B: SLURRY FORMULA	118
VITA	120

LIST OF TABLES

	Page
Table 1 Hydrogen production technologies summary [24]	10
Table 2 The typical characteristics of the main electrolysis technologies [25].....	12
Table 3 The review of cathode materials for oxygen-ion conducting electrolyte-supported SOEC	15
Table 4 Examples of doped zirconia based material for solid electrolyte in SOC 16	16
Table 5 Examples of doped ceria based material for solid electrolyte in SOC	17
Table 6 The comparison of total conductivity of YSZ, GDC and ScSZ [34].....	18
Table 7 Oxygen electrode materials for oxygen-ion conducting electrolyte-supported SOC	20
Table 8 Summary of candidate support metals (Ni-based).....	23
Table 9 Summary of previous research in fabrication of SOFC	25
Table 10 Comparison of SOFC fabrication techniques [52]	29
Table 11 Reviewing of electrochemical performance of metal supported-SOC.....	36
Table 12 Average grain size of sintered $\text{Sc}_{0.1}\text{Ce}_{0.05}\text{Gd}_{0.05}\text{Zr}_{0.89}\text{O}_2$ (SCGZ) electrolyte and sintered SCGZ electrolyte with 0.5 wt.% CuO when sintering temperature was varied. 66	66
Table 13 Mass changing of Ni-Fe-alloy foam after firing at different temperature and after reducing in 10 vol% H_2 at 1073 K, 12 h.....	78
Table 14 The properties of the cathode slurries.....	81
Table 15 The parameters extracted from the Nyquist plot of Ni-Fe-alloy-foam supported SOEC with different steam content in electrolytic mode at 1073 K.....	88

Table 16 The parameters extracted from the Nyquist plot of Ni-Fe-alloy-foam supported SOEC and Ni-SCGZ cathode supported SOEC with $\text{H}_2\text{O}:\text{H}_2 = 70:30$ at 1073 K

94



LIST OF FIGURES

	Page
Figure 1 Flowsheet of a conventional steam-methane reforming process [23].	9
Figure 2 Generalized schematic of a single SOEC.....	13
Figure 3 X-ray diffraction patterns of 0.5M0.5Ce10ScSZ (M=Yb, Sm, Gd) and 1Ce10ScSZ [41].....	19
Figure 4 The I-V response of Ni-YSZ/YSZ/LSM-YSZ and Ni-YSZ/YSZ/BSCF in both electrolysis and fuel cell mode (1073 K, H ₂ O/H ₂ =50/50) [42].	21
Figure 5 Performance of the anode-supported single SOFC having unsintered BSCF, LSM and LSCF cathodes at 1073 K, exposing to 97H ₂ % and 3% H ₂ O at the anode and ambient air at the cathode [43].	21
Figure 6 Cross-sectional microstructure of Ni-Fe alloy support oxidized at 873 K in air for 2 h [44].	24
Figure 7 The results of shrinkage analysis in fabrication of Ni-SSZ gradient anodes/SSZ electrolyte for SOFC[15].....	30
Figure 8 Photos of (A) green tape before sintered, (B) co-sintering cell at 3°C/min (30- 1400°C), (C) co-sintering cell at 0.5°C/min (30- 600°C), 3°C/min (600- 800°C) and 1°C/min (800- 1400°C) [15].	31
Figure 9 Tapes after thermal decomposition at 600°C for the fabrication of large-area unit cell [14].	33
Figure 10 SEM micrograph of the polished fracture (left) non NiO gradient and (right) NiO gradient layer on NiCrAl foam support [19].	34
Figure 11 Polarization curves of Ni-SDC infiltrated 430L STS/SSZ/LSFSc infiltrated SSZ metal supported-SOFC measured at 600- 800°C [48].	36
Figure 12 Total (R_T), ohmic (R_Ω) and polarization (R_p) resistances of the Ni-Fe/Ni-GDC/GDC/LSM-BSCF SOFC as a function of testing temperature obtained from	

measured electrochemical impedance spectra at open circuit voltage and various temperatures between 500 and 650°C [44].....	37
Figure 13 SEM image of (a,b) polished cross section of STS/SDCN-YSZ/YSZ/LSM-YSZ/STS metal supported-SOFC structure after sintering and before catalyst infiltration [58]	38
Figure 14 Temperature-dependence of the initial cell stability of LSM/SDCN cell. (a) Current density at 0.7 V and (b) OCV for cells operated potentiostatically [58].....	39
Figure 15 Long-term operation: (a) Current density at 0.7 V for cells operated potentiostatically at 700°C with LSM/SDCN (black) and symmetric SDCN/SDCN (blue) catalysts. Current step polarization curves at 700°C before (black) and after (blue) long-term operation for (b) LSM/SDCN and (c) SDCN/SDCN [58].....	40
Figure 16 Rheological properties of YSZ inks at 333 K as a function of dispersant content for Solsperse S3000 and Nuosperse FA196 dispersants and three different YSZ powders of TZ-8Y, TZ-8YS and TZ-8YS having surface areas of 12.3, 6.2 and 3.1 m ² /g, respectively. 41	
Figure 17 Schematic of rheometer [59].....	42
Figure 18 Proper loading of sample after closing the gap for cone and parallel plate geometry systems [61].....	42
Figure 19 Effects of various parameters on different section of a typical viscosity curve [60]	43
Figure 20 SEM Configuration [63].....	43
Figure 21 Difference in contrast of the NiO and CGO is visible with the darker particle denoting NiO [63].....	44
Figure 22 Energy dispersive X-ray analysis of different points in the same scan area showing different elemental composition of each points [63].....	45
Figure 23 X-ray diffraction in crystalline structure [64].....	46
Figure 24 Diffraction peak and information content [64].....	47

Figure 25	Schematic of TGA station [65].....	48
Figure 26	Re-oxidation TMA of fine structured anode sample [66].....	48
Figure 27	Typical stress-strain curve of a semi-crystalline material with some.....	49
Figure 28	Photo images of the setup for 3-point bending test of cell [46].....	50
Figure 29	Schematic drawing of electrolyte-supported SOEC; (a) top view, (b) side view	52
Figure 30	Schematic drawing of Alloy foam-supported SOEC ;(a) top view, (b) side view [67]	55
Figure 31	The fabrication procedure of electrolyte-supported SOEC.....	59
Figure 32	The fabrication procedure of cathode-supported SOEC.....	60
Figure 33	The fabrication procedure of Alloy foam-supported SOEC.....	61
Figure 34	The preparation procedure of electrode slurries	62
Figure 35	Scanning electron microscope (SEM) images of sintered $Sc_{0.1}Ce_{0.05}Gd_{0.05}Zr_{0.89}O_2$ (SCGZ) at (a) 1423 K, (b) 1473 K, (c) 1523 K, (d) 1573 K, (e) 1623 K, and (f) 1673 K.	64
Figure 36	SEM images of sintered $Sc_{0.1}Ce_{0.05}Gd_{0.05}Zr_{0.89}O_2$ (SCGZ) with 0.5 wt.% CuO at (a) 1423 K, (b) 1473 K, (c) 1523 K, (d) 1573 K, (e) 1623 K, and (f) 1673 K.....	65
Figure 37	Relative density (%) of the SCGZ pellet and the SCGZ pellet with 0.5 wt.% CuO when the sintering temperature was varied.	67
Figure 38	The X-ray diffraction patterns of (a) sintered SCGZ at 1673 K and (b) sintered SCGZ with 0.5 wt.% CuO at 1523 K.	68
Figure 39	The I-V curves of the SCGZ electrolyte-supported SOEC conducted from 873 K to 1173 K under a constant steam to hydrogen ratio (70:30)	70
Figure 40	The I-V curves of the SCGZ with 0.5wt.% CuO electrolyte-supported SOEC conducted from 873 K to 1173 K under a constant steam to hydrogen ratio (70:30)	70

Figure 41	Activation energy of conduction (E_a) for the SOEC having SCGZ electrolyte and 0.5 wt.% CuO-added SCGZ electrolyte.....	71
Figure 42	Thermal gravimetric (TG) curve and differential thermal analysis.....	73
Figure 43	Thermal gravimetric (TG) curve and differential thermal analysis (DTA) curve of the green electrolyte layer.....	73
Figure 44	Sinterability of dip-coated electrolyte layer with 0.5-1 wt.% of CuO as sintering additive in SCGZ at various sintering temperature.	75
Figure 45	Degree of oxidation of candidate for the support at 1073 K under atmosphere.....	76
Figure 46	Stress-strain curve of Ni-Fe-alloy foam in different firing process	78
Figure 47	Ni-SCGZ cathode on the Ni-Fe-alloy foam and SEM images of cross sectional cell fabricated by varying solid content in the cathode slurry.....	81
Figure 48	Viscosity-shear rate curve of the cathode slurries.....	82
Figure 49	Images of sintered cells with different heat treatment conditions.....	85
Figure 50	The Ni-Fe-alloy-foam supported Ni-SCGZ/SCGZ/BSCF SOEC.....	86
Figure 51	SEM image of Ni-Fe-alloy-foam supported-SOEC before electrochemical performance measurement; (a) SCGZ with 0.5 wt.% CuO additive, (b) cross sectional image of Ni-Fe-foam supported Ni-SCGZ/SCGZ SOEC and (c) interface between SCGZ electrolyte and Ni-SCGZ cathode layer.....	86
Figure 52	I-V curves of of Ni-Fe-alloy-foam supported SOEC; (a) with $H_2O:H_2 = 70:30$ at various operating temperature, (b) at 1073 K with various $H_2O:H_2$ content and (c) Nyquist plot of Ni-Fe-alloy-foam supported SOEC with different steam content in feeding gas under electrolytic mode (1.1V).....	89
Figure 53	I-V curves of Ni-Fe-alloy-foam supported SOEC and Ni-SCGZ cathode-supported SOEC with $H_2O:H_2 = 70:30$ at 1073 K.....	92
Figure 54	The Nyquist plot at $H_2O:H_2 = 70:30$ and 1073 K: (a) Ni-Fe-alloy-foam supported SOEC and (b) Ni-SCGZ cathode supported SOEC.....	93

Figure 55 Durability test of Ni-Fe-alloy-foam supported SOEC and Ni-SCGZ cathode supported SOEC operated at 0.9 and 0.6 Acm^{-2} , respectively with $\text{H}_2\text{O}:\text{H}_2 = 70:30$ at 1073 K, 10 h. 94

Figure 56 SEM images of Ni-Fe-alloy foam supported SOEC after durability test operated at 0.9 cm^{-2} with $\text{H}_2\text{O}:\text{H}_2 = 70:30$ at 1073 K and 10 h.....95

Figure 57 Image of Ni-Fe-alloy-foam supported SOEC after durability test operated at 0.9 and 0.3 Acm^{-2} with $\text{H}_2\text{O}:\text{H}_2 = 70:30$ at 1073 K, 10 h.....96



CHAPTER I

INTRODUCTION

1.1 Motivation

Hydrogen can be used as various application followed by the growth of technologies such as feedstock in chemical process, fuel production, fertilizer production, heat-treating metals and pharmaceuticals etc. Hydrogen is the one of alternative fuel which is an efficient energy carrier for renewable energy. The demand has trend to dramatically increase in the near future. Nowadays, hydrogen global production has been manufactured through the combustion of fossil fuel such as natural gas. Most of the global production uses the steam reforming of methane which is the cheapest process for hydrogen production. However, this process generates greenhouse gas emission and produces hydrogen with impurity content. Purification process must be used in the downstream of production. For sustainable and friendly environment, researcher has extensively paid attention for developing alternative processes in a large scaling of hydrogen production.

Steam electrolysis through solid oxide electrolysis cell (SOEC) is one of the promising processes to produce high purity hydrogen and oxygen as products without greenhouse gas emission. The reaction is taken place in the gas phase with a high operating temperature. SOEC device requires less total energy for dissociation of the steam molecule than liquid phase reaction as water. Higher hydrogen production rate is also identified for SOEC technology when compared with other conventional water steam electrolysis devices. This advantage introduced to SOEC which is modified and tough researched is potential processes that provide large value in long

term operation for hydrogen production. SOEC is actually the reversed functional working of solid oxide fuel cell (SOFC). SOEC consists of an electrolyte sandwiched by anode and cathode. Hydrogen is produced at cathode side in which steam is reduced to hydrogen and oxygen ions by potential supplying. Electrolyte is used as ionic membrane for oxygen ion diffusion to anode side. Oxygen gas is formed by oxidation at the anode. This working electrolysis cell is called oxygen-ionic-conducting SOEC which is the main focus for this research.

Challenge remains for SOEC development to improve performance and durability of the cell [1-6]. One of the strategies to overcome the challenge is to fabricate a thinner cell, reducing total resistance, especially the ohmic resistance. In general, the cell requires a mechanical support from a thick electrode or electrolyte, which is referred as cathode-, anode- or electrolyte-supported cell [7]. Therefore, to fabricate a thinner ceramic cell, alternative materials, which is often metal or metal alloy, are extensively studied to increase mechanical strength of the thin ceramic cell. This cell type is referred as metal-supported cell.

Material selection of the support and the cell's fabrication process are important. Ferritic stainless steel has been widely used as the support material in solid oxide fuel cell (SOFC) due to its low cost. However, elemental inter-diffusion of chromium (Cr) from the substrate to electrode can occur during heat treatment process [8-11]. Cr poisoning occur when Cr diffuses and reacts with oxygen to form chromium oxide [12]. Ni-based support is also considered because of the material compatibility between the support and electrode. However, Ni coarsening and Ni infiltration can occur after high-temperature heat treatment and degrade the cell's performance. Therefore a composite of Ni-alloy can be advantageous and in turn contributes to extensive material choice in research and development.

Low-temperature process such as pulsed laser deposition (PLD), plasma spray, and electrophoretic deposition (EPD) has been used to fabricate metal-

supported cell. Compared to various thin layer deposition, sequence wet-chemical coating involves tape-casting, dip coating and screen printing can provide multi active-layer with simple process and reasonable cost. Kim et al. [13] successfully fabricates a metal-supported SOFC using a sheet of Ni-Fe alloy as the support. Lee et al. [14] proposes a cost-effective production of metal-supported SOFC. The rheological properties of the slurry to produce the flatness and smooth green layer are reported as an important factor of this deposition technique. Moreover, the ratio of starting powder and polymeric solvent and additives is important factor in the slurry formulation. The decomposition of additives and shrinkage in the green layer can also induce cracking and delamination of cell [15]. The sequence wet-chemical coating is a high-temperature process. Ceramic parts in the cell are generally sintered in air at elevated temperatures, but due to the presence of metal support, the cell requires sintering in reducing condition to prevent metal oxidation. However, reducing conditions causes nickel coarsening in electrode, oxygen electrode decomposition, and accelerates elemental inter-diffusion [16]. Considering sintering in air atmosphere, creeping in the cell can occur and creep will gradually generate cracks in the electrolytes. It was reported that the oxide layer generate during sintering can significantly affect the creep behavior of the metal [17]. Therefore, oxidation resistance in the support is important.

Metal foam provides good mechanical properties, lightweight while maintaining high strength and rigidity. The complex geometry within the metal foam increases the surface area per unit volume and is an ideal for heat transfer or thermal management [18]. Gondolini et al. [19] proposed a fabrication method of Ni-GDC on Ni-Cr-Al foam with screen printing technique. However, the electrochemical performance was not reported in the work. In our previous work [20], the cathode-supported SOEC, composing of Ni-Sc_{0.1}Ce_{0.05}Gd_{0.05}Zr_{0.89}O₂ (Ni-SCGZ) cathode, SCGZ electrolyte and Ba_{0.5}Sr_{0.5}Co_{0.8}Fe_{0.2}O_{3-δ} (BSCF), exhibited rather relatively high

performance. In this study, the Ni-Fe alloy foam was chosen as a promising support material due to its high porosity and oxidation resistance in order to compose to the alloy-foam supported Ni-SCGZ/SCGZ/BSCF. However, the fabrication of thin ceramic layer on the foam is the rather difficult and various parameters to obtain successfully fabricated SOEC.

In this study, to fabricate Ni-Fe-alloy-foam supported SOEC, the sequence wet-chemical coating of electrode having a gradient of thermal expansion coefficient (TEC) as well as firing process was investigated. Slurries formula and heat treatment condition was proposed. Thermal behavior of the green layer and the alloy-foam support were studied. Slurries rheology was also identified to control viscosity of the green tapes during fabrication. The microstructure of the cell was characterized. The electrochemical performance and durability of the SOEC are measured under H_2O/H_2 feed with varied steam content in a controlled temperature.

1.2 Research objective

To fabricate and measure the electrochemical performance of Ni-Fe-alloy-foam supported solid oxide electrolysis for hydrogen production from high temperature steam electrolysis.

Sub-object includes:

1.2.1 To determine the effect of CuO as sintering additive in different sintering temperature on the densification and electrochemical performance of scandium cerium- and gadolinium-doped zirconia electrolyte

1.2.2 To fabricate Ni alloy-foam-supported solid oxide electrolysis cell (SOEC) in button size

1.2.4 To generate recipe for electrodes and electrolyte slurries in the cell fabrication process

1.2.5 To determine suitable heat treatment condition during fabrication process

1.2.6 To investigate electrochemical performance and durability alloy foam-supported SOEC and determine the effect of operating condition (temperature and steam content)

1.3 Research scope

1.3.1 The fabrication of Ni-Fe-alloy-foam supported SOEC is carried out using the sequence wet-chemical coating. The condition parameters are slurry compositions and heat treatment during electrolyte sintering process.

1.3.2 Cathode layers are designed to obtain TEC and viscosity gradient layer.

1.3.3 Ni-Fe-alloy-foam (60 wt.% of Ni and 40 wt.% of Fe) is used as support

1.3.4 Nickel oxide (NiO) / Scandium cerium- and gadolinium-doped zirconia ($\text{Sc}_{0.1}\text{Ce}_{0.05}\text{Gd}_{0.05}\text{Zr}_{0.89}$, SCGZ) cermet and SCGZ are used as cathode and electrolyte material, respectively

1.3.5 $\text{Ba}_{0.5}\text{Sr}_{0.5}\text{Co}_{0.8}\text{Fe}_{0.2}\text{O}_{3-\delta}$ (BSCF) is used as anode materials.

1.3.6 Hydrogen is produced via high-temperature steam electrolysis reaction, controlling potential from OCV to 1.8 V.

1.4 Expected benefit

The fabrication of Ni-Fe-alloy-foam supported SOEC which is carried out using the sequence wet-chemical coating will be investigated for hydrogen production by steam

electrolysis reaction at high temperature (1073K). Two major concepts of this thesis consisting of 1) The study effect of CuO as sintering additive in scandium cerium- and gadolinium-doped zirconia ceramic based SOEC and 2) The fabrication and performance measurement of Ni-Fe-alloy-foam supported SOEC.

The outcome of this project can be critical beneficial for SOEC development. Up to our knowledge, there is no report on using alloy foam as the support of cell for SOEC application. The support could help improve electrochemical performance because the ceramic parts are thinner. The metal foam contains porosity for gas diffusion and is also cheaper than conventional metal support with machining for gas-flow-field.

This research supports clean and sustainable process with high purity of hydrogen production development. It can be a principle conceptual for scaling-up in stack SOEC. The fabrication process and operating condition are proposed for Ni-Fe-alloy-foam supported SOEC in hydrogen production.

Research results including 1 petty patent application and 2 publications as follows:

1.4.1 Thailand's petty patent application number: 1903003170

(การเตรียมเซลล์ไฟฟ้าเคมีประเภทออกไซด์ของแข็งชนิดที่มีโลหะความพรุนสูงเป็นตัวรองรับ)

1.4.2 R. Visvanichkul, S. Peng-Ont, W. Ngampuengpis, N. Sirimungkalakul, P. Puengjinda, T. Jiwanuruk, T. Sornchamni, P. Kim-Lohsoontorn. Effect of CuO as sintering additive in scandium cerium and gadolinium-doped zirconia-based solid oxide electrolysis cell for steam electrolysis. Processes. 2019; 7(12):868.

1.4.3 R. Visvanichkul, S. Peng-Ont, W. Ngampuengpis, N. Sirimungkalakul, P. Puengjinda, T. Jiwanuruk, T. Sornchamni, P. Kim-Lohsoontorn. Fabrication of alloy foam-supported solid oxide electrolysis cell (SOEC) for hydrogen production. The 2nd International Symposium on Hydrogen Energy and Energy Technologies (HEET 2019), Osaka, Japan, Dec 12-13, 2019



จุฬาลงกรณ์มหาวิทยาลัย
CHULALONGKORN UNIVERSITY

CHAPTER II

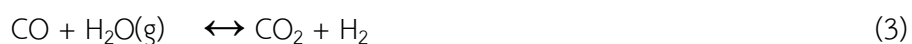
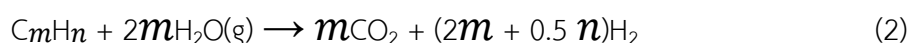
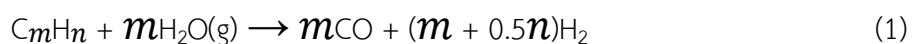
LITERATURE REVIEW

2.1 Hydrogen production

Hydrogen is a molecule with H₂ formula consisting of two hydrogen atoms which formed by single bond [21]. It can be used in various applications following the growth of technologies. According to energy crisis and environmental problem, the growth of hydrogen demand has been increasing dramatically more than threefold since 1975 [22]. There are common processes for hydrogen production in the present. Example of commercial processes is discussed as following below;

2.1.1 Steam Reforming

The most widespread process for hydrogen production is steam reforming. The process uses light natural gas like methane as raw material in which the reaction as Eqs. (1)- (4) take places to convert fuel to hydrogen. The advantage arises from the high efficiency of operation and the low operational and production costs.



However, carbon monoxide (CO) and carbon dioxide (CO₂) is the by-product of this process. This requires purification in the downstream product. Moreover,

severe operating temperature, multi-steps and high amount of energy are consumed during process. Fig. 1 shows the flowsheet diagram of steam-methane reforming [23].

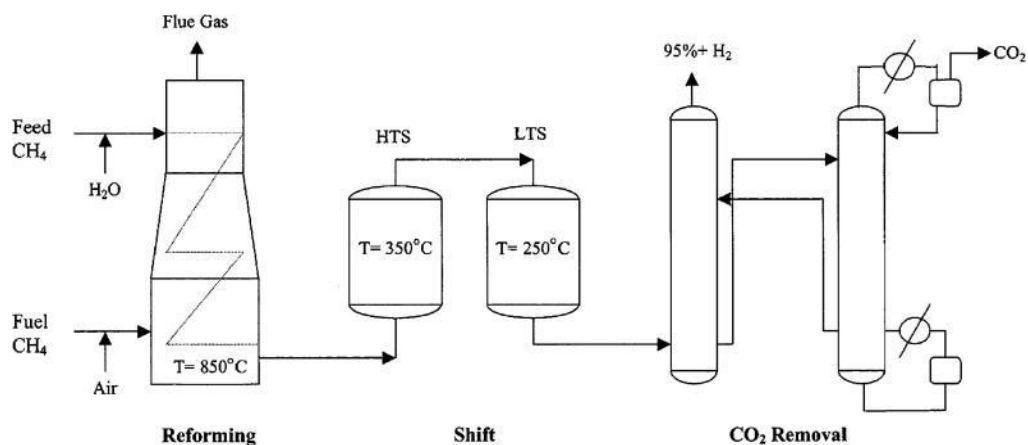


Figure 1 Flowsheet of a conventional steam-methane reforming process [23]

2.1.2 Partial Oxidation

The presence of oxygen in feed is the different point when compared with the other process. Oxygen is used as oxidizing agent in hydrocarbon combustion to produce hydrogen as the primary product. The reaction of partial oxidation of methane is shown in Eqs (5)- (7). High temperature (>1573 K) and pressure (>3 MPa) are required in reactions without catalyst [24]. As presence of oxygen gas, high purity of oxygen requires in the process. Air separation for pure oxygen must involve in production lead to high cost for this purification.



There are by-product gases consisting of CO, CO₂, H₂O, CH₄, hydrogen sulfide (H₂S), and carbon-oxysulfide (COS) in gaseous mixture. The decomposition of acetylene as an intermediate product is produced soot during process. The amount of soot depends on the ratio of H:C in the initial feed gas.

In addition to discuss, hydrogen can produce through various technologies and sources as shown in Table 1. To optimize process, minimize environmental impact and energy consumption, hydrogen production development is research challenging in energy and environment research field.

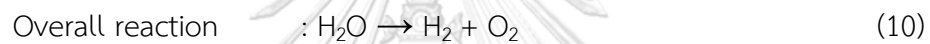
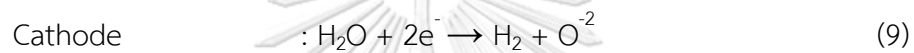
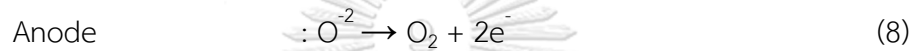
Table 1 Hydrogen production technologies summary [24]

Technology	Feedstock	Efficiency	Maturity
Steam reforming	Hydrocarbons	70–85%	Commercial
Partial oxidation	Hydrocarbons	60–75%	Commercial
Autothermal reforming	Hydrocarbons	60–75%	Near term
Plasma reforming	Hydrocarbons	9–85%*	Long term
Biomass gasification	Biomass	35–50%	Commercial
Aqueous phase reforming	Carbohydrates	35–55%	Med. term
Electrolysis	H ₂ O + electricity	50–70%	Commercial
Photolysis	H ₂ O + sunlight	0.5%*	Long term
Thermochemical water splitting	H ₂ O + heat	NA	Long term

*Hydrogen purification is not included.

2.2 Steam Electrolysis Reaction

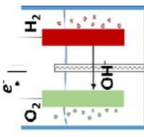
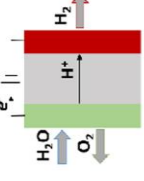
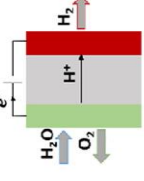
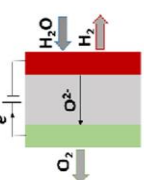
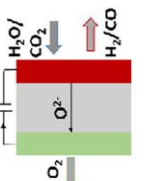
As discussed on previous section, common processes for hydrogen production use conventional fossil fuel as raw material and produce hydrogen mixed with CO₂ or CO. Therefore, steam electrolysis is a promising process to produce high purity hydrogen without greenhouse gas emission to atmosphere. Steam electrolysis reaction is based on electrochemical reaction, using electrical potential supplying with conductive electrodes to produced steam in electrolytic cell. The steam is produced by following Eqs (8)-(10).



The electrical potential is supplied from external circuit. Water can be broken up into hydrogen and oxygen molecule by this direct current passing. This method has been commercially used for hydrogen production since the initial of 19th century.

There are various electrolysis technologies such as proton exchange membrane (PEM), alkaline based cell and solid oxide cells (SOCs). Table 2 displays example of electrolysis technologies.

Table 2 The typical characteristics of the main electrolysis technologies [25]

		Low Temperature Electrolysis			High Temperature Electrolysis		
		Alkaline (OH ⁻) electrolysis	Proton Exchange Membrane	Proton Exchange (H ⁺) electrolysis	Solid Oxide Electrolysis (SOE)	Oxygen ion(O ²⁻) electrolysis	
		Liquid	Polymer Electrolyte Membrane	H ⁺ - PEM	H ⁺ - SOE	O ²⁻ - SOE	Co-electrolysis
Operation principles							
Charge carrier		OH ⁻	H ⁺	H ⁺	H ⁺	O ²⁻	O ²⁻
Temperature		20-80°C	20-200°C	500-1000°C	500-1000°C	500-1000°C	750-900°C
Electrolyte		liquid	solid (polymeric)	solid (ceramic)	solid (ceramic)	solid (ceramic)	solid (ceramic)
Anodic Reaction (OER)		$4\text{OH}^- \rightarrow 2\text{H}_2\text{O} + \text{O}_2 + 4\text{e}^-$	$2\text{H}_2\text{O} \rightarrow 4\text{H}^+ + \text{O}_2 + 4\text{e}^-$	$2\text{H}_2\text{O} \rightarrow 4\text{H}^+ + 4\text{e}^- + \text{O}_2$	$2\text{H}_2\text{O} \rightarrow 4\text{H}^+ + 4\text{e}^- + \text{O}_2$	$\text{O}^{2-} \rightarrow \frac{1}{2}\text{O}_2 + 2\text{e}^-$	$\text{O}^{2-} \rightarrow \frac{1}{2}\text{O}_2 + 2\text{e}^-$
Anodes		Ni > Co > Fe (oxides) Perovskites: $\text{Ba}_{0.5}\text{Sr}_{0.5}\text{Co}_{0.8}\text{Fe}_{0.2}\text{O}_{3-5}$, LaCoO_3	IrO_2 , RuO_2 , $\text{Ir}_x\text{Ru}_{1-x}\text{O}_2$ Supports: TiO_2 , ITO, TIC	Perovskites with protonic-electronic conductivity	$\text{La}_x\text{Sr}_{1-x}\text{MnO}_3 + \text{Y-Stabilized ZrO}_2$ (LSM-YSZ)	$\text{La}_x\text{Sr}_{1-x}\text{MnO}_3 + \text{Y-Stabilized ZrO}_2$ (LSM-YSZ)	$\text{La}_x\text{Sr}_{1-x}\text{MnO}_3 + \text{Y-Stabilized ZrO}_2$ (LSM-YSZ)
Cathodic Reaction (HER)		$2\text{H}_2\text{O} + 4\text{e}^- \rightarrow 4\text{OH}^- + 2\text{H}_2$	$4\text{H}^+ + 4\text{e}^- \rightarrow 2\text{H}_2$	$4\text{H}^+ + 4\text{e}^- \rightarrow 2\text{H}_2$	$4\text{H}^+ + 4\text{e}^- \rightarrow 2\text{H}_2$	$\text{H}_2\text{O} + 2\text{e}^- \rightarrow \text{H}_2 + \text{O}^{2-}$	$\text{H}_2\text{O} + 2\text{e}^- \rightarrow \text{H}_2 + \text{O}^{2-}$ $\text{CO}_2 + 2\text{e}^- \rightarrow \text{CO} + \text{O}^{2-}$
Cathodes		Ni alloys	Pt/C MoS ₂	Ni-cermet	Ni-YSZ	Ni-YSZ	Ni-YSZ perovskites
Efficiency		59-70%	65-82%	up to 100%	up to 100%	up to 100%	-
Applicability		commercial	near-term commercialization	laboratory scale	laboratory scale	demonstration	laboratory scale
Advantages		low capital cost, relatively stable, mature technology	compact design, fast response/start-up, high-purity H ₂	enhanced kinetics, thermodynamics: lower energy demands, low capital cost	enhanced kinetics, thermodynamics: lower energy demands, low capital cost	enhanced kinetics, thermodynamics: lower energy demands, low capital cost	+ direct production of syngas
Disadvantages		corrosive electrolyte, gas permeation, slow dynamics	low OH ⁻ conductivity in polymeric membranes	mechanically unstable electrodes (cracking), safety issues: improper sealing	mechanically unstable electrodes (cracking), safety issues: improper sealing	mechanically unstable electrodes (cracking), safety issues: improper sealing	
Challenges		Improve durability/reliability; and Oxygen Evolution	Reduce noble-metal utilization	microstructural changes in the electrodes: delamination, blocking of TPBs, passivation	microstructural changes in the electrodes: delamination, blocking of TPBs, passivation	microstructural changes in the electrodes: delamination, blocking of TPBs, passivation	C deposition, microstructural change electrodes

2.3 Solid Oxide Electrolysis Cell (SOEC)

2.3.1 General principles

Solid oxide electrolysis cell is an electrochemical device that is made from metal and ceramic materials. This device allows the conversion of steam into hydrogen under steam electrolysis reaction as discussed in section 2.2. Conversely, an electrolysis cell is reverse working mode of fuel cell device in which the electricity is produced by chemical energy of fuel feed gas.

The cell is consisted of three layers which is cathode (H_2 electrode), electrolyte and anode (O_2 electrode) as shown in Fig. 2.

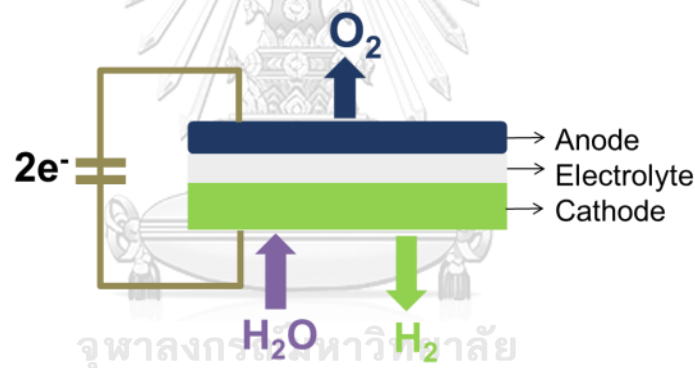


Figure 2 Generalized schematic of a single SOEC

The steam is introduced at cathode side and broken bond into hydrogen molecule and oxygen ion (O^{2-}) by external potential supplying. Hydrogen is swept through out of cathode channel as primary product. An oxygen ion is transferred through solid electrolyte layer which is ion conductive material. This process is called oxygen-ion conducting SOEC. For proton-ion conducting SOEC, the transferring ion is proton ion (H^+) [26].

SOEC research and development has been interesting. There are many research challenge aim for commercialization and effective production. The summary of previous SOEC research result and discussion are discussed in section 2.3.2-3.

2.3.2 Materials selection

To find high electrical and ion conductive material for SOEC fabrication, material selection for electrodes plays important role. Criteria of material selection in SOEC are similar to those in solid oxide fuel cell (SOFC). Each electrode must be provided specific properties as following discussion;

2.3.2.1 Cathode (H_2 electrode)

Dwivedi [27] reports that an H_2 electrode material properties consisting of high electrical conductivity for external circuit supplying, good stability in long term operation and provide enough electro-catalytic efficiency with optimized porosity for mass transport of carrier gas. Along with SOFC function, Nickle (Ni) provide highest electrochemical performance in case of H_2 -based reaction and also maintains the thermal compatibility with ceramic electrolyte material. Composite of Ni metal and Yttria-stabilized zirconia (YSZ) as Ni-YSZ cermet (conventional cermet) enhances reaction sites of H_2 electrode. The polarization resistance is also reduced by inhibition of Ni grain growth. Therefore, Ni-YSZ cermet is generally used material for fuel electrode of solid oxide cell. Some reviews of other cathode materials are listed in Table 3.

Table 3 The review of cathode materials for oxygen-ion conducting electrolyte- supported SOEC

Materials	Cell configuration	Feed gas	Temperature (K)	Current density (Acm ⁻²)	Voltage (V)	Reference
Pr _{0.3} Sr _{0.7} Ti _{0.3} Fe _{0.7} O _{3-δ} (PSTF)	PSTF YSZ LSM-YSZ	60%H ₂ O/Ar	1073	-0.30	1.46	[28]
Ni _{0.6} Fe _{0.4} /SDC	Ni _{0.6} Fe _{0.4} /SDC YSZ LSM- SDC	40%H ₂ O/H ₂	1073	-0.29	1.50	[29]
Ni/YSZ	Ni/YSZ YSZ LSCF-GDC	70%H ₂ O/ H ₂ (Seawater)	1073	-1.00	1.19	[30]
Ni/YSZ	Ni/YSZ YSZ LSM-YSZ	70%H ₂ O/ H ₂	1223	-3.6	1.48	[31]

2.3.2.2 Electrolyte

An electrolyte is dense layer. Perovskite ceramics at which oxygen vacancies are found into crystalline structure is the candidate electrolytes for SOEC fabrication. High capability of ionic conductive material as discussed in section 2.3.1 is desirable. Both of mechanical and chemical properties are also stability and compatibility with other electrodes [27].

Jaiswal et al. [32] review many research in development of solid electrolytes for SOFC. It was reported the general principle of electrolyte structure. There are two based materials consist of Zirconia (Zr) based and Ceria (Ce) based which are conventional electrolyte material. These materials are an IV-B group metal oxide with addition of other transition metal oxide into their structure. The crystalline structure which is cubic fluorite phase structure provides high oxygen diffusion with high

tolerance of atomic disorder. Many effort in Zr- based and Ce- based material development have been studying for SOC implementation.

A. Zirconia based material

As crystalline structure of pure zirconia oxide (ZrO_2), cubic fluorite phase structure can be obtained at high temperature (above 2573 K) which provides low ionic conductivity at SOC operating temperature [32]. To stabilize the structure, doping transition metal element into ZrO_2 structure is conducted in research solution. Table 4 lists examples of doped zirconia based material for solid electrolyte in SOC.

Table 4 Examples of doped zirconia based material for solid electrolyte in SOC

Materials	Temperature (K)	Total conductivity (S/cm)	Reference
8%YSZ with 4% Fe_2O_3	973	0.400*	[33]
$(Sc_2O_3)_{0.093}(ZrO_2)_{0.907}$ or (9.3%ScSZ)	1073	0.120	[34]
$(Sc_2O_3)_{0.10}(CeO_2)_{0.01}(HfO_2)_{0.01}(ZrO_2)_{0.88}$	1073	0.140	[35]
$(Sc_2O_3)_{0.04}(Y_2O_3)_{0.04}(ZrO_2)_{0.92}$	1073	0.062	[34]
$(Y_2O_3)_{0.08}(ZrO_2)_{0.92}$ or (8%YSZ)	1073	0.052	[34]

*Calculation with The Nernst-Einstein relation

B. Ceria based material

Another conventional electrolyte material is ceria based material. Aliovalent cation doped ceria with alkaline earth metal oxide such as Calcium (CaO), Samarium (Sm_2O_3), Neodymium (Nd_2O_3) and Gadolinium (Gd_2O_3) has demonstrated an excellent

ionic conductivity. However, electronic conductivity is obtained at intermediate temperature (873 K to 1573 K). It also requires high sintering temperature to produce the dense of microstructure for high ionic conductivity [36].

Table 5 Examples of doped ceria based material for solid electrolyte in SOC

Materials	Temperature (K)	Total conductivity (S/cm)	Reference
$\text{Ce}_{0.9}\text{Gd}_{0.1}\text{O}_{1.95}$	973	0.043	[37]
$\text{Ce}_{0.8}\text{Ga}_{0.05}\text{Cu}_{0.15}\text{O}_{1.825}$	973	0.020	[38]
$\text{Sm}_{0.174}\text{Ce}_{0.826}\text{O}_{1.913}$	973	0.020	[39]
$\text{Ce}_{0.8}\text{Er}_{0.2}\text{O}_{2-\delta}$	973	0.018	[36]
CeO_2	873	3.71×10^{-4}	[39]

These conventional materials (zirconia based and ceria based) provide advantage and disadvantage in their applications. Scandium doped zirconia based provides the highest conductivity when compared with other doping but high temperature requiring to achieve sufficient ionic conductivity. Simultaneously, gadolinium doping is excellent ion conductor in ceria based material. However, electronic conductivity is found in their property. Ceria is reduced from Ce^{4+} to Ce^{3+} under reducing atmosphere, leading to electrical short circuit and voltage loss during operation [40].

To optimize the solid state properties, tri-doping of scandium, gadolinium and cerium into zirconia based is purposed for material implementation. The comparison of total conductivity of YSZ, GDC and ScSZ was shown in Table 6.

Table 6 The comparison of total conductivity of YSZ, GDC and ScSZ [34]

Materials	Temperature (K)	Total conductivity (S/cm)
9.3%ScSZ	1073	0.120
$(\text{CeO}_2)_{0.80}(\text{GdO}_{1.5})_{0.20}$ or GDC		0.093
8%YSZ		0.052

Scandia-stabilized zirconia co-doped with CeO_2 is a promising electrolyte in term of conductivity but rapid degradation occurs in a long-term operation. Chin et al. [41] studies the effect of M_2O_3 ($\text{M}=\text{Yb}, \text{Gd}, \text{Sm}$) and CeO_2 co-doping into Scandium doped zirconia structure on their conductivity degradation. It is reported that scandium doped zirconia with Gd_2O_3 and CeO_2 as co-dopant provides only cubic phase in their crystalline structure as shown in Fig. 3. This introduces a high ionic conductivity.

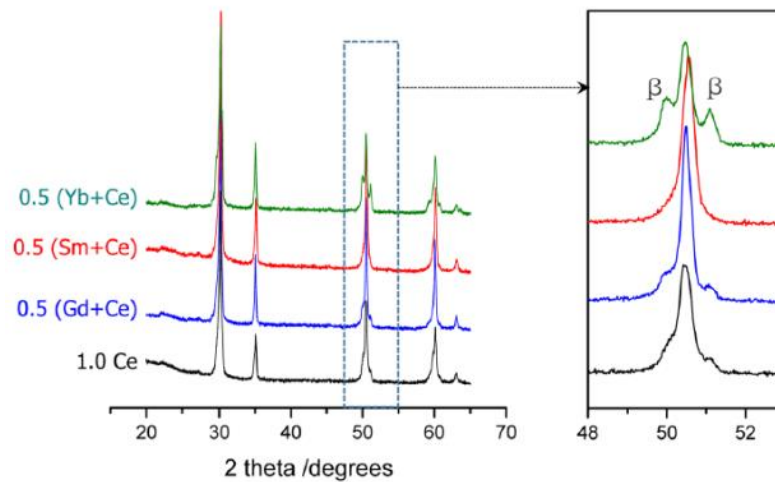


Figure 3 X-ray diffraction patterns of 0.5M0.5Ce10ScSZ (M=Yb, Sm, Gd) and 1Ce10ScSZ [41]

2.3.2.3 Anode (Oxygen electrode)

In oxygen electrode side, the electrode is dominated by severe oxidizing atmosphere. Air is a favorable gas feed into this side. Good oxygen electrode contains three phase boundary as same as hydrogen electrode. These properties include electrical conductivity, ionic conductivity and high gas permeability. Mixed ionic electronic conductive material with sufficient porous structure is required to achieve an excellent electrode.

The LSM-YSZ composite is widely used as the conventional material for oxygen electrode in galvanic cell. LSM is used as electronic conductor and YSZ is used as ionic conductor. The composite displays high stability in thermal and chemical property. In electrolytic cell, the resistance has been higher than galvanic cell. However, overall electrode resistance must be similarly in term of both working modes (electrolytic and galvanic cell) [42]. Table 7 summarizes the candidate of oxygen electrode materials

Table 7 Oxygen electrode materials for oxygen-ion conducting electrolyte-supported SOC

Materials	Cell configuration	Feed gas	Temperature (K)	Current density (Acm ⁻²)	Voltage (V)	Reference
BSCF	Ni/YSZ YSZ BSCF	97%H ₂ /H ₂ O	1073	1.46	0.6	[43]
		50% H ₂ O/H ₂		-0.34	1.2	[42]
LSCF	Ni/YSZ YSZ LSCF	97%H ₂ /H ₂ O		1.21	0.6	[43]
LSM	Ni/YSZ YSZ LSM	97%H ₂ /H ₂ O		0.99	0.6	[42]
LSM-YSZ	Ni/YSZ YSZ LSM-YSZ	50% H ₂ O/H ₂		-0.20	1.2	[43]

Kim-lohsoontorn et al. [42] investigate performance of cathode supported-solid oxide electrolysis cell with different anode materials (LSM-YSZ and Ba_{0.5}Sr_{0.5}Co_{0.8}Fe_{0.2}O_{3-δ}, BSCF). It is reported that BSCF has greater electrical performance than LSM-YSZ as polarization curve shown in Fig. 4. However, degradation of BSCF occurs during long time operation, leading to increasing of ohmic resistance.

Kim et al. [43] also investigate electrochemical performance of BSCF material without pre-sintering process in anode supported-SOFC. La_{0.6}Sr_{0.4}Co_{0.8}Fe_{0.2}O_{3-δ} (LSCF) and La_{0.8}Sr_{0.2}MnO_{3-δ} (LSM) are also investigated in this study. The performance of BSCF is higher than other materials in term of current density (Fig. 5). Therefore, BSCF can be a promising oxygen electrode material for SOC fabrication.

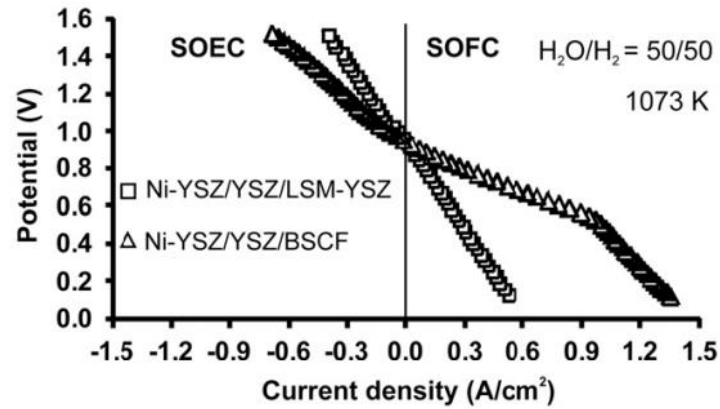


Figure 4 The I-V response of Ni-YSZ/YSZ/LSM-YSZ and Ni-YSZ/YSZ/BSCF in both electrolysis and fuel cell mode (1073 K, $H_2O/H_2=50/50$) [42].

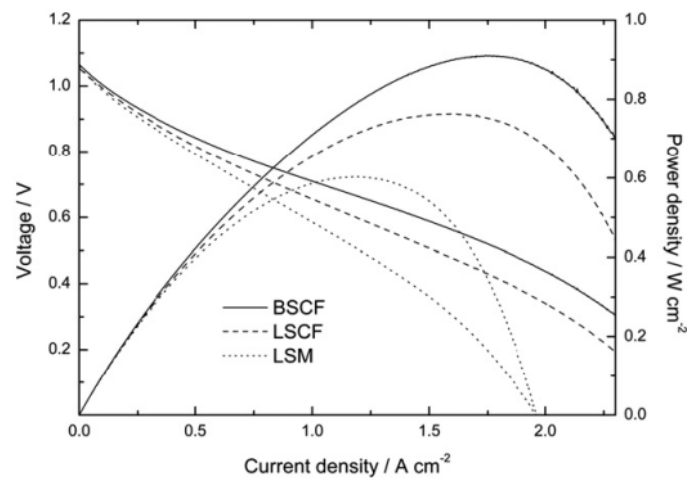


Figure 5 Performance of the anode-supported single SOFC having unsintered BSCF, LSM and LSCF cathodes at 1073 K, exposing to 97 H_2 % and 3% H_2O at the anode and ambient air at the cathode [43]

2.3.2.4 Support material

Metal-supported SOC has been developed. Thick metal layer which is used to support thin ceramic cell compartment to provide mechanical tolerance and stability

of the cell. The support material should be inexpensive with a proper gas flow filed. It should provide benefit greatly with increasing of mechanical property, redox tolerance and thermal cycling of the cell. As thinner layer of all electrodes, the total resistance of the cells is reduced and their electrochemical performance can be improved.

Tucker [7] reviews progress in metal supported-SOFC. It is suggested that material for support should have thermal expansion coefficient slightly higher than electrolyte material to enable rapid thermal cycling during operation. Moreover, oxidation resistance must be concern in the material selection.

Ferritic stainless steel has been widely used as support material in SOC. This support provides low cost, high oxidation resistance, stable in elevated operating temperature and compatible TEC with electrolyte. Unfortunately, Elemental inter-diffusion of Ni, Cr and Fe from the substrate and electrode occurs after annealing process. This solid diffusion results in a catalyst poisoning in anode at which the reason of low activity. When stainless steel is used as a support material in SOC, a diffusion barrier layer between fuel electrode and support can be a promising solution in the implementation of stainless-support SOC [8-11].

Ni-based material is also considered as the support material due to material compatibility between the support and electrode. However, Ni coarsening and Ni infiltration can occur after high-temperature heat treatment and degrade the cell's performance. Therefore a composite of Ni-alloy can be advantageous intern and contributes to extensive material choice in research and development.

Table 8 Summary of candidate support metals (Ni-based)

Materials	Thermal expansion coefficient or TEC (ppmK ⁻¹)	Reference
Ni	16.50	[7]
NiCrAl	16	[19]
NiCrAlY	15-16	[7]
NiFe (50:50)	13.70	[7]

Note : TEC of electrolytes (YSZ, CGO, LSGM) are 10–12 ppmK⁻¹ [7]

In this research, an alloy of nickel-iron (Ni-Fe) is used as support material to eliminate the limitation in stainless steel and Ni based material. To obtain better TEC matching between electrode and avoid solid diffusion as mentioned above, Kim et al. [13] successfully fabricate thin metal supported- SOFC by using Ni-Fe alloy as support material. The electrochemical performance is satisfactory result. Impurity oxide scale phase based on solid diffusion has not identified in microstructure. However, particle coarsening is detected in anode and cathode layer after operation at 2 Acm⁻², 1073 K, 10 h.

Li et al. [44] also observe redox tolerance of Ni-Fe alloy supported SOFC. The result reveals that cell exhibits excellent tolerance to redox cycles. Oxide scale, possibly be NiFe₂O₄ is identified on inner surface scaffold of porous Ni-Fe alloy as shown in Fig. 6. However, this oxide scale formation prevents inward oxidation of alloy metallic inside scaffold attribute to great oxidation resistance of this support.

Xu et al. [45] investigate the oxidation of Ni-Fe alloy in a humidified atmosphere of MS-SOFC operation. The presence of vapor in fuel electrode can promote oxidation during the process because of increasing of oxygen partial pressure. Fe_3O_4 which form on the surface by thermally grown oxide scale has influence electrical conductivity. Incidentally, the support provides sufficient electrical conductivity for this application and can be well employed in SOFCs.

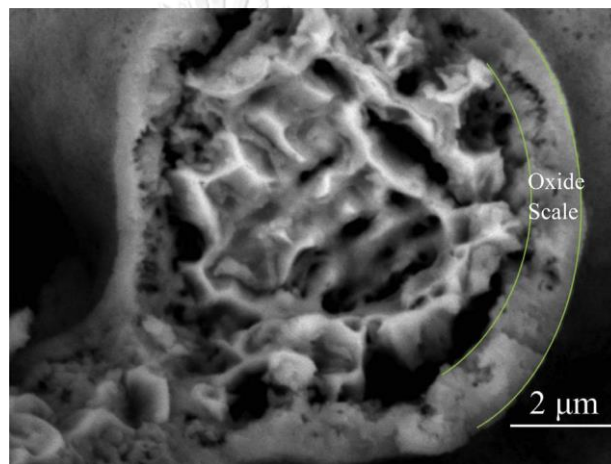


Figure 6 Cross-sectional microstructure of Ni-Fe alloy support oxidized at 873 K in air for 2 h [44].

2.3.3 Metal supported SOEC

2.3.3.1 Fabrication

Fabrication of metal supported SOEC has been developed to overcome some limitation of conventional cell and improve electrochemical performance and durability. In SOEC operation, the fabrication has concerned similarity as the fuel cell fabrication. Materials for each compartment are discussed in Section 2.3.2. There are various variables such as electrode's deposition technique, material compatibility between electrodes, fabricated condition and physical cell property. These variables must be controlled to accomplish the successful fabrication. Summary of previous

research in fabrication of SOFC and detail of common fabrication techniques are listed in Table 9 and 10 respectively.

Table 9 Summary of previous research in fabrication of SOFC

Cell Configuration	Layer fabrication				References
	Layers	Technique	Fabrication condition	Thickness (μm)	
1) NiFe/Ni-YSZ/YSZ/LSCF	Support : NiFe (50:50)	Tape casting	Co-firing with multi-steps - Green sheet laminated with 3 MPa of pressure at 70 °C, 10 min - Fired at 400 °C, 5 h in air (2 °C/min) - Fired at 1,300 °C, 5 h in air (3 °C/min) - Reduced at 800 °C, 1 h in wet H ₂ (-2 °C/min) - Cooled to room temperature (-3 °C/min) Apply a vertical loading at 1 kg/cm ²	120	[46]
	H ₂ Electrode : Ni-YSZ (6:4)			30	
	Electrolyte : 8YSZ			15	
	O ₂ Electrode : LSCF	Screen-printing	-		

Table 9 Summary of previous research in fabrication of SOFC (Continued)

Cell Configuration	Layer fabrication				References
	Layers	Technique	Fabrication condition	Thickness (μm)	
2) AISI 434L (STS)/ STS-YSZ/YSZ/LSTN-YSZ	Support : AISI 434L (STS)	Tape casting	<ul style="list-style-type: none"> - Green sheet laminated with 25 MPa of pressure at 60 °C, 10 min - Fired at 400°C, 12 h in air - Fired at 1,250 °C, 3 h in air Apply a vertical loading at 2 kg/cm ²	150	[47]
	Current collector : STS-YSZ (1:1)			20	
	H ₂ Electrode : LSTN-YSZ			15	
	Electrolyte : 8YSZ with 1wt.%Al ₂ O ₃			5	
	Buffer layer : GDC			RF-magnetron sputtering	
	O ₂ Electrode : LSCF	Screen-printing	- In-situ fired at 900 °C, 1 h during electrochemical testing process	10	
3) 430Ni-SDC infiltrated 430L STS/SSZ/LSFSc infiltrated SSZ	Support : 430L STS	Tape casting	1) STS/SSZ/Porous SSZ <ul style="list-style-type: none"> - laminating and co-sintering in a reducing atmosphere of 5% H₂/95% N₂ at 1320°C for 4 h 	260	[48]
	H ₂ Electrode : Ni-SDC infiltrated support	Infiltration		17	
	Electrolyte :SSZ	Tape casting	2) Electrodes infiltration <ul style="list-style-type: none"> - H₂ electrode : infiltrated 30 wt.% Ni-SDC (5 wt.% per time) - O₂ electrode : infiltrated 10 wt.% LSFSc (3 wt.% per time) - Dried and reduced at 850°C, 2 h in 5% H₂/95% N₂ 	30	
	O ₂ Electrode : LSFSc infiltrated porous SSZ	Tape casting and infiltration			

Table 9 Summary of previous research in fabrication of SOFC (Continued)

Cell Configuration	Layer fabrication				References
	Layers	Technique	Fabrication condition	Thickness (μm)	
4) Crofer22APU/ LST - GDC/GDC/ YSZ/GDC/ LSCF-GDC	Support : Crofer22APU	Chemical etching	-	200	[49]
	Porous material : Pre-coarsened GDC at 1200°C	GDC, Aremco 644-A	-	-	
	Metal coating : $\text{Y}_{0.2}\text{Sr}_{0.8}\text{TiO}_3$	Doctor blade coating	1,000°C, 1 h	-	
	H ₂ Electrode : LST-GDC	Doctor blade coating	1,000°C, 1 h	-	
	Electrolyte 1 : nanoparticle GDC		1,000°C, 1 h	-	
	Electrolyte 2 : nanoparticle YSZ	3-step coating process	950°C, 1 h	-	
	Electrolyte 3 : YSZ			-	
	Catalyst : Ni nitrate (2M)	5 times of impregnation (8wt.%)	900°C, 1 h	-	
	Buffer layer :GDC	Spin coating		-	
O ₂ Electrode : LSCF-GDC	Screen-printing	900°C, 1 h	-		
5) Ni supported/ Ni-YSZ/YSZ/LSCF	Support : Ni with 10wt.% pore	Tape casting	- Green sheet laminated at 70 °C, 10 min	200	[50]
	H ₂ Electrode : Ni-YSZ (6:4)		- Fired at 1,300°C, 3 h in air	30	
	Electrolyte : 8YSZ		- Reduced at 800 °C, 1 h in reducing atmosphere	20	
	O ₂ Electrode : LSCF	Screen-printing	- In-situ fired at 900 °C, 2 h during electrochemical testing process	-	

Table 9 Summary of previous research in fabrication of SOFC (Continued)

Cell Configuration	Layer fabrication				References
	Layers	Technique	Fabrication condition	Thickness (μm)	
6) 430LFSS/ Ni-YSZ/YSZ/LSM-YSZ	Support : 430L FSS		-	-	[51]
	H ₂ Electrode : Ni-YSZ (46:38) with 16 wt.% carbon black	Atmospheric plasma spraying (APS)	Number of spraying : 40 Duration of spray run : 1.84 min Deposition rate : 34.3 $\mu\text{m}/\text{min}$	63.09	
	Electrolyte : YSZ		Number of spraying : 50 Duration of spray run : 2.30 min Deposition rate : 26.0 $\mu\text{m}/\text{min}$	59.85	
	O ₂ Electrode : LSM- YSZ		Number of spraying : 80 Duration of spray run : 3.69 min Deposition rate : 11.1 $\mu\text{m}/\text{min}$	41.00	

Table 10 Comparison of SOFC fabrication techniques [52]

Process	Thickness	Components made	Advantage
Tape-casting	> 10 μm	Whole cell	Low-cost, co-sintering
Slip-casting	> 1 μm	Electrodes, electrolyte	Simple and inexpensive
Screen-printing	> 5 μm	Electrodes, electrolyte	Low cost, co-sintering
Wet powder spraying	> 5 μm	Electrolyte, electrodes	Low-cost
Dip-coating	> 1 μm	Whole cell	Low-cost
Spin-coating	> 1 μm	Electrodes, Electrolyte	Reproducible, uniform
Extrusion/co-extrusion	> 100 μm^{a}	Electrolyte, supports	Large, complex shapes
Hollow fiber	> 200 μm^{b}	Electrolyte, supports	Graded porosity
Freeze-casting	N/A	supports	Graded porosity
Dry-pressing	N/A	Whole cell	Low-cost
Catalyst impregnation	N/A	Electrodes	Nano-structured surfaces

^a The thickness of electrolyte fabricated by co-extrusion is about 20 μm .

^b The thickness of electrolyte fabricated by dual layer hollow fiber is about 10 μm .

As presented in Table 10, tape casting and dip-coating process provide applicable fabrication for whole cell compartments, low cost and simplest method for layer deposition. However, there are various variables which are controlled during process for successfully fabrication. Several importance variables are discussed following;

A) Effect of heat treatment process

Jin et al. [15] investigate anode-supported SOFC fabrication by tape-casting and co-firing technique. It is found that the decomposition of additive and shrinkage in green tapes clearly induces cracking and delamination of half-cell. Thermo-

gravimetric and differential thermal analyses (TG-DTA) and thermal dilatometry are used for monitoring decomposition of additives and linear shrinkage layers respectively. Additives are vaporized at temperature exceed 500°C. The results of shrinkage analysis also reveals that there are 2 steps during sintering process that 1) 30-600°C and 2) 800- 1400°C, which provide a large mismatch of linear shrinkage in all layers as shown in Fig. 7 for of Ni-SSZ gradient anodes/SSZ electrolyte for SOFC. Cracking and peeled electrolyte are found on cell by the rapid heating rate and shrinkage mismatch as shown in Fig. 8(B). To successfully fabricate the cell, sintering process are divided into 3 steps which are 1) 0.5°C/min (30- 600°C), 2) 3°C/min (600- 800°C) and 3) 1°C/min (800- 1400°C). Slow heating rate is found to help preventing defect formation. Therefore, shrinkage analysis of all layers must be identified to determination of step heating rate for successfully fabrication.

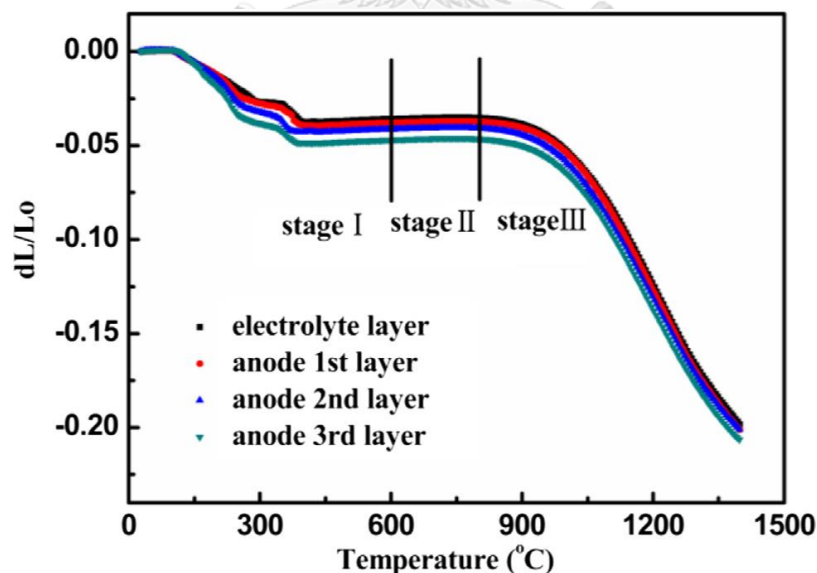


Figure 7 The results of shrinkage analysis in fabrication of Ni-SSZ gradient anodes/SSZ electrolyte for SOFC[15]

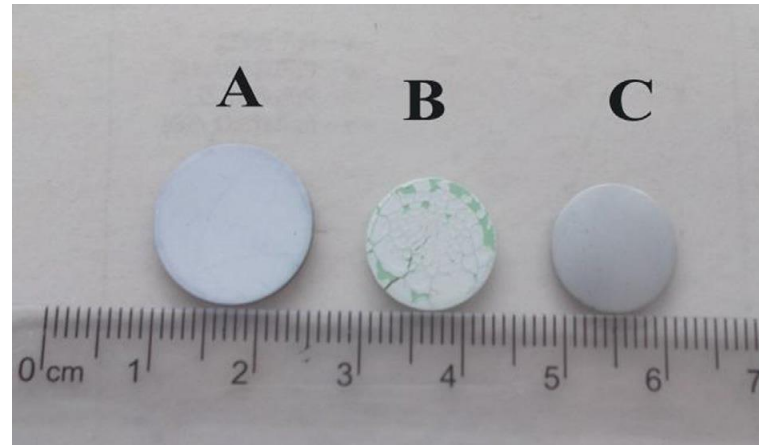


Figure 8 Photos of (A) green tape before sintered, (B) co-sintering cell at $3^{\circ}\text{C}/\text{min}$ (30- 1400 $^{\circ}\text{C}$), (C) co-sintering cell at $0.5^{\circ}\text{C}/\text{min}$ (30- 600 $^{\circ}\text{C}$), $3^{\circ}\text{C}/\text{min}$ (600- 800 $^{\circ}\text{C}$) and $1^{\circ}\text{C}/\text{min}$ (800- 1400 $^{\circ}\text{C}$) [15]

B) Effect of slurry composition

Slurry composition is the considerable parameter which carefully in manufacturing of SOC. This determines rheology of slurry and green layer mechanical properties [14]. Slurries have been identified properties by optimum ratio of starting powder, solvent and additives. The role of each composition and their properties should be clarified to successfully fabricate each layer. In common SOFC fabrication, slurry is consisting of starting powder, solvent and other additive (dispersant, binder, plasticizer and pore former). The starting powder is solid material which is used as main composition in green tape such as ceramic, metal and cermet. Solid particle is suspended in liquid phase as solute in solvent. Additives are added to enhance rheology and properties (particle network strength, viscosity and mechanical property) reach to the uniform and easily deposition. Behavior of slurry in tape

casting has several points that similar with screen printing ink. Therefore, some reviews of this parameter are conducted by screen printing fabrication research to understand rheology phenomenon. Effect of slurry compositions are revealed as follow:

1) Starting powder

To obtain a flatness and uniform layer, particle size and distribution of powder are critical parameters in slurry preparation. This identified the maximum solid content in slurry. High solid content attribute to excessive viscosity and difficulty in slurry mixing and green tape casting. Electrical performance is also enhanced by applying of nanocomposite which provides large surface area and excellent dispersion in electrode layer [53, 54]. However, low solid content is observed in screen-printing ink by using nano-sized powder. Due to high surface area, inter-particle interaction is increased and motivated defect in green film after printing [55].

2) Solvent

Solvent plays the critical role in slurry preparation. The volume of solvent is also effect directly to the rheological properties of slurry. Starting powder and solid additives require solvent to produce homogeneous phase in slurry. In addition to particle size and distribution of powder, solvent also determine maximum the solid loading (include starting powder and other additives) in slurry. Therefore, volume and solubility of solvent to be chosen has to be considered in slurry preparation to obtain steady slurry.

C) TEC and shrinkage matching

The defect which occurs during fabrication process can be generated from the mismatching of their TEC and shrinkage rate in annealing process. The TEC of each layer is determined by their material composition in solid content; ceramic, metal or cermet. However, the shrinkage of layer depends on all composition in slurry. Internal stress of their mismatch is created at interface of layers and caused of cracking and fracture on fabricated cell. Rapid heating also activates stress and evaporation of additives which are source of defect. Therefore, TEC and shrinkage mismatch must be minimized by low decomposition heat rate.

Lee et al [14] believe that shrinkage of support layer should be higher than electrolyte layer. Micro cracking has been occurred by higher shrinkage of electrolyte. Electrolyte is also low densification. Result of defect tape which is occurred by shrinkage mismatch is shown as Fig. 9. Coarse particle powder is substituted fine particle in their fabrication to reduce shrinkage rate. Controlling low heat rate in fast shrinkage range is also used for suppress the undesired phenomenon [15].

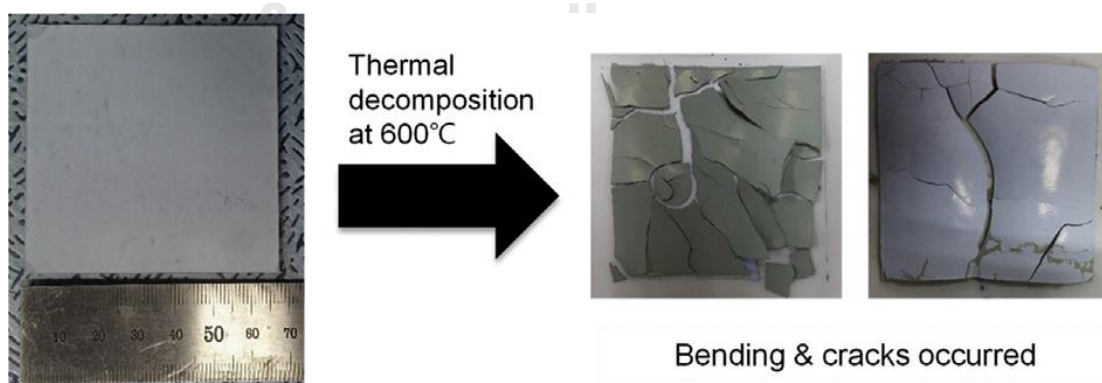


Figure 9 Tapes after thermal decomposition at 600°C for the fabrication of large-area unit cell [14]

In addition to shrinkage, TEC mismatch is also investigated and purposed as influence parameter in fabrication by Gondolini et al. [19]. They study the deposition of NiO-GDC layer on NiCrAl foam with screen-printing technique. It has found that the detachment between bi-layer occur between interlayer as shown in Fig. 10. The ascription is postulated that the detachment is made by expansion of foam support and shrinkage of cermet layer during sintering process up to 1273 K. To obtain the adhesion between both layers, TEC of cermet layer is increased to match the TEC of the alloy foam by increasing NiO content in ink composition. Shrinkage rate is also adjusted by compositional gradient cermet [53].

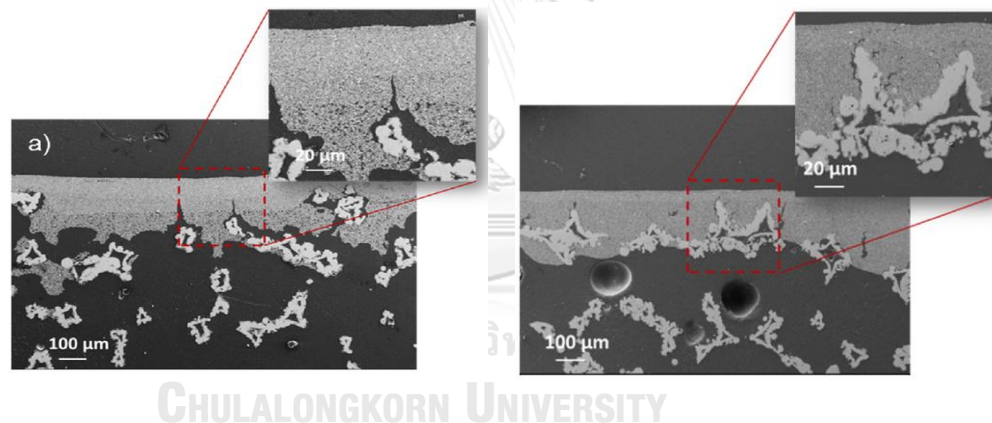


Figure 10 SEM micrograph of the polished fracture (left) non NiO gradient and (right) NiO gradient layer on NiCrAl foam support [19]

D) Reducing condition

Particle coarsening and oxide formation are undesired phase in H_2 electrode microstructure which is formed by high temperature annealing in oxidizing atmosphere. In order to obtain excellent electrochemical performance, a reducing atmosphere is conducted during fabrication before reaction testing to minimize the

defects. Reducing condition must also be specified to obtain successfully fabrication. 10%H₂ in N₂ at 800°C, overnight is the conventional reducing condition which provides sufficient reducing of oxide and avoid possible ignition.

2.3.3.2 Electrochemical performance

Electrochemical performance of SOC is enhanced by metal-supported cell design. To understand this improvement, metal supported-SOFC research is reviewed and summarized in following subsections.

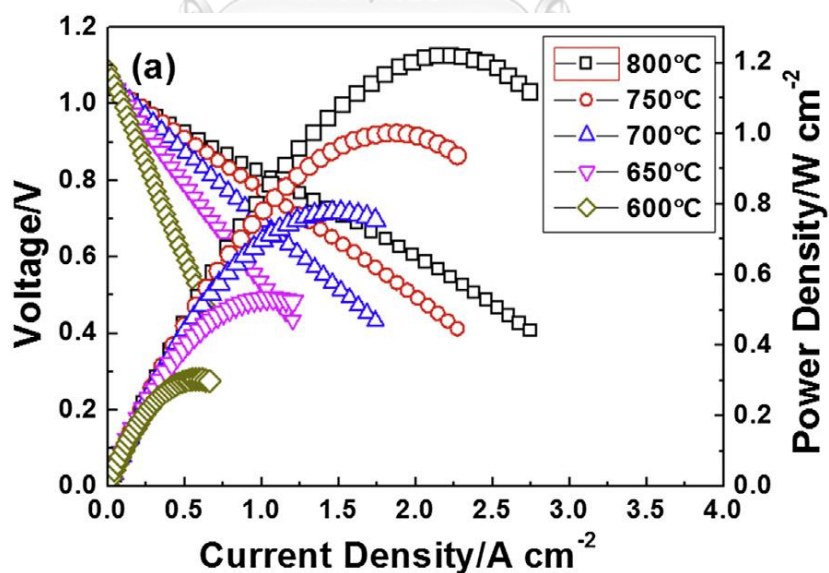
A) Current density

The one of electrochemical performance results which is taken first priority for comparison and discussion is current density. It shows how much of current is produced or consumed in reaction area by electrochemical reaction. In SOEC operation, if current is highly consumed at low potential (above OCV), electrolytic cell can provide great performance and produce high primary product. Table 11 shown summary of electrochemical performance of metal supported-SOC.

For consequence the effect of operating temperature, electrochemical performance has efficiently proceeded at increasing of temperature followed principle of thermodynamics. The trend of polarization curve along different temperature is shown in Fig. 11.

Table 11 Reviewing of electrochemical performance of metal supported-SOC

Cell configuration	Feed gas	Temperature (K)	Current density (Acm^{-2})	Voltage (V)	Reference
Fe26Cr / Ni-GDC/YSZ/LSCF	97% H_2 /3% H_2O	1073	2.2	0.7	[56]
Ni-SDC infiltrated 430L STS/SSZ/LSFSc infiltrated SSZ	97% H_2 /3% H_2O	1073	2	0.6	[48]
Ni supported/ Ni-YSZ/YSZ/LSCF	97% H_2 /3% H_2O	1073	1.5	0.6	[50]
NiFe/Ni-YSZ/YSZ/LSCF	97% H_2 /3% H_2O	1073	0.7	0.6	[46]
Porous Ni/Porous STS/ Ni-GDC/GDC/LSC-YSZ	97% H_2 /3% H_2O	723	0.4	0.6	[57]

**Figure 11** Polarization curves of Ni-SDC infiltrated 430L STS/SSZ/LSFSc infiltrated SSZ metal supported-SOFC measured at 600- 800°C [48]

B) Electrochemical impedance spectra (EIS)

Electrochemical impedance spectra or EIS provides all resistances which are total resistance, ohmic resistance from all electrodes and polarization resistance.

Li et al. [44] studies the performance of Ni-Fe alloy supported SOFC by low cost tape-casting. Their EIS result is shown in Fig. 12. It is found that resistances decreases with increasing of temperature. The polarization resistances are gradually low in which the cell is well fabrication. The ohmic resistances are also low.

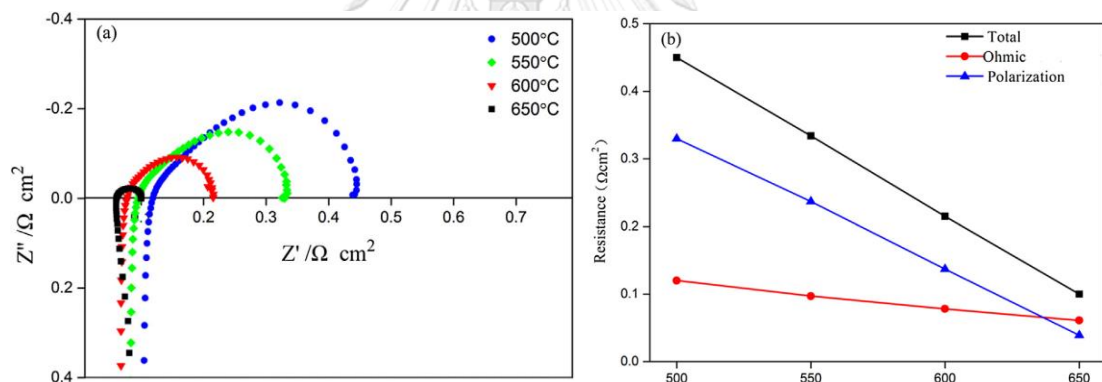


Figure 12 Total (R_T), ohmic (R_{Ω}) and polarization (R_p) resistances of the Ni-Fe/Ni-GDC/GDC/LSM-BSCF SOFC as a function of testing temperature obtained from measured electrochemical impedance spectra at open circuit voltage and various temperatures between 500 and 650 $^{\circ}\text{C}$ [44]

C) Durability

Tucker [58] fabricates metal supported- SOFC that stainless steel as support. Porous YSZ backbones for H_2 and O_2 electrodes are deposited on both side of dense YSZ layer. Electrode catalysts are infiltrated to both backbones which are

$\text{La}_{0.15}\text{Sr}_{0.85}\text{MnO}_{3-\delta}$ (LSM) on the O_2 electrode side and 80 vol% $\text{Sm}_{0.2}\text{Ce}_{0.8}\text{O}_{2-\delta}$ -20 vol% Ni (SDCN) on the H_2 electrode side as shown the SEM image in Fig. 13.

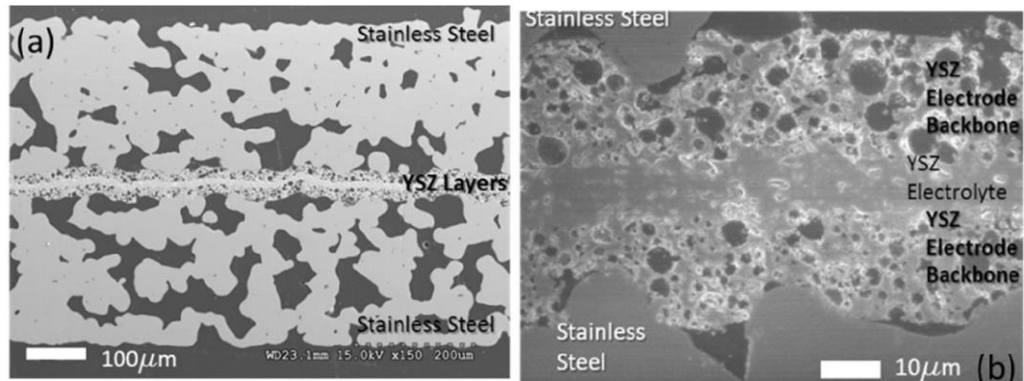


Figure 13 SEM image of (a,b) polished cross section of STS/SDCN-YSZ/YSZ/LSM-YSZ/STS metal supported-SOFC structure after sintering and before catalyst infiltration [58]

As results in Fig. 14, long term operation performance at 650, 700 and 750°C is conducted by LSM and SDCN as infiltrated electrodes for O_2 and H_2 electrode, respectively. It is not surprising that severe degradation of current density is obtained at 750 °C. Coarsening of catalyst and increasing of Cr deposition in O_2 electrode are found at higher temperature. It is also confirmed that this degradation must be attributed to microstructure evolution by the stable of OCV in Fig 14(b). This stable OCV is indicated that the sealing of cell is maintained along operation. Therefore, 700°C of operating temperature is chosen in other effect experiment.

Type of infiltrated catalyst on O_2 electrode side is investigated as results shown in Fig 15. SDCN/SDCN cell provided stable operation than LSM/SDCN. Although, LSM/SDCN cell displays higher electrochemical performance at initial operation.

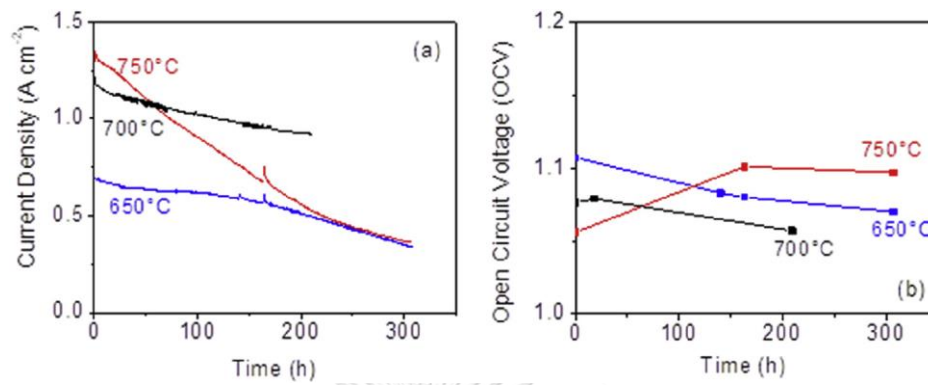


Figure 14 Temperature-dependence of the initial cell stability of LSM/SDCN cell. (a) Current density at 0.7 V and (b) OCV for cells operated potentiostatically [58]

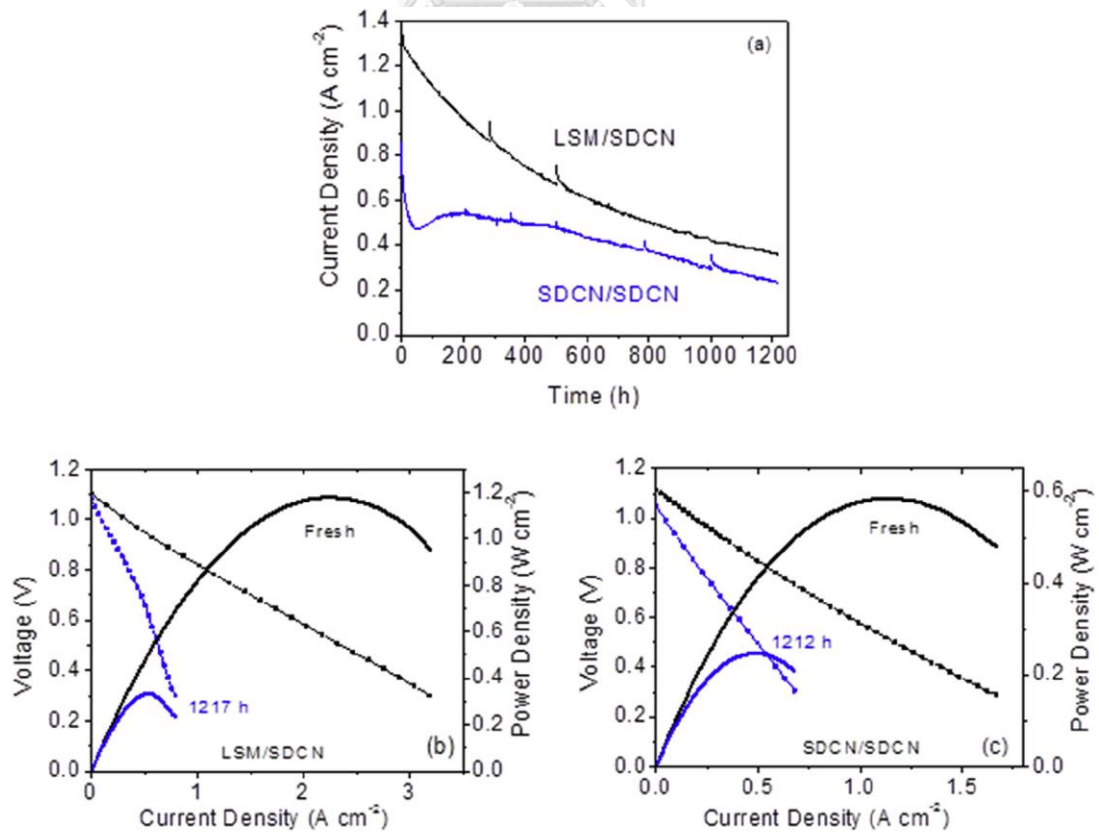


Figure 15 Long-term operation: (a) Current density at 0.7 V for cells operated potentiostatically at 700°C with LSM/SDCN (black) and symmetric SDCN/SDCN (blue) catalysts. Current step polarization curves at 700°C before (black) and after (blue) long-term operation for (b) LSM/SDCN and (c) SDCN/SDCN [58]

2.4 Characterization

2.4.1 Cell Characterization

2.4.1.1 Rheology of slurries

Electrode slurry which is included electrode powders and additives is characterized properties by rheological characterization. Slurry rheology is the one of several factors which has impacted on the quality of casted layer on the substrate. This performed as non-Newtonian fluid which their viscosity is varied dependent on shear rate, shear stress and time. Therefore, general viscosity measurement is not insufficient to identified the slurry characterization [55]

Consequence of non-Newtonian fluid of slurry, steady-state properties is used as analysis data in slurry characterization. Shear stress at any shear rate is implied by rheometer in the analysis process as shown in Fig. 16.

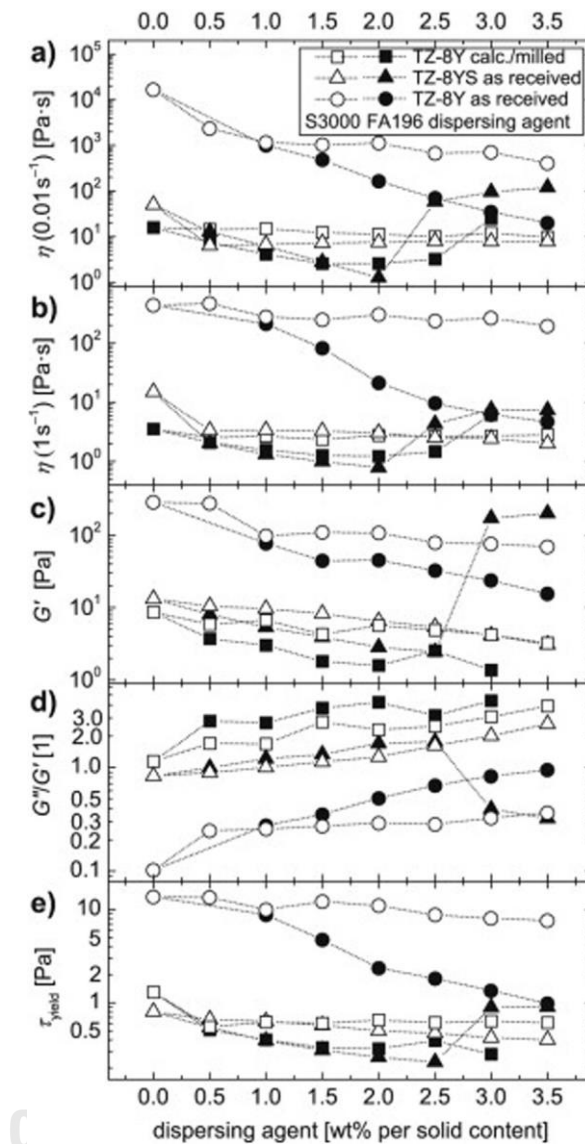


Figure 16 Rheological properties of YSZ inks at 333 K as a function of dispersant content for Solsperser S3000 and Nuosperser FA196 dispersants and three different YSZ powders of TZ-8Y, TZ-8YS and TZ-8YS having surface areas of 12.3, 6.2 and 3.1 m²/g, respectively.

(a) Viscosity η at a shear rate of 0.01 s⁻¹, (b) Viscosity η at a shear rate of 1 s⁻¹, (c) Storage modulus G' , (d) Damping factor G''/G' and (e) Physical yield stress [55]

Meakin and Hukins [59] investigate the rheological properties of poly(2-hydroxy methacrylate) (pHEMA) as a function of water content which is non-Newtonian fluid. The characterization is conducted by rheometer analysis. The schematic of rheometer is shown in Fig. 17.

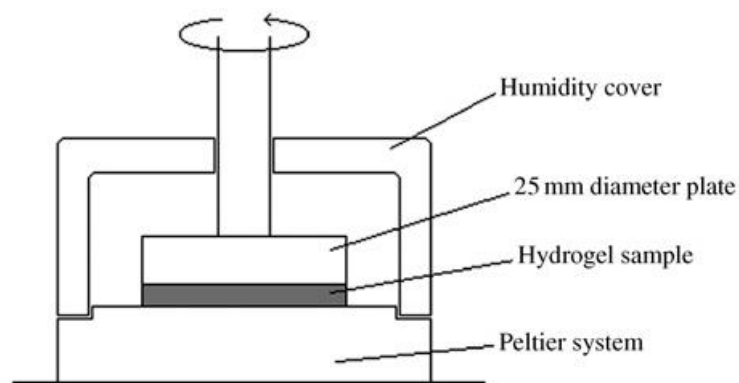


Figure 17 Schematic of rheometer [59]

The rheometer system consisting of a fixed plate (Peltier plate) in which sample is placed, and an upper rotating plate on sample which is controlled gap distance between two plates and the sample. Excess sample around plate is then trimmed away by small blade. Example of station testing after trimming is shown in Fig. 18. Shrivastava [60] also summarizes the effect of parameters on viscosity curve as shown in Fig. 19.



Figure 18 Proper loading of sample after closing the gap for cone and parallel plate geometry systems [61]

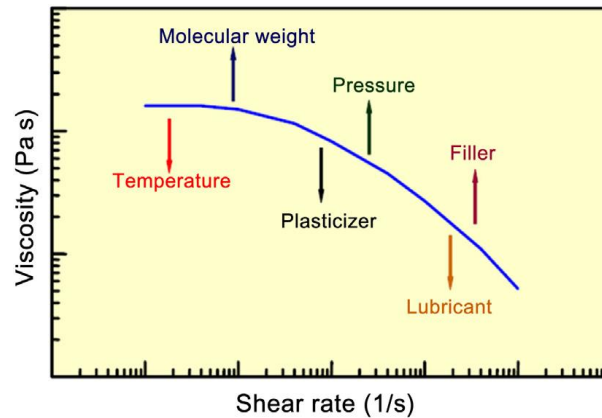


Figure 19 Effects of various parameters on different section of a typical viscosity curve [60]

2.4.1.2 SEM-EDX

Scanning electron microscope or SEM is an electron microscopic instrument which is allowing morphology image of specimen. Abd Mutalib et al. [62] report the principle of SEM. They summarize that an image is produced by reaction of electron beam and sample surface. SEM configuration is included electron source, electromagnetic lenses, electron detector, sample chamber, and the computer display as shown in Fig. 20.

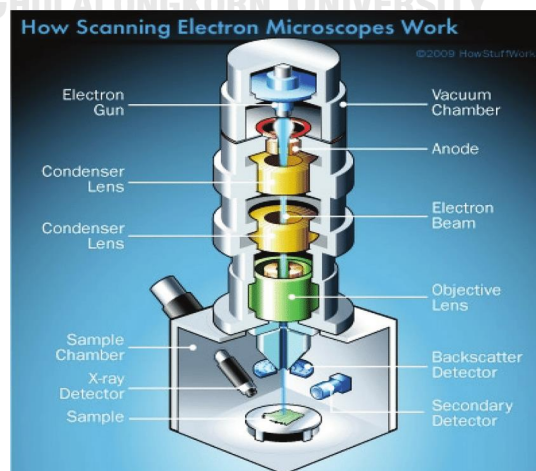


Figure 20 SEM Configuration [63]

In the meanwhile, energy dispersive X-ray spectroscopy or EDX is quantity analysis which is the detective instrument for element mapping of sample. EDX is detected elements that possess higher atomic number more than Boron. Therefore, element composition and their position on specimen are obtained by this technique.

Application of SEM-EDX in ceramic material is basic technique for morphology characterization. Nickle oxide (NiO) and cerium gadolinium oxide (CGO) are identified by the different contrast image between both elements in respective layers (Fig. 21). Element mapping which is characterized by EDX is also obtained by a plot of relative elemental distribution along a horizontal line in the scan area of the sample as shown in Fig. 22.

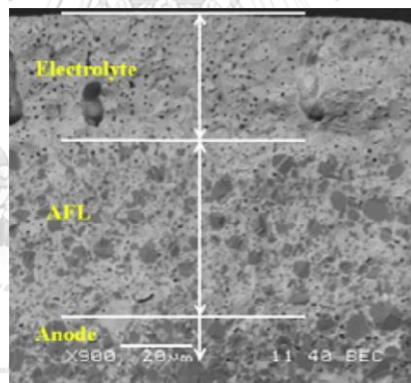


Figure 21 Difference in contrast of the NiO and CGO is visible with the darker particle denoting NiO [63]

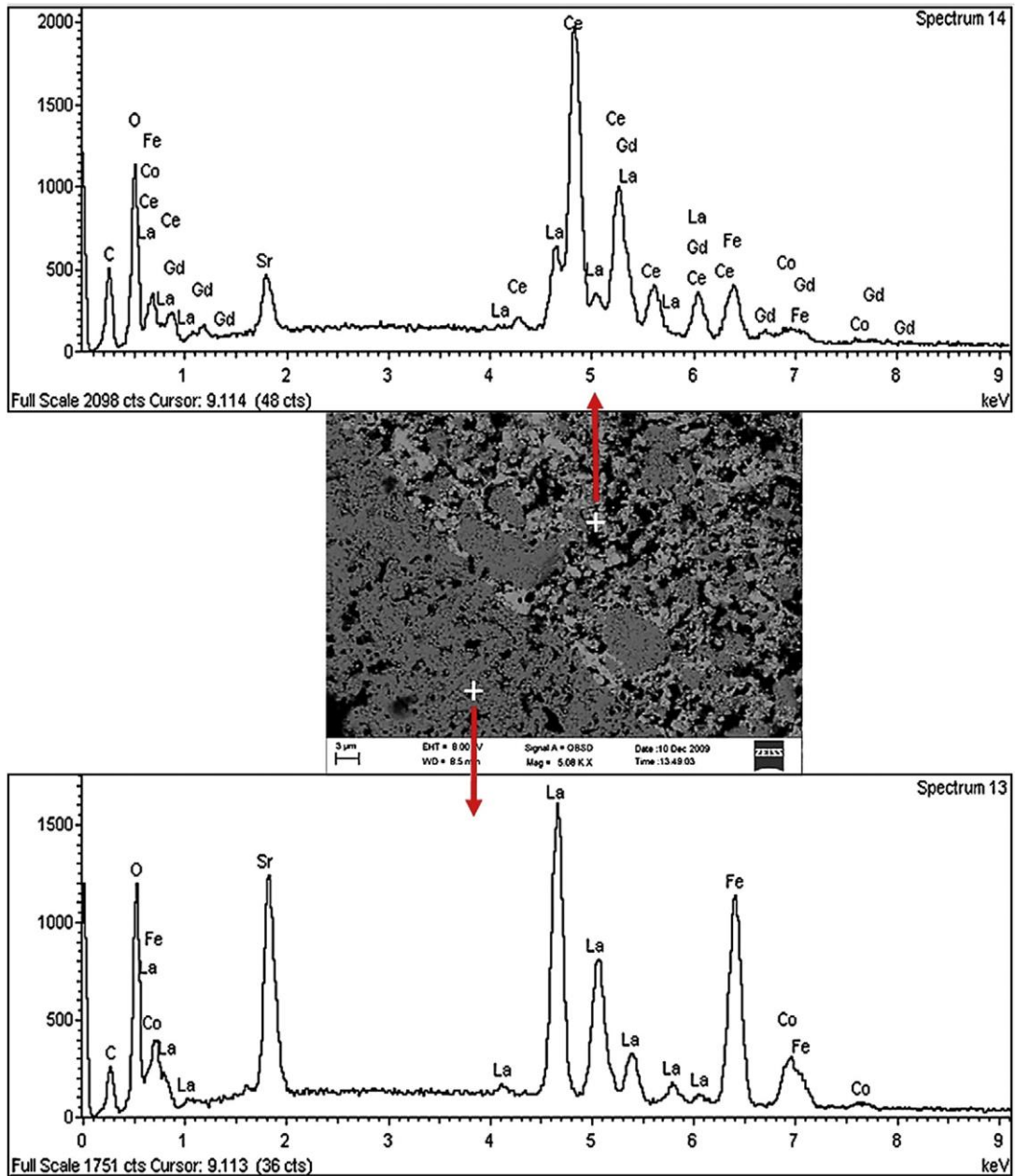


Figure 22 Energy dispersive X-ray analysis of different points in the same scan area showing different elemental composition of each points [63]

2.4.1.3 XRD

X-ray Diffractometer (XRD) is an instrument for crystalline analysis of sample. This technique is dominated by X-ray diffraction in crystalline plane as shown in Fig. 23. Each crystalline phase consist of different unit cells. When X-ray diffracted to lattice planes, the absorbed energy of detective ray is identified as peak pattern (Fig. 24) for each crystalline structure. The crystalize size is calculated by Scherrer's equation as shown in Eqs.(11) and crystalline phase pattern.

$$FWHM(2\theta) = \frac{b\lambda}{D \cos\theta} \quad (11)$$

where FWHM is the full wide of the highest peak in XRD analysis pattern, 2θ is the scattering angle in radians, λ is the wavelength, b is the constant value which is 0.89 or 0.94 depending on function of fitting in pattern and D is the dimension of the crystallites.

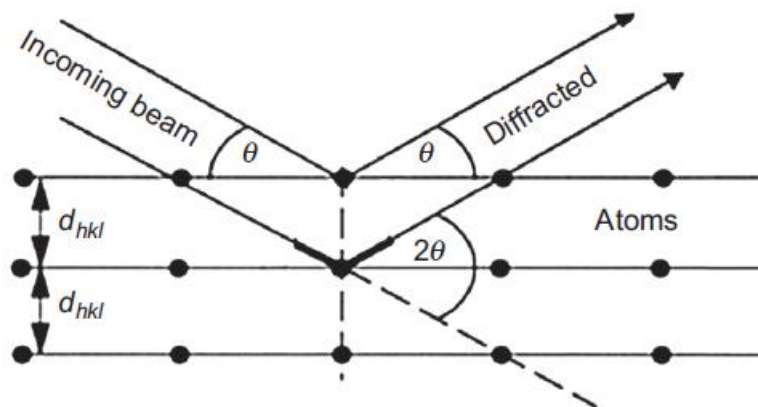


Figure 23 X-ray diffraction in crystalline structure [64]

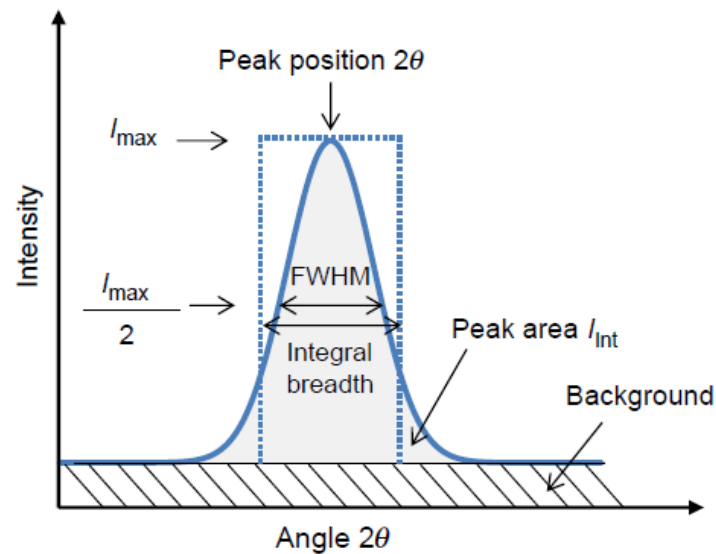


Figure 24 Diffraction peak and information content [64]

2.4.1.4 TGA

Thermogravimetric analysis or TGA is the technique involved the mass change of substance under controlled condition. It uses for thermal circumstances investigation such as oxidation, reduction and decomposition. TGA can be also utilized in chemical reaction for kinetics determination.

Loganathan et al. [65] review that there are several factors that influence to mass changing during analysis process. The factors are consist of 1) amount of sample, 2) physical structure of sample, 3) sample holder, 4) nature of analysis atmosphere, 5) pressure and 6) heating or cooling rate condition. A general schematic of TGA station is shown as Fig. 25.

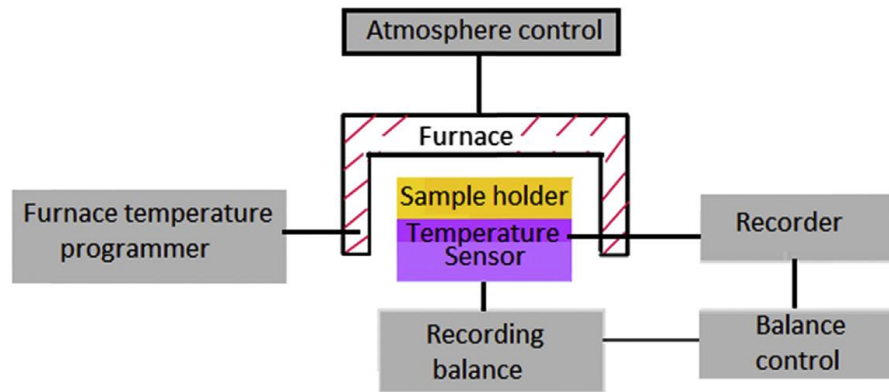


Figure 25 Schematic of TGA station [65]

TGA application in capability of oxidation is used in this research for substrate and electrode characterization. Waldbillig et al. [66] investigate the effect of Ni content in fine anode structure on oxidation rate by TGA technique. The TGA curve is shown as Fig. 26. Condition for analysis is controlled at 750°C in air.

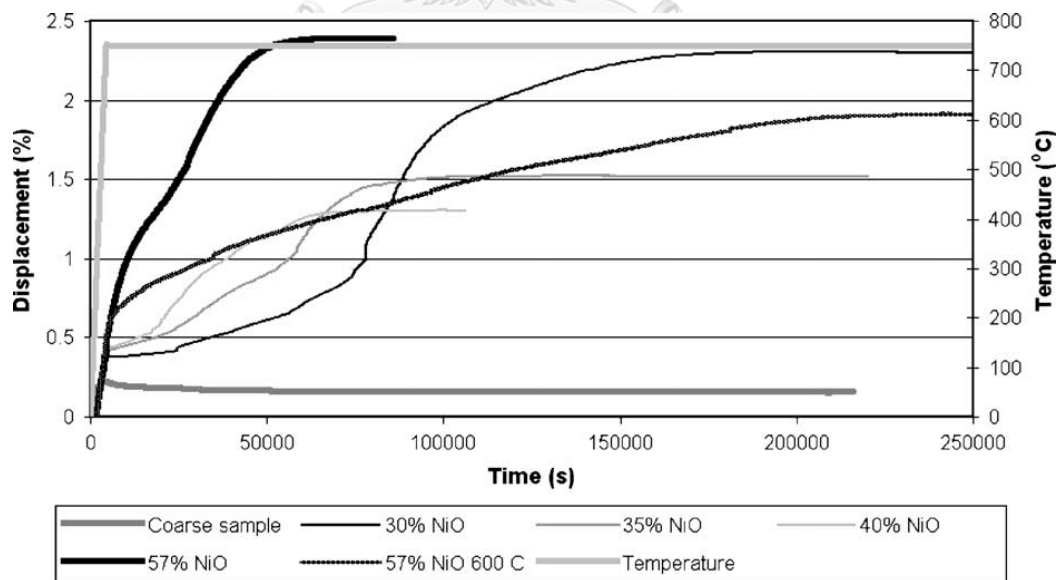


Figure 26 Re-oxidation TMA of fine structured anode sample [66]

2.4.1.5 UTM

In order to understand the mechanical properties of substrate, universal testing machine is used in the investigation of stress-strain curve. A typical stress-strain curve is shown in Fig. 27. Some critical point which is represented matter behavior is also indicated. The detail of each critical point is referred as following [60];

- 1) Point A as “Proportional limit”
- 2) Point B as “Elastic limit”
- 3) Point C as “Yield point”
- 4) Point D as “Ultimate point”
- 5) Point E as “Break point”
- 6) Point F as “Strength at yield”
- 7) Point G as “Elongation at yield”
- 8) Point H as “Ultimate strength”
- 9) Point K as “Strength at break”

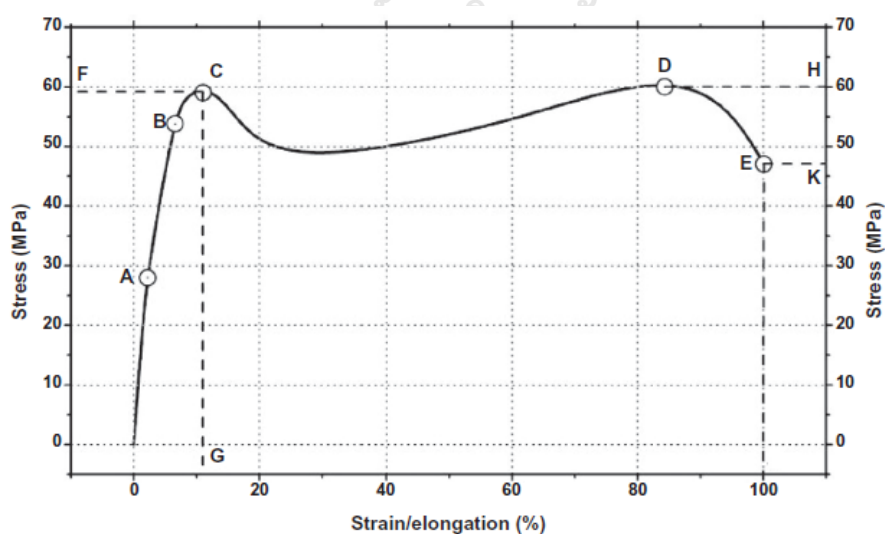


Figure 27 Typical stress-strain curve of a semi-crystalline material with some critical measuring points [60]

Cho et al. [46] study the mechanical property of thin metal supported- SOFC. This is conducted by 3-point bending testing that shown as Fig. 28. The cell is placed on the gap between a metal jig. A load with constant movement speed is applied above the cell to generate the stress-stain curve of action.

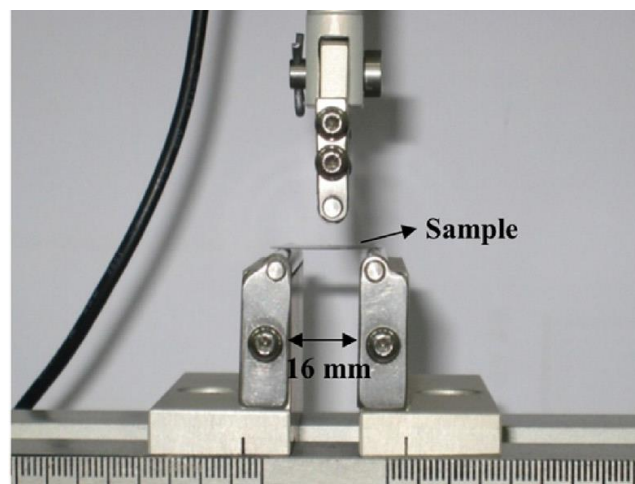


Figure 28 Photo images of the setup for 3-point bending test of cell [46]

CHAPTER III

EXPERIMENTAL

In this research, Nickel-Iron alloy supported solid oxide electrolysis cell (SOEC) was fabricated by wet chemical coating and firing process that included tape casting, dip-coating and screen-printing for H₂ electrode, electrolyte and O₂ electrode respectively. The experiment for fabrication divided into 3 parts: Fabrication and characterization of electrolyte-supported, Ni-Fe-alloy-foam supported SOEC and cathode-supported SOEC. Investigation of electrochemical performance of fabricated cell was also part of this experiment.

3.1 Fabrication and characterization of electrolyte-supported SOEC

Scandium cerium- and gadolinium-doped zirconia (Sc_{0.1}Ce_{0.05}Gd_{0.05}Zr_{0.89}O₂, SCGZ) was fabricated into an electrolyte-supported SOEC. Three grams of SCGZ powder (Kceracell, Chungcheongnam-do, Republic of Korea) were pressed at 24 MPa into a pellet with diameter of 25 mm and thickness of 1.4 mm. The pellets were then sintered at 1373 K to 1673 K for 4 h. The electrolyte pellet with sintering additive was fabricated using the same method when 0.5 wt.% CuO was added into the SCGZ starting powder. The relative density of the sintered electrolyte pellet was calculated following Equation (12).

$$\text{Relative density} = \frac{\text{Actual density}}{\text{Theoretical density}} \times 100 \quad (12)$$

where actual density is the bulk density of sintered cell. The theoretical density was obtained by lattice parameter from X-ray diffraction (XRD) analysis (Bruker D8 Advance, Massachusetts, US).

Platinum (Pt) conductive paste (70 wt.% Pt, Nexceris) was coated on the both sides of the electrolyte pellet as electrodes with thickness and area of $\sim 30 \mu\text{m}$ and $\sim 0.5 \text{ cm}^2$, respectively. The schematic of cell component was shown as Fig. 29. The cell was then fired at 1173 K for 2 h. It should be noted that the choices of electrode used depend on the deposition technique, the operating temperature, and the type of conductivity. Using gold or platinum as working electrode was reported to perform well at high temperature but below 873 K they are relatively blocking oxygen [27].

Phase and crystallite size of sintered electrolyte were determined using XRD with $\text{CuK}\alpha$ source (Bruker D8 Advance, Massachusetts, US). The microstructure of the samples was investigated using SEM (Hitachi S-3400N JEOL model S-3400, Tokyo, Japan). The average grain sizes were calculated by linear intersection method.

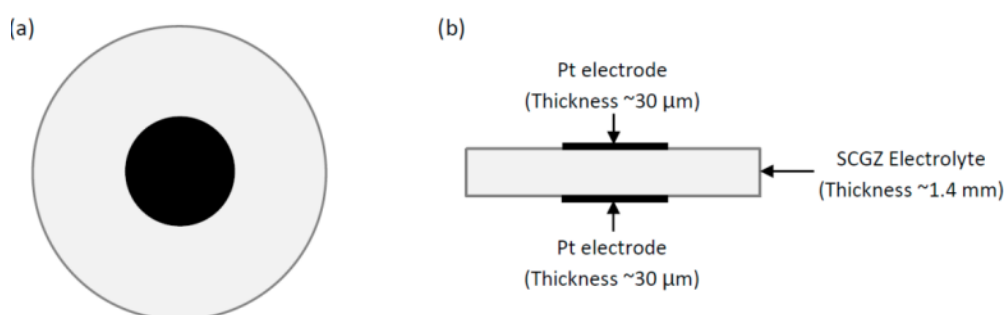


Figure 29 Schematic drawing of electrolyte-supported SOEC; (a) top view, (b) side view

3.2 Fabrication and characterization of Ni-Fe-alloy-foam-supported SOEC

In order to fabricate an alloy foam supported SOEC, electrode slurries were prepared by mixing of starting powder, solvent, and other additives. Each electrode layer was layer-by-layer coated on the foam support by wet chemical coating technique.

3.2.1 Preparation of alloy foam support

The Ni-Fe (60:40) alloy foam (Tmax Battery Equipments Limited, People's Republic of China) having a 5-130 ppi porosity, 25 mm diameter and 1 mm thickness was used as the support. The alloy foam was cut into disc and was punched in vertical direction to increase packing density and reduce surface roughness.

The oxidation tolerance of the support materials was measure in term of degree of oxidation (DoO) which was done at 1073 K under atmosphere. The degree of oxidation of supports was calculated following equation (13):

$$\text{DoO}(\%) = \frac{m_{\text{oxidized}}(t) - m_{\text{initial}}}{m_{\text{oxidized}} - m_{\text{initial}}} \quad (13)$$

when $m_{\text{oxidized}}(t)$ is the mass of sample at a certain time during analysis. m_{initial} and m_{oxidized} are the mass of sample at the initial and final of the oxidation, respectively. The change in mass of the alloy foam support was also determined for the samples after firing at 1573 K to 1673 K as well as the samples after firing and subsequently reducing in 10 vol.%H₂ at 1073 K for 12 h. Stress-strain curves of the alloy foam support were also identified by universal testing machine (UTM, ASTM D695, USA).

3.2.2 Preparation of cathode slurry and fabrication of the cathode layer

NiO (Sigma-Aldrich, USA) and $\text{Sc}_{0.1}\text{Ce}_{0.05}\text{Gd}_{0.05}\text{Zr}_{0.89}\text{O}_2$ (SCGZ, Kceracell, Republic of Korea) were used as cermet starting powder. For cathode slurry, the cermet powder was mixed with toluene-ethanol binary solvent and polymeric additives. Terpineol (Sigma-Aldrich, USA), and polyethylene glycol 400 (PEG 400, Sigma-Aldrich, USA) were used as dispersant and plasticizer, respectively. The slurry was mixed using zirconia ball-milling at room temperature for 24 hr. After that, cathode slurry was coated layer-by-layer on the alloy foam support at which cathode green layers were formed as multi-layers with a gradient of solid content ranging from 50-70 wt.%. High solid content provided viscous slurry was deposited as the first layer on the support. The viscous slurry could build a thick layer on the alloy foam to prevent slurry sweeping through the highly porous structure. The lower solid content slurries were then coated on top to create a smooth surface layer. NiO content in the slurry (NiO:SCGZ) was also varied ranging from 60 to 75 wt.% to obtain thermal expansion coefficient gradient in the cathode layers. The gap between blade and surface deposition was 100-200 μm . The coated green cathode layers on the alloy foam support was dried and fired at 1373 K, 2 h (1 Kmin^{-1}) with uniaxial loading 0.5 kgcm^{-2} to prevent internal stress and rapid shrinkage which introduced a defect in the cell.

3.2.3 Preparation of electrolyte slurry and fabrication of the electrolyte layer

The SCGZ electrolyte powder was mixed with 0.5-1 wt.% of CuO as sintering additive (Sigma-Aldrich, USA). The electrolyte slurry was prepared by mixing the powder with xylene-butyraldehyde solvent and polyvinylpyrrolidone (PVP, Sigma-Aldrich, USA) at 343 K for 24 h. Polyvinyl butyral (B-98, Sigma-Aldrich) and PEG 400 as

binder and plasticizer, respectively, were then added and stirred for another 24 h. The electrolyte slurry was deposited on the cathode layer by dip-coating. The half-cell was sintered at 1623 K for 4 h with the same uniaxial loading in the cathode firing process. Thin electrolyte layer ($\sim 30\text{-}50\ \mu\text{m}$) were formed.

3.2.4 Preparation of anode slurry and fabrication of the anode layer

$\text{Ba}_{0.5}\text{Sr}_{0.5}\text{Co}_{0.8}\text{Fe}_{0.2}\text{O}_{3-\delta}$ (BSCF, Kceracel, Republic of Korea) was used as anode material demonstrating the high electronic and ionic conductivity [43]. The anode slurry which was contained BSCF powder and terpeneol at weight ratio of 1 to 1 was coated on the sintered cell by screen-printing with $\sim 0.5\ \text{cm}^2$ electrode active area.

The viscosity of cathode and electrolyte slurries was determined using a rheometer (TA Instruments, USA) with a 25 mm diameter steel disk plate. Viscosity-shear rate curves were obtained by sweeping shear rate from 0.02 to $70\ \text{s}^{-1}$ with the gap between plates at $500\ \mu\text{m}$. Thermal behavior of green layers was investigated with the weight loss and the heat of reaction between 298-1273 K using thermal gravimetric analysis (TGA, TA Instruments SDT Q600, USA). The microstructure and morphology of the fabricated cell was performed by scanning electron microscopy (SEM, Hitachi S-3400N JEOL model S-3400, Tokyo, Japan).

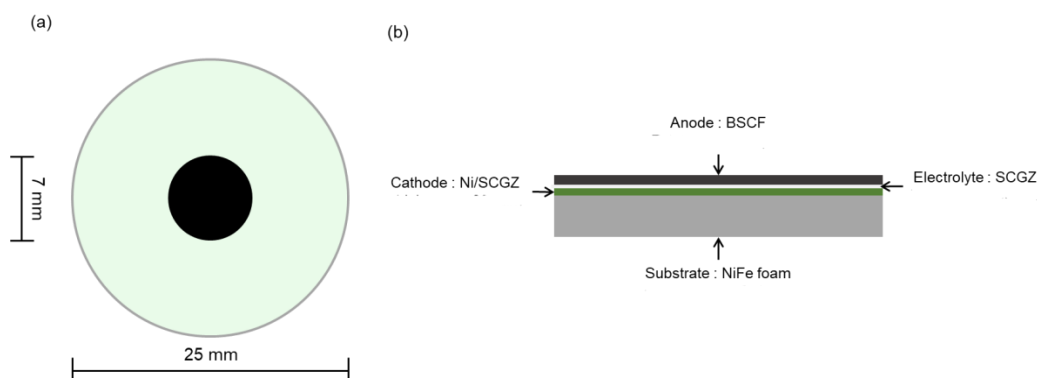


Figure 30 Schematic drawing of Alloy foam-supported SOEC ;(a) top view, (b) side view [67]

3.3 Fabrication and characterization of cathode-supported SOEC

NiO (Sigma-Aldrich) and SCGZ cermet powder in a weight ratio of 60:40 were ball-milled for 24 h in ethanol medium. After that, the slurry was dried at 105°C, overnight to obtain green powder. A cermet pellet in 25 mm diameter was fabricated by uniaxial compression with 3 g of green powder at the same condition in section 3.1. The green body was fired at 1,100 °C, 2 h. SCGZ electrolyte slurry was then coated on fired pellet and sintered at 1,450 °C, 4 h. Heating rate for both annealing process was 5 °C/min. BSCF anode was prepared by screen printing on sintered half-cell. The morphology of fabricated cells is investigated using SEM (Hitachi S-3400N JEOL model S-3400, Japan).

3.4 Electrochemical performance measurement

3.4.1 Electrochemical performance measurement of electrolyte-supported SOEC Fabrication

Electrochemical performance was measured in a controlled temperature from 873 K to 1173 K with the feed containing steam and hydrogen at the ratio of 70:30. The fabricated cell was attached with Pt mesh and wire (Kceracell, Chungcheongnam-do, Republic of Korea) for electrical connection. The cell was placed on a cell holder with high temperature sealant (Ceramabond 552, Aramco, Houston, TX, USA). The holder was installed inside a vertical furnace (Chavachote, Bangkok, Thailand). HPLC liquid pump (Teledyne SSI, State College, Pennsylvania, US) was used to supply deionized water through a heated-pipe for

steam generation in the system. Linear sweep voltammetry procedure was applied to generate current/voltage (I-V) curves by controlling the potential from 0.4 V to 1.8 V with a scan rate of 20 mVs⁻¹ (Metrohm Autolab, Utrecht, The Netherlands).

Resistance was determined by the slope of current-voltage (I-V) curves and the conductivity of fabricated cell (σ) was then calculated using Equation (14).

$$\sigma = L/RA \quad (14)$$

where σ is the conductivity (S cm⁻¹); L is the thickness of fabricated cell (cm); R is the cell resistance (Ω); and, A is the area of electrode (cm²).

The activation energy of conduction (E_a) was obtained by using Arrhenius, Equation (15) with conductivity value as mentioned above.

$$\sigma T = A \cdot \exp\left(-\frac{E_a}{RT}\right) \quad (15)$$

where σ is the conductivity (S cm⁻¹); T is the absolute temperature (K); A is a constant; E_a is the activation energy of conduction (J mol⁻¹); and R is the gas constant (8.314 J K⁻¹ mol⁻¹). It should be noted that the activation energy of conduction in this study was calculated from I-V curves ranging from open circuit voltage to 1.8 V. The slope of I-V curve is total resistance, which includes electrode resistance. The I-V slope was not constant and was derived using a linear regression with R-squared (R^2) ranging from 0.90–0.97. In this study, Pt was applied as both electrodes (Pt/Electrolyte/Pt) and was expected to provide rather low resistance at operating conditions.

3.4.2 Electrochemical performance measurement of Ni-Fe-alloy-foam-supported SOEC

Platinum (Pt) conductive paste (70 wt.% Pt, Nexceris), mesh and wire (Kceracell, Republic of Korea) were attached on the both side of fabricated cell for electrical connection. The fabricated cell was installed in test station consisting of alumina cell holder with high-temperature sealant (Ceramabond 552, Aramco, USA) inside a furnace (Chavachote, Thailand). The detail setup can be found in our previous work [20]. The electrochemical performance was measured at 873-1173 K with feed containing 60-80 vol.% of steam at constant hydrogen content (20 vol.% H₂, balanced N₂). Deionized water was supplied for steam generation using high performance liquid chromatography pump (Teledyne SSI, USA). A heated-tube was used as steam generator. A potentiostat (PG310 Metrohm Autolab, Netherlands) was used to evaluate the cell performance. Linear sweep current technique was applied to generate polarization curves by potential applying from 0.4 V to 1.8 V with a scan rate of 20 mVs⁻¹. Electrochemical impedance spectroscopy (EIS) analysis were performed in both electrolytic mode (0.6 V) and galvanic mode (1.1 V) with excitation in the frequency ranges were investigated from 0.1 MHz to 0.1 Hz using a sinusoidal signal amplitude of 0.01 mVrms. In addition, the durability of the fabricated cell was investigated using chronopotentiometry technique at 800°C with 70 vol.% of steam for 10 h.

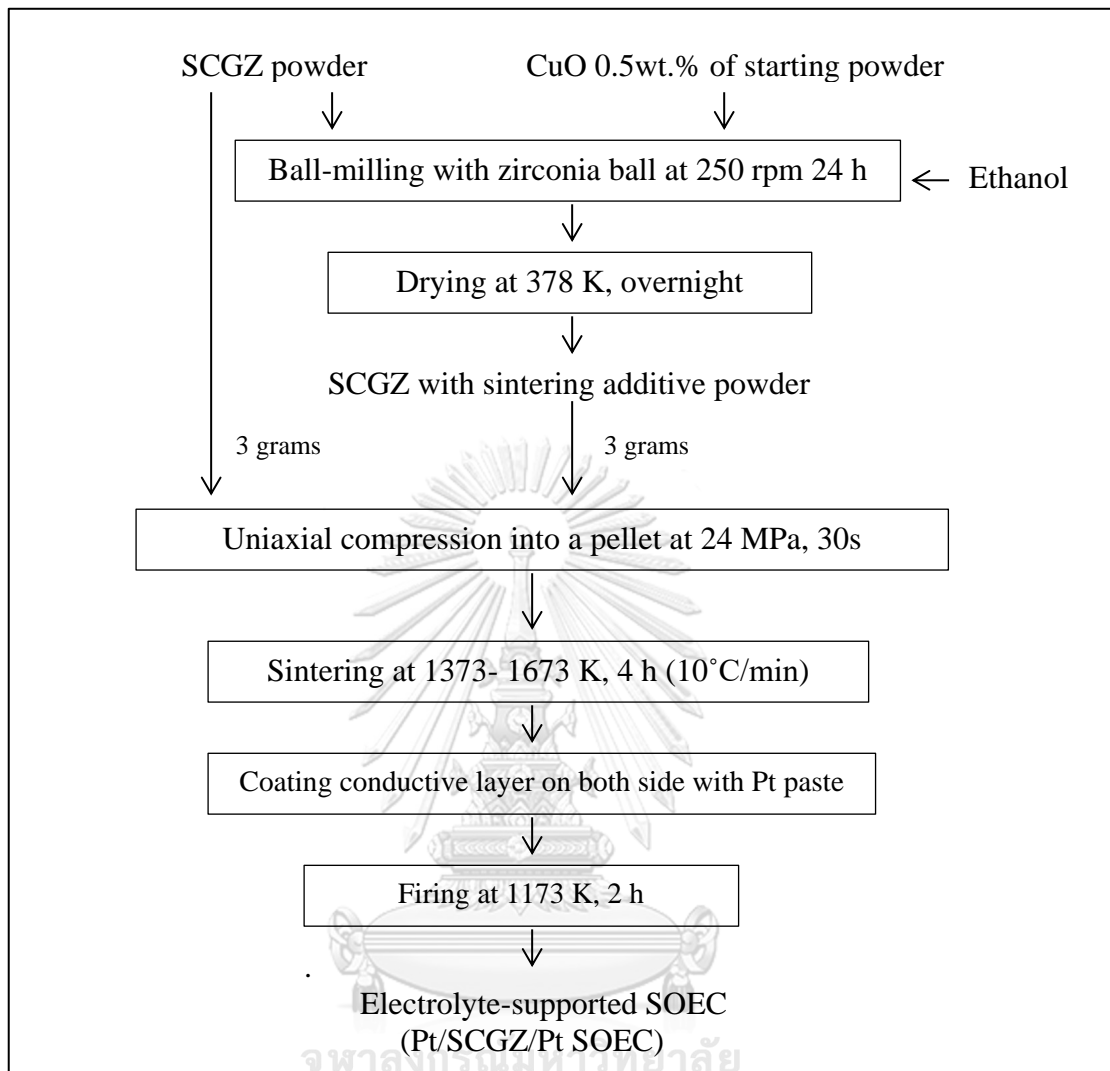


Figure 31 The fabrication procedure of electrolyte-supported SOEC

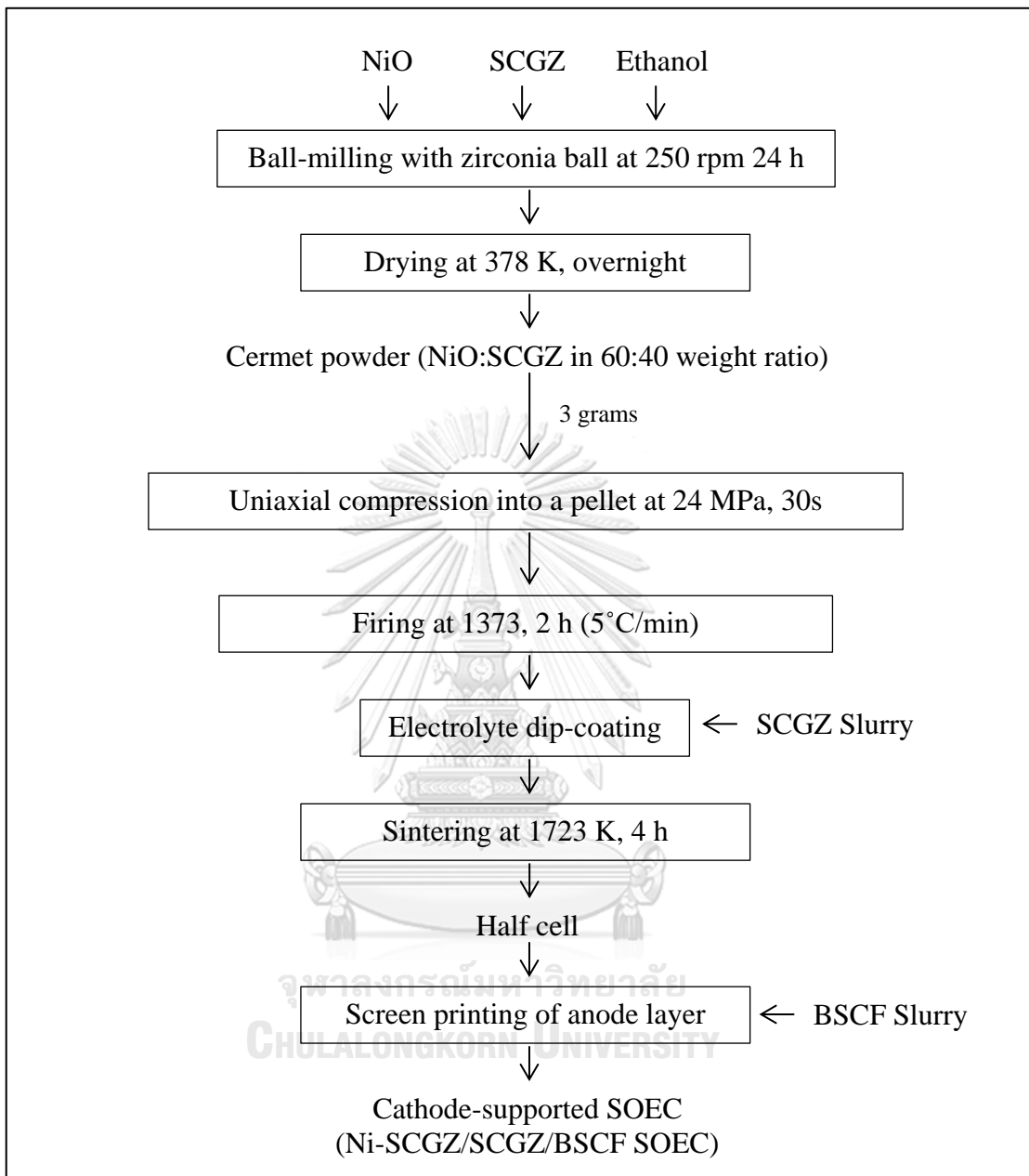


Figure 32 The fabrication procedure of cathode-supported SOEC

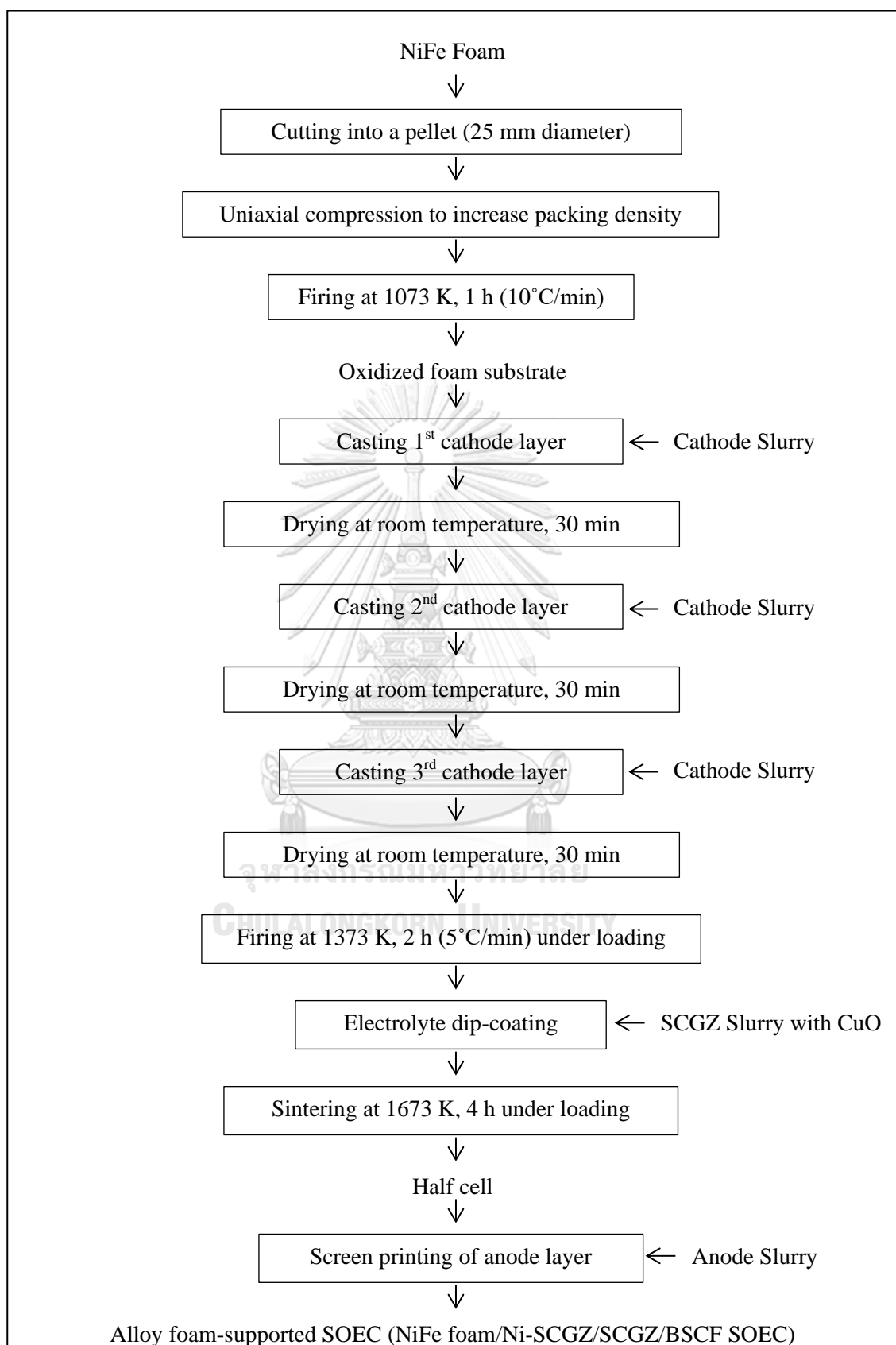


Figure 33 The fabrication procedure of Alloy foam-supported SOEC

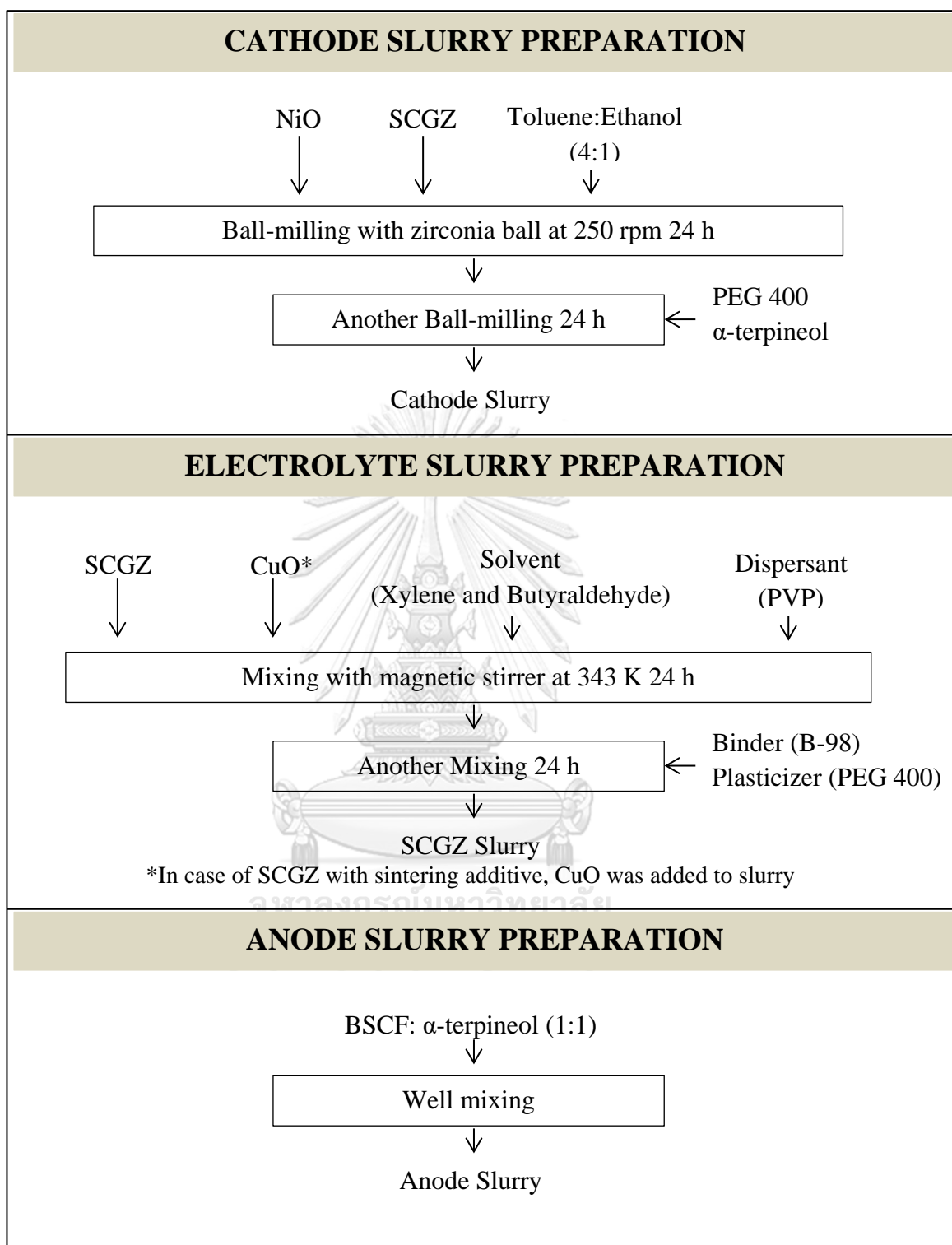


Figure 34 The preparation procedure of electrode slurries

CHAPTER IV

RESULTS AND DISCUSSION

4.1 Effect of CuO as sintering additive in different sintering temperature on the electrolyte densification

4.1.1 Densification of the electrolyte-supported SOEC

SEM images of SCGZ electrolyte with and without 0.5 wt.% CuO sintered at varied temperature from 1423 K to 1673 K are presented in Fig. 35 and 36, respectively. The microstructure images reveal that the SCGZ without the sintering additive could not be densified although high sintering temperature was used. Porosity were observed all over the SCGZ without the sintering additive. Grain boundary was observed from 1623 K but the grain size was rather small. The porosity decreased when the sintering temperature was increased. However, the relative density of the SCGZ without the sintering additive was only <90%, although high sintering temperature was increased up to 1673 K. On the other hand, densification and larger grain size were observed in the sample with the sintering additive. The grain growth was observed when increasing sintering temperature (Table 12). The added CuO could diffuse along the grain boundary and substituted in the vacancy position of the microstructure. Myung et al. [68] investigated CuO (0.3 wt.% to 1.5 wt.%) as sintering additive in yttria-stabilized zirconia (YSZ) sintering between 1423 K to 1673 K. It was reported that 0.5 wt.% of CuO is the optimal amount providing the highest densification. Amount of optimal CuO additive at 0.5 wt.% was the same for

YSZ and SCGZ, likely because both materials are zirconia-based electrolyte. However, although having same optimal CuO amount, YSZ requires relatively higher sintering temperature (1623 K) when compared with SCGZ (1573 K) at the same sintering additive amount.

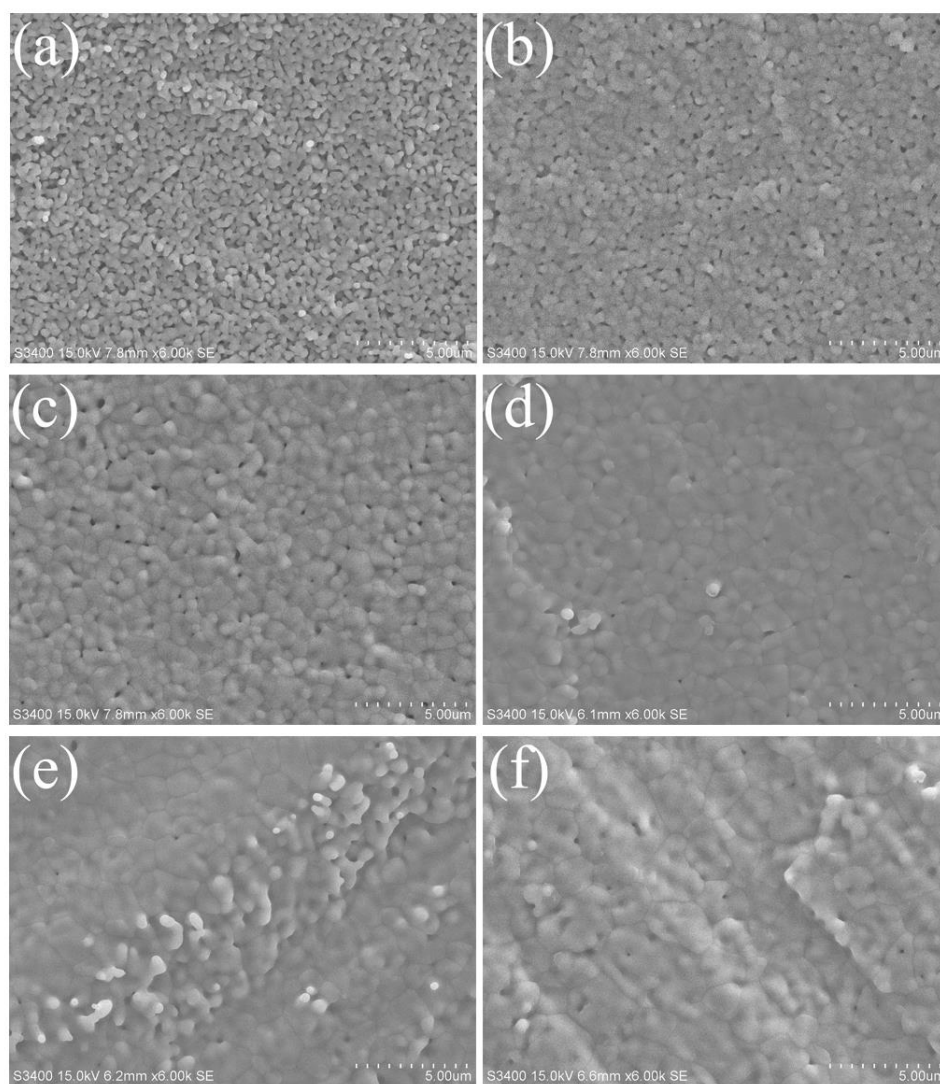


Figure 35 Scanning electron microscope (SEM) images of sintered $\text{Sc}_{0.1}\text{Ce}_{0.05}\text{Gd}_{0.05}\text{Zr}_{0.89}\text{O}_2$ (SCGZ) at (a) 1423 K, (b) 1473 K, (c) 1523 K, (d) 1573 K, (e) 1623 K, and (f) 1673 K.

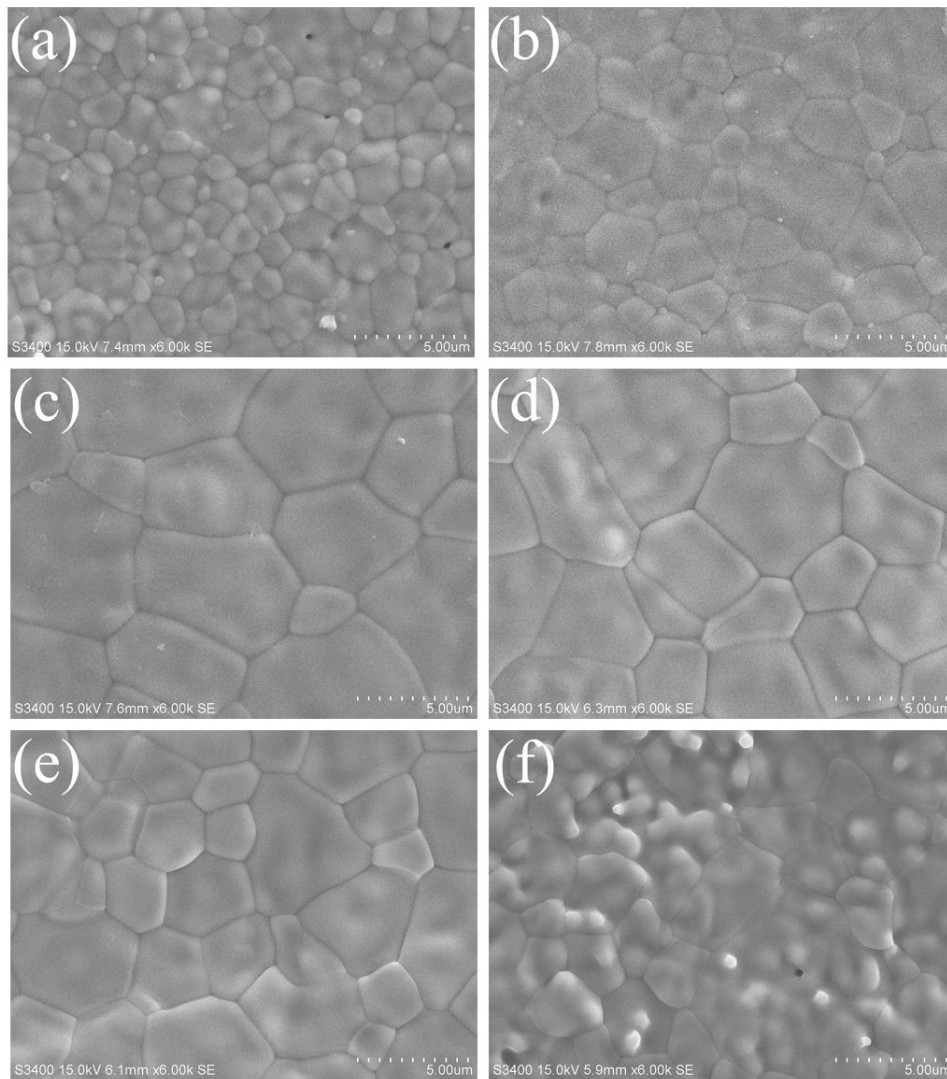


Figure 36 SEM images of sintered $\text{Sc}_{0.1}\text{Ce}_{0.05}\text{Gd}_{0.05}\text{Zr}_{0.89}\text{O}_2$ (SCGZ) with 0.5 wt.% CuO at (a) 1423 K, (b) 1473 K, (c) 1523 K, (d) 1573 K, (e) 1623 K, and (f) 1673 K.

Table 12 Average grain size of sintered $\text{Sc}_{0.1}\text{Ce}_{0.05}\text{Gd}_{0.05}\text{Zr}_{0.89}\text{O}_2$ (SCGZ) electrolyte and sintered SCGZ electrolyte with 0.5 wt.% CuO when sintering temperature was varied.

Sintering Temperature (K)	Average Grain Size (μm)	
	SCGZ	SCGZ with 0.5 wt.% CuO
1423	-	1.58
1473	-	2.66
1523	1.04	5.02
1573	1.20	5.11
1623	1.51	3.32
1673	2.28	3.77

Adding 0.5 wt.% CuO enhanced the densification of SCGZ. The relative densities of the fabricated cells are presented in Fig. 37. The SCGZ without sintering additive provided rather low relative density (<90%) at all sintering temperatures, corresponding to porosity observed in the SEM images. The SCGZ with 0.5 wt.% CuO could be densified at lower sintering temperature. Increasing sintering temperature from 1423 to 1673 K could help increase the relative density of the fabricated cell. The cell was densified at 95% relative density at 1573 K respect to other sintering temperature. It was reported that CuO exhibit relatively low melting point (around 1599 K) and can enhance sintering by pore filling during liquid phase sintering[69]. Increasing temperature above 1623 K was found to decrease the relative density of the fabricated cell, likely relating to the liquid phase sintering.

Liou et al [70] studied the effect of CuO as sintering additives on CaTiO_3 perovskite ceramics. Liquid phase sintering at grain boundary is found at sintered sample at 1723 K for 6 h and increases significantly when increasing sintering temperature to 1743 K. However, liquid phase did not occur when increasing sintering temperature up to 1773 K for 6 h, leading to less densification. Moreover, sintering soak time was increased to 8 h at 1723 K, liquid phase sintering significantly increases when compared with 6 h. A proper sintering temperature and soak time are important factors affecting the densification of the sample.

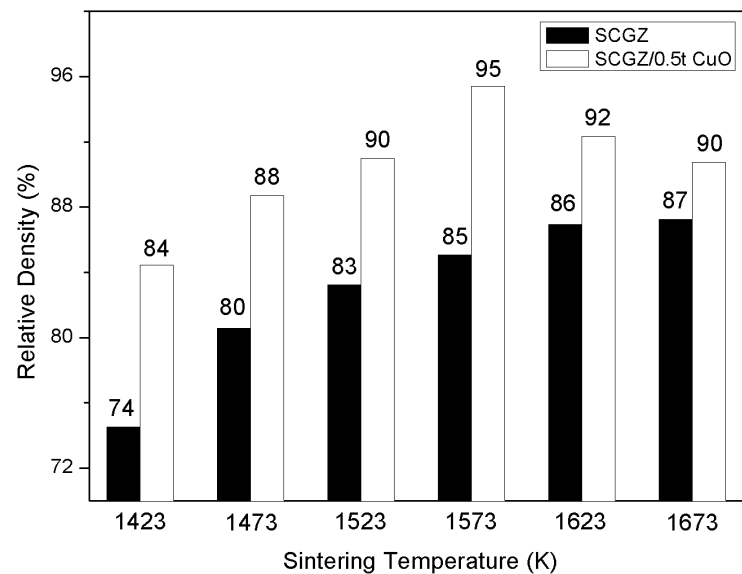


Figure 37 Relative density (%) of the SCGZ pellet and the SCGZ pellet with 0.5 wt.% CuO when the sintering temperature was varied.

4.1.2 Phase identification

XRD patterns of the SCGZ pellet sintered at 1673 K and the SCGZ with 0.5 wt.% CuO pellet sintered at 1523 K are shown in Fig. 38. The XRD patterns included main peaks at (111), (200), (220), (311), and (222) planes (COD Database ID: 1529100). Impurity phase was not detected. The XRD patterns of two samples were identical in term of the peak positions. Shifting in peaks position of the XRD patterns was not detected. This result could confirm that CuO did not form into a solid solution with SCGZ but well-mixed with SCGZ as a composite form. This results corresponded to the previous work [71]. It should be noted that CuO peaks were not detected, likely due to small amount of CuO in the sample. The average crystallite sizes were 184 nm and 202 nm for SCGZ sintered at 1673 K and SCGZ with sintering additive sintered at 1523 K, respectively, corresponding to the work that reported higher densification provided a larger grain size leading to a larger crystallite size [72].

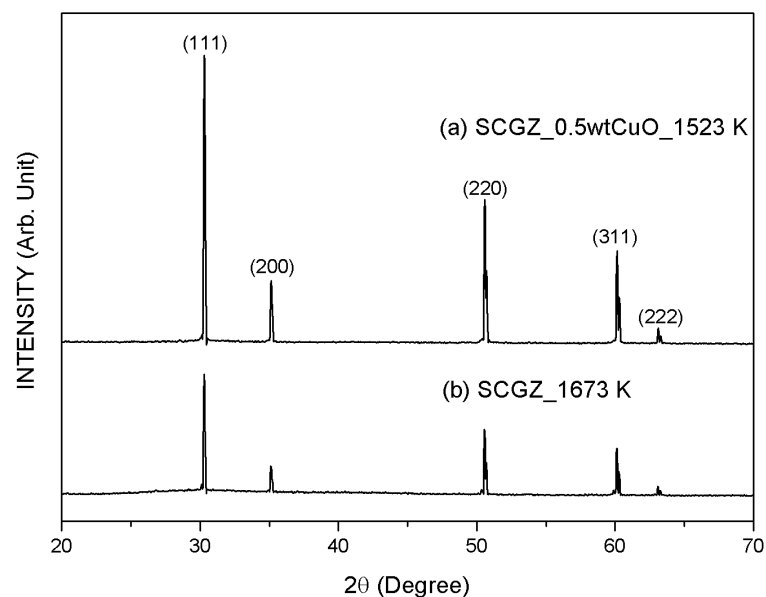


Figure 38 The X-ray diffraction patterns of (a) sintered SCGZ at 1673 K and (b) sintered SCGZ with 0.5 wt.% CuO at 1523 K.

4.1.3 Activation Energy of Conduction

The electrochemical performance of the SOEC was evaluated. Linear sweep voltammetry was from 873 K to 1173 K under a constant steam to hydrogen ratio (70:30). The I-V curves of the cells having SCGZ electrolyte without and with CuO addition are shown in Fig. 39 and 40, respectively. The conductivity and activation energy of conduction are presented in Fig. 41. It can be seen that the conductivity increased with increasing operating temperature. The activation energy of conduction (E_a) was 72.34 kJmol^{-1} and 74.93 kJmol^{-1} for SCGZ and SCGZ with CuO, respectively. In this study, adding 0.5 wt.% CuO did not significantly affect the conductivity of the electrolyte. The use of CuO as sintering additive in various ceramic electrolytes has been reported differently. It was reported that adding CuO can lead to ionic and electrical properties modification [68, 73-77]. Zhang et al [77] found that addition of 1 wt.% CuO improved the sinterability of $\text{Sm}_{0.2}\text{Ce}_{0.8}\text{O}_{1.9}$ (SDC) electrolyte. The SDC could be densified even at lower sintering temperature than 1273 K but the ionic conductivity was also decreased as a result of microstructure alteration. On the other hand, 0.5 mol% of CuO as sintering additive could provide high ionic conductivity and insignificant change in the activation energy of conduction for gadolinium-doped ceria (GDC) electrolyte [78]. In this study, 0.5 wt.% CuO was used as a potential sintering additive for SCGZ electrolyte in SOEC, decreasing the sintering temperature without any significant change in the activation energy of conduction.

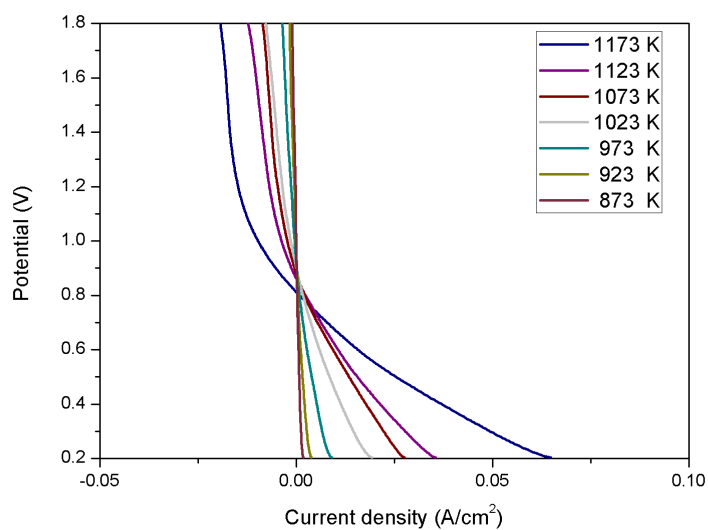


Figure 39 The I-V curves of the SCGZ electrolyte-supported SOEC conducted from 873 K to 1173 K under a constant steam to hydrogen ratio (70:30)

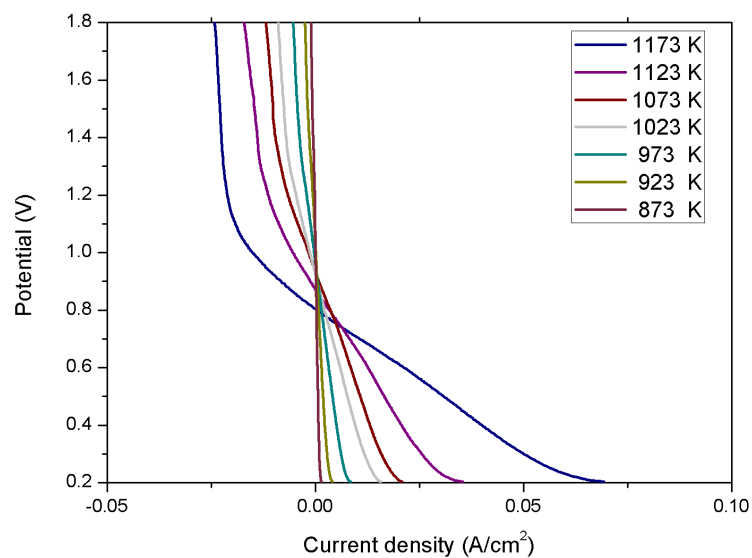


Figure 40 The I-V curves of the SCGZ with 0.5wt.% CuO electrolyte-supported SOEC conducted from 873 K to 1173 K under a constant steam to hydrogen ratio (70:30)

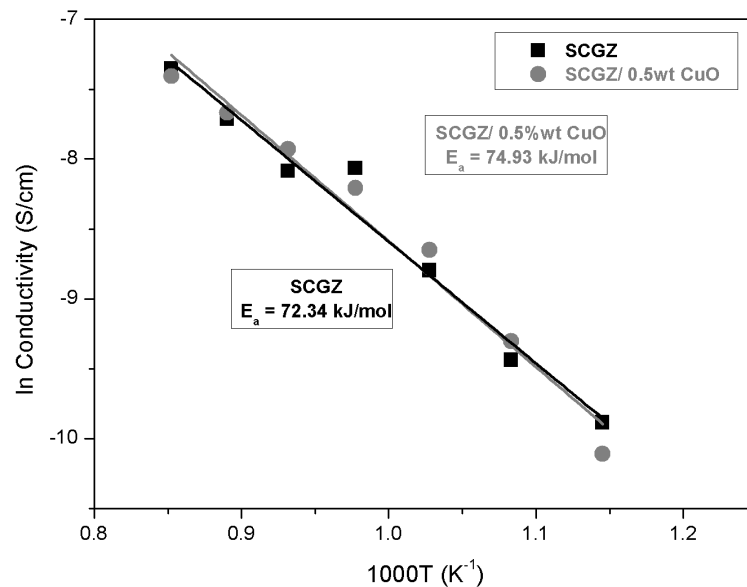
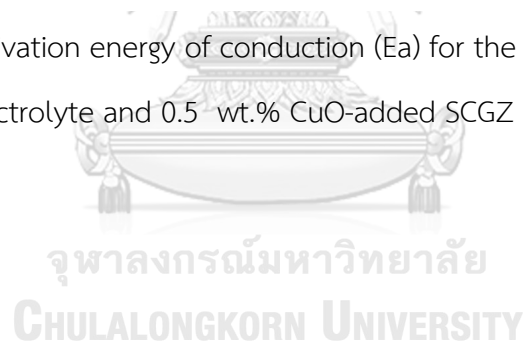


Figure 41 Activation energy of conduction (E_a) for the SOEC having SCGZ electrolyte and 0.5 wt.% CuO-added SCGZ electrolyte



4.2 Fabrication of Ni-alloy-foam-supported solid oxide electrolysis cell (SOEC)

4.2.1 Thermal behavior of the cathode and electrolyte layers

4.2.1.1 Thermal gravimetric analysis of the green layers

The decomposition of solvent and additives in the cathode and electrolyte slurry during heat treatment was one of the parameters that significantly affect the cell fabrication. This process results in a shrinkage of green layer during the firing

process. The defect formation such as cracking, peeling, and bending can occur. Therefore, thermal behavior of the green cathode and electrolyte layers can help determine suitable heat treatment conditions suppressing the defect in cell during the fabrication.

Fig. 42 and 43 present thermal behavior of the green cathode and electrolyte layers, respectively. For the green cathode layer, slurry vehicle consisted of toluene, ethanol, terpineol and polyethylene glycol (PEG 400). The binary solvent system of toluene and ethanol is commonly used in slurry composition of tape-casting technique for defect-free electrodes tape fabrication. The solvent plays critical key role of powder solubility and dispersion in slurry [79]. Homogeneity of the slurry is not only dominated by the solvent but also the dispersant. The nature of dispersant contains the stable suspension of particle with steric stabilization and hindrance. Terpineol is an effective dispersant which was reported to increase the density and flexibility of green YSZ tape [80]. PEG 400 is also used as a promising plasticizer in SOFC fabrication. PEG 400 is also used as a surfactant that provides easy casting or screen-printing of green ceramic layer [55].

As presented in Fig. 42, the mass loss of the green cathode initially occurred from 313 K to 453 K, corresponding to ethanol and toluene evaporation. The mass loss between 453 K to 673 K was corresponded to a decomposition of terpineol and PEG 400 with two exothermic heat flows observed on the DTA curve [15].

Similarly, the mass loss of green electrolyte layer was observed at the same temperature range to that of the green cathode (Fig. 43). Xylene and butyraldehyde were used as solvents in the electrolyte slurry. Polyvinylpyrrolidone (PVP), polyvinyl butyral (B-98) and PEG 400 were also used as dispersant, binder and plasticizer, respectively. This polymeric slurry was formulated in our previous work for YSZ electrolyte dip-coating [20]. A rapid mass loss was also shifted from 453-673 K in the

cathode slurry to 406-615 K in the electrolyte slurry, corresponding to decomposition of PVP, B-98 and PEG 400.

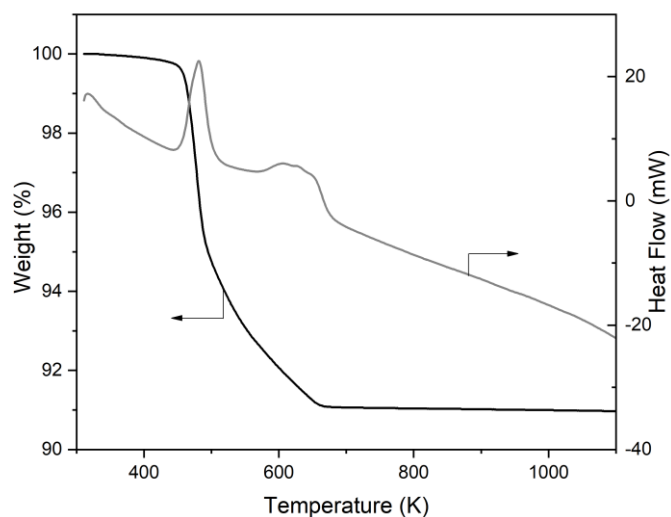


Figure 42 Thermal gravimetric (TG) curve and differential thermal analysis (DTA) curve of the green cathode layer

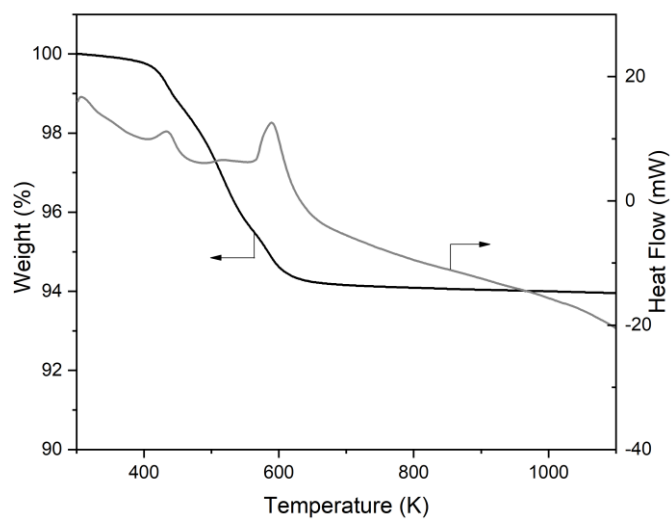


Figure 43 Thermal gravimetric (TG) curve and differential thermal analysis (DTA) curve of the green electrolyte layer

4.2.1.2 Sinterability of dip-coated electrolyte layer

In metal supported cell, the electrolyte sintering temperature should be sufficiently low in order that the metal substrate does not deform during the sintering. However, low sintering temperature resulted in a low densification of the electrolyte layer. In our previous work [81], 0.5 wt.% CuO was therefore added as a sintering additive in the SCGZ electrolyte pellet to gain a sufficient densification (>95% relative density with average grain size of 3 μm) at relatively lower sintering temperature (1523 to 1573 K) when compared with bare SCGZ electrolyte. The sintering temperature of SCGZ with CuO additive insignificantly affected the microstructure and electrochemical performance of the SOEC. In this present study, the electrolyte was deposited by dip-coating, not compressing and molding of starting powder as used in previous work. It was found that different techniques in electrolyte fabrication resulted in different electrolyte densification. For the dip coating, the electrolyte slurry contained solid particles which are suspended in the polymeric solvent. The rheology and solid packing of the green layer were influenced by various parameters such as solid content, solvent, heating rate and soak time during drying [14].

As presented in Fig. 44, although 0.5 wt.% CuO-SCGZ prepared via compressing and molding technique exhibited densified electrolyte layer after sintered at 1523-1573 K [81], the same electrolyte layer prepared via dip-coating technique did not achieve sufficient densification. Porous structure was observed. Average grain size could not be determined in this condition. The CuO content was then increased from 0.5 to 1.0 wt.% while maintain sintering temperature at 1573 K. It was found that when sintered at 1573 K, the electrolyte densification did not significantly change with increasing CuO content. Conversely, increasing the firing

temperature to 1623 and 1673 K significantly increased the electrolyte densification. The SEM images show the electrolyte average grain size at 4.03 and 4.28 μm for sintering at 1623 and 1673 K, respectively.

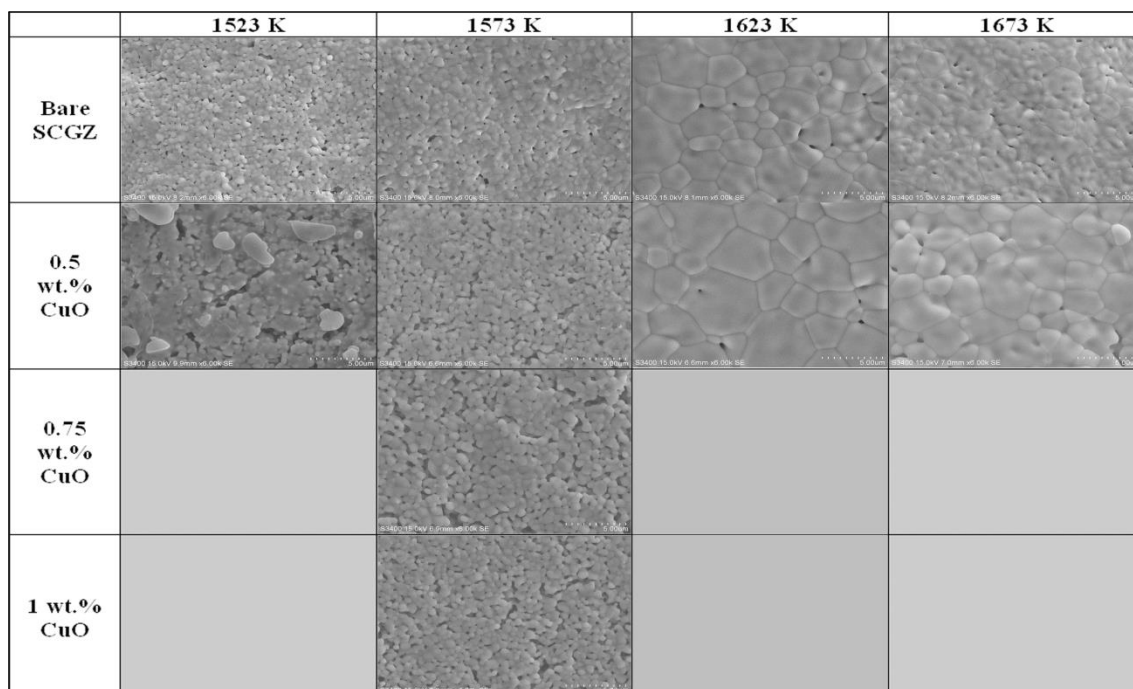


Figure 44 Sinterability of dip-coated electrolyte layer with 0.5-1 wt.% of CuO as sintering additive in SCGZ at various sintering temperature.

CHULALONGKORN UNIVERSITY

4.2.2 Degree of oxidation of the Ni-Fe-alloy foam supports

Hydrogen production from steam using SOEC was conducted in oxidizing atmosphere at the cathode side. The cell compartment at this side faced severe oxidizing conditions due to high steam content. Degree of oxidation tolerance is therefore an important parameter for material candidates as the cathode and the support. In this study, degree of oxidation of Ni-SCGZ (60:40) cermet and Ni-Fe alloy were investigated by TGA analysis as shown in Fig. 45. It was found that oxidation

tolerance of Ni-Fe alloy were higher than Ni-SCGZ cermet. The oxidation of the Ni-Fe alloy completed within 1 h. In contrast, it took Ni-SCGZ only a few minutes to reach a completed oxidation. Moreover, different Ni and Fe content provided different oxidation rate. The Ni-Fe alloy with weight ratio at 60:40 revealed a lower oxidation rate than Ni-Fe alloy with weight ratio at 50:50, corresponding to the work of Zhu J.H. et al [82] which reports that increasing Ni content decreased the oxidation rate of the Ni-Fe alloy. Li K. et al [44] also observes the redox tolerance of Ni-Fe supported in solid oxide fuel cell. Oxide scale, possibly NiFe_2O_4 , was identified on inner surface scaffold of porous Ni-Fe. This oxide scale formation prevents inward oxidation of alloy metallic inside scaffold attribute to a great oxidation resistance of the Ni-Fe support. In this study, Ni-Fe alloy foam with the ratio of Ni to Fe at 60:40 wt.% was therefore chosen as the support for the SOEC.

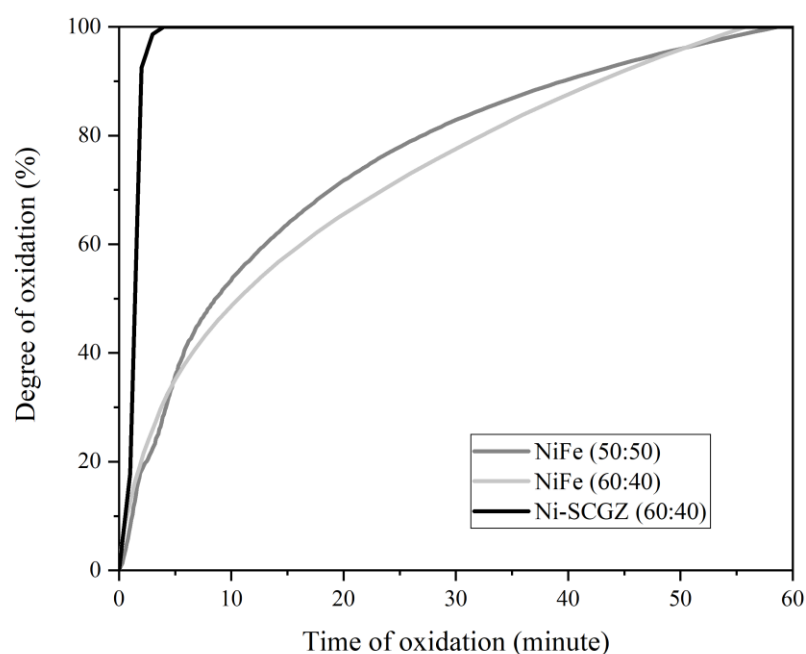


Figure 45 Degree of oxidation of candidate for the support at 1073 K under atmosphere

Not only facing severe oxidizing conditions in electrolysis operation, the support also faced the firing process in the cell fabrication. The firing process formed oxide compounds and decreased the mechanical property of the support material. Therefore, effect of various firing temperatures on Ni-Fe (60:40) foam support was also investigated. The Ni-Fe foam was fired at different temperatures (1573 K to 1673 K) in atmosphere – referred as ‘fired foam’. The fired foam was then reduced in 10 vol%H₂ at 1073 K for 12 h – referred as ‘reduced foam’. The mass changing of the fired foam was calculated by the ratio between increasing weight after firing to the initial weight of the foam. The mass changing of the reduced foam was then calculated by the ratio between increasing weight after reducing to the initial weight of the foam. As presented in Table 13, it can be seen that the Ni-Fe foams were converted to close amount of oxide compound after firing at different temperatures. The stress-strain curve of all Ni-Fe foams was presented in Fig.46. The fired foam was more brittle and less flexible than unfired foam and the reduced foam. It was likely that the oxide scale forming after firing decreased the strength of the foam. However, the mass changing after reducing process revealed the fired foams were completely reversed to the Ni-Fe alloy foam with mass changing <0.1 wt.% based on the initial weight of the unfired foam. Reducing condition after the fabrication process was considerably dominated the mechanical property and microstructure of the support.

Table 13 Mass changing of Ni-Fe-alloy foam after firing at different temperature and after reducing in 10 vol%H₂ at 1073 K, 12 h.

Firing temperature (K)	Mass changing (wt.%) (based on the initial weight of pre-fired foam)	
	After firing process	After reducing process
1573	39.68	< 0.1
1623	38.53	
1673	39.29	

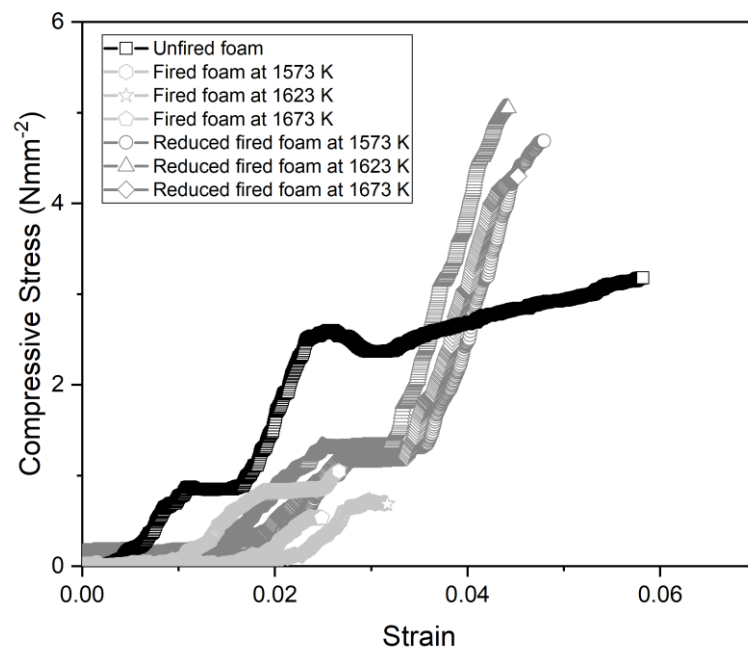


Figure 46 Stress-strain curve of Ni-Fe-alloy foam in different firing process

4.2.3 Fabrication of alloy-foam supported SOEC

4.2.3.1 Formulation of the cathode having a gradient of viscosity and thermal expansion coefficient

Microstructure of the alloy foam with high porosity was one of the key challenges in the cell fabrication. In order to produce a thin cathode layer on a highly porous foam structure by wet chemical coating technique, viscosity of the cathode slurry played a critical role. The first layer of the cathode was considered. The first cathode layer could prevent sweeping of slurry through the porous structure in the sequence coating. The first layer also acted as a bonding between the cathode functional layer and the alloy foam substrate. Therefore, the first layer of the cathode should have high viscosity as well as close thermal expansion coefficient (TEC) to the Ni-Fe alloy foam support. The first cathode layer deposition on the Ni-Fe foam was investigated by varying the solid content in the cathode slurry and the cermet composition (Ni-SCGZ). The solid content was varied from 50-80 wt.% The SEM images of the first cathode layer and the Ni-Fe foam after heat treatment are presented in Fig 47. It was found that 70-80 wt.% solid content in the cathode slurry produced a thin cathode layer attached on the foam substrate. However, 70 wt.% solid content was chosen in this study, considering an easy casting and a smooth surface. The cathode slurry with 40-50 wt.% solid content could produce smoother surface because of lower viscosity but the slurry swept through the porous structure.

The heat treatment of the fabricated cell was accompanied by a certain shrinkage of each layers due to TEC mismatching between the Ni-Fe alloy foam support and the ceramic material. To reduce the TEC mismatching, which resulted in detachment of the layers, the green cathode was divided into 3 layers with different

cermet and solid content, leading to a gradient of TEC in the cathode. High Ni content slurry (75:25 weight ratio of NiO:SCGZ) was used in the first cathode layer in order that the cathode layer could have the TEC ($13.83 \times 10^{-6} \text{ K}^{-1}$) close to that of the Ni-Fe foam ($14.16 \times 10^{-6} \text{ K}^{-1}$) in this study. However, the TEC of SCGZ electrolyte was $10.33 \times 10^{-6} \text{ K}^{-1}$. Therefore, the slurry for the second and the third cathode layer have a lower Ni and total solid content. The slurries for each cathode layer were formulated as presented in Table 14.

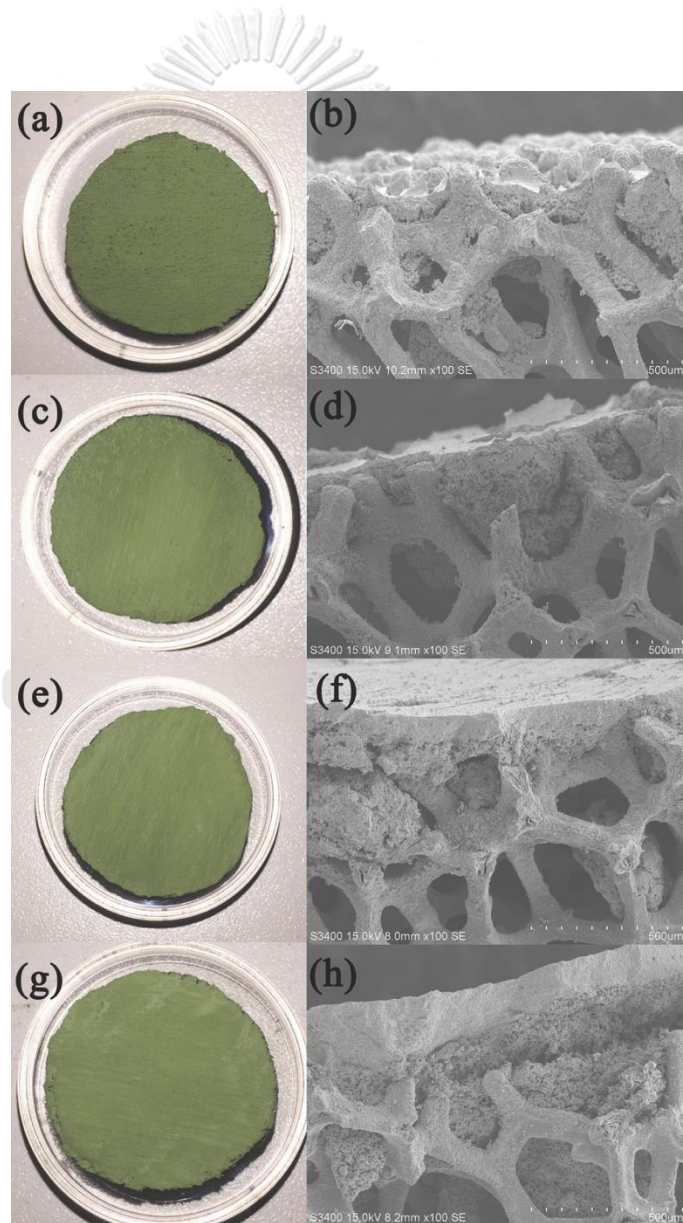


Figure 47 Ni-SCGZ cathode on the Ni-Fe-alloy foam and SEM images of cross sectional cell fabricated by varying solid content in the cathode slurry : **(a,b)** 40 wt.%; **(c,d)** 50 wt.%; **(e,f)** 70 wt.%; and, **(g,h)** 80 wt.%

Table 14 The properties of the cathode slurries

Properties	Layer				
	Ni-Fe foam	NiO-SCGZ 1	NiO-SCGZ 2	NiO-SCGZ 3	SCGZ
Solid content	-	70 wt.%	60 wt.%	50 wt.%	30wt.%
NiO:SCGZ	-	75:25	70:30	60:40	0:100
TEC ($\times 10^6 \text{ K}^{-1}$)	14.16	13.83	13.62	13.40	10.33

The rheology of the cathode slurries was evaluated as shown in Fig. 48. It was found that all slurries were non-newtonian fluid with varied viscosity along the applying shear rate. This result confirmed that Ni and total solid content affected viscosity property of the slurry. However, the test of NiO-SCGZ 1 was unsuccessfully done due to excessively viscous slurry. Three layers of the cathode were deposited. All cathode layers were co-fired at 1373K for 2 h, generating a gradient of TEC in the cathode.

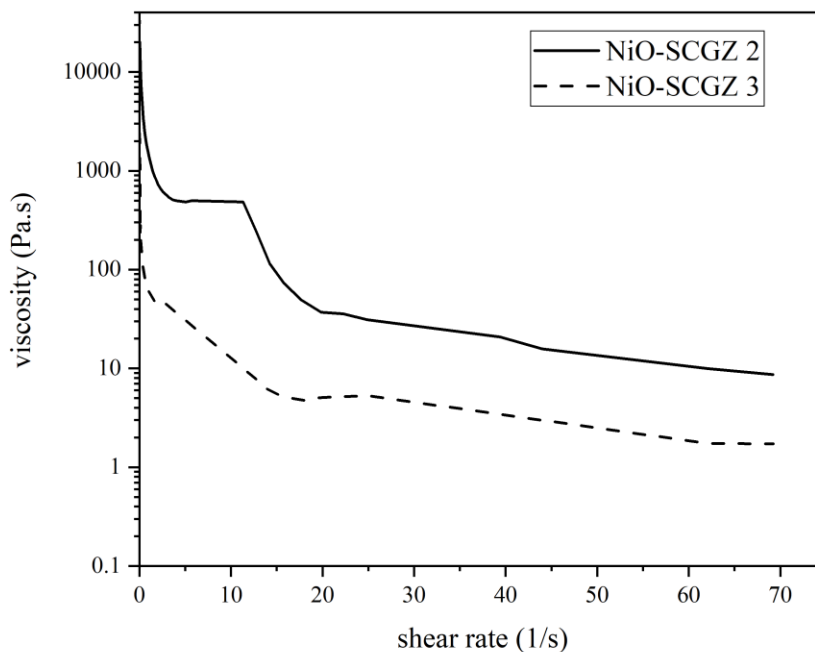


Figure 48 Viscosity-shear rate curve of the cathode slurries

4.2.3.2 Heat treatment conditions in the electrolyte sintering process

In addition to the cathode slurry composition in cathode fabrication process, heat treatment condition during the electrolyte sintering importantly influenced the cell fabrication. The SCGZ electrolyte layer was deposited by dip-coating. The effect of heating rate, compressing load, and step in firing was investigated. The images of fabricated cells with different heat treatment conditions are presented in Fig.49.

A) Effect of heating rate

The effect of heating rate during electrolyte sintering was compared at 3 K min⁻¹, 5 K min⁻¹, 10 K min⁻¹, and multi-step heating. The sintering temperature was 1623 K for 4 h. For multi-step heating, the temperature was initially ramped to 473 K with the heating rate of 1 K min⁻¹. After that, the temperature was ramped further to 673 K with the heating rate of 0.5 K min⁻¹ and 1623 K with the heating rate of 3 K

min^{-1} . The temperature of 1623 K was maintained for 4 h. Severe cracking was observed on the electrolyte surface and the faster heating rate dominated the crack formation, corresponding to the work of Jin et al [15]. The cracking was suppressed by reducing heating rate during the electrolyte sintering process. However, minor cracking was still observed on the surface. As reported earlier, the TGA of the green electrolyte layer (Fig. 43) showed significant mass loss between 353 K to 673 K due to the decomposition of the solvents and the additives in the firing process. It was likely that a rapid heating rate affected the evaporation of large amount of the organic compounds, causing a cracking network on the sintered electrolyte. Therefore, the multi-step heating rate was applied. Initially, heating of 1 K min^{-1} (ramping from room temperature to 473K) was used for solvent evaporation. After that the slower heating rate at 0.5 K min^{-1} (473K to 673K) was applied for the decomposition of additives and prevention of layer shrinkage due to a rapid mass loss. Finally, heating rate at 3 K min^{-1} (673K to 1623K) was used ramping to the electrolyte sintering temperature. In this stage, mass loss was nearly zero and additives were completely decomposition. No cracking on the electrolyte surface was observed with multi-step heating rate. However, cell bending was observed on the sintered body because of internal stress during shrinkage and expansion of each compartment at high temperature.

B) Effect of compressive loading

To produce flatness in the sintered cell without cracking, the sintered cell was fabricated by applying a compressive loading at 0.5 kg cm^{-2} on the cell surface and using the multi-step heating rate. The cell was successfully fabricated without bending as presented in Fig. 49. Compressive loading provided the excessive force to overcome internal stress distribution generated from shrinkage and expansion of the

materials. However, the amount of loading should be optimized to prevent the damage from loading. Increasing compressive loading increased the deformation rate of the cell body [83].

C) Effect of firing step

In this study, the Ni-Fe-alloy foam supported SOEC was successfully fabricated using the multi-steam heating rate and the compressive loading during the electrolyte sintering. The multi-steps heating rate for electrolyte sintering were applied after the cathode layer was initially fabricated. This process was referred as 'two-step firing' where gradient cathode layers deposited on the foam support were fired before sintering the electrolyte layer. In this study, co-firing of the electrolyte, the gradient cathode and the foam support was also investigated. As presented in Fig. 8, co-firing of all layers generated a severe defect. The gradient cathode layers were designed to suppress the effect of TEC mismatching between the support and the electrolyte. However, during co-firing, the electrolyte layer shrunk and peeled off the cathode surface and severe cracking was observed. Internal stress during the co-firing process might be excessively higher than the two steps firing. Myung et al. [53] suggested that both the mismatch of TEC and shrinkage for different material dominated the delamination of electrode layers during co-firing process. The shrinkage of each layer with multi-steps heating rate should be further investigated to fulfill the fabrication of the alloy-foam supported SOEC under co-firing condition.

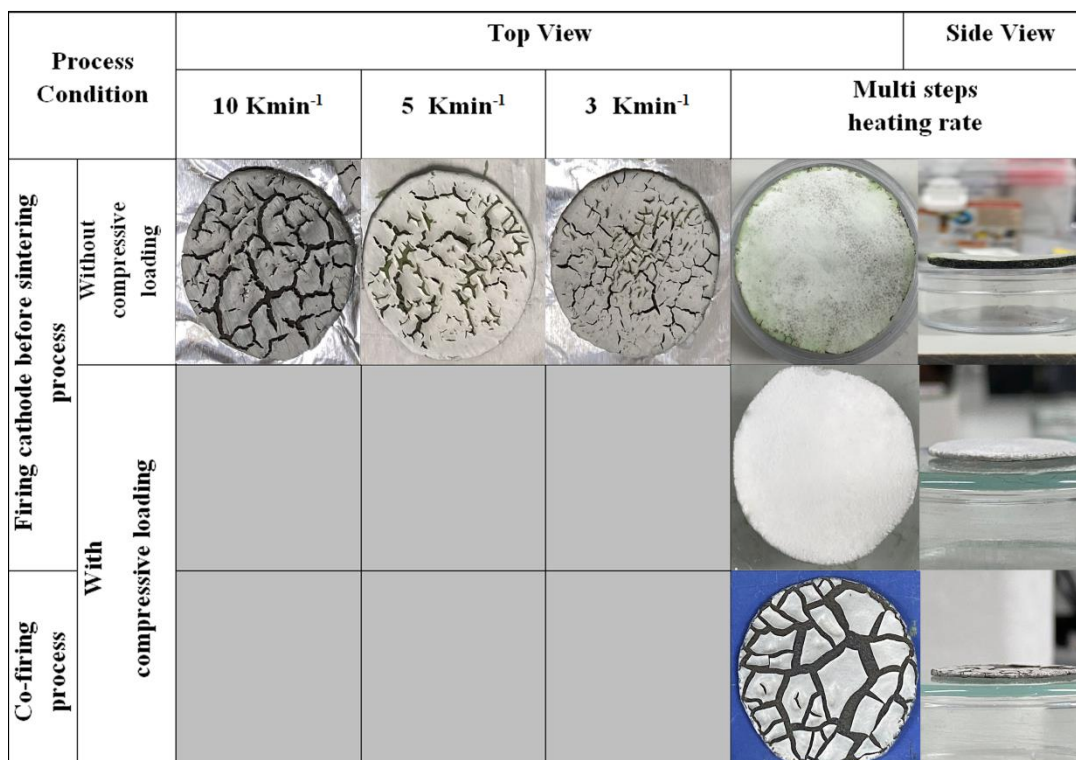


Figure 49 Images of sintered cells with different heat treatment conditions

4.2.4 Microstructure of alloy-foam-supported SOEC

The TEC in cathode was adjusted using varied NiO content in NiO-SCGZ cermet as well as total solid content in the cathode slurry. The suitable heat treatment condition was applied. Fig. 50 shows the cell during fabrication process while Fig. 51 shows microstructure of the fabricated cell. The SEM images revealed well attachment of all layers (electrolyte, electrodes and substrate). The average thickness of cathode and electrolyte were 150 and 25 μm , respectively. The cathode thickness was $\sim 100\text{-}200 \mu\text{m}$. The detachment between the Ni-Fe-alloy foam and the Ni-SCGZ cathode was eliminated by the TEC gradient in the cathode layers. The electrolyte was sufficiently dense with average grain size at 4.03 μm . The

interface between the electrolyte and the electrode layers also displayed good adhesion.

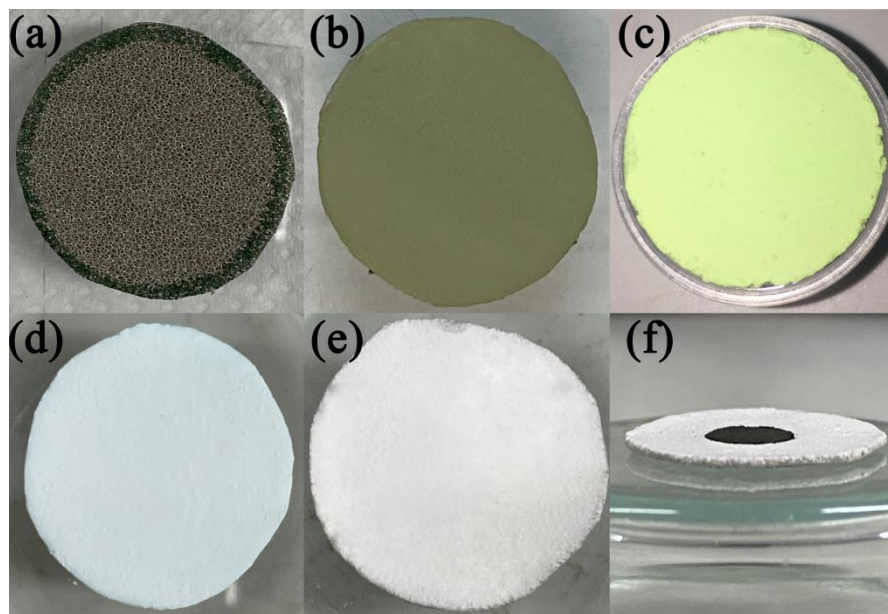


Figure 50 The Ni-Fe-alloy-foam supported Ni-SCGZ/SCGZ/BSCF SOEC : **(a)** the Ni-Fe alloy foam; **(b)** deposition of the cathode layers; **(c)** sintered Ni-SCGZ cathode; **(d)** deposition of the SCGZ electrolyte; **(e)** sintered electrolyte; and, **(f)** deposition of anode

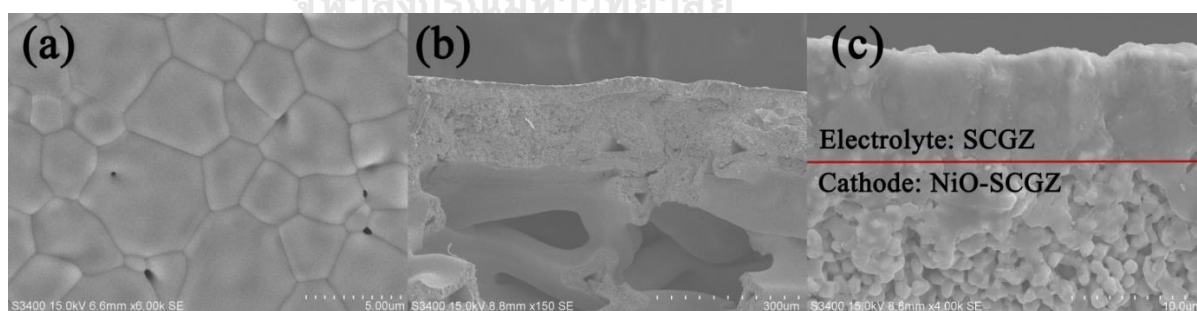


Figure 51 SEM image of Ni-Fe-alloy-foam supported-SOEC before electrochemical performance measurement; **(a)** SCGZ with 0.5 wt.% CuO additive, **(b)** cross sectional image of Ni-Fe-foam supported Ni-SCGZ/SCGZ SOEC and **(c)** interface between SCGZ electrolyte and Ni-SCGZ cathode layer

4.3 Electrochemical performance of Ni alloy-foam-supported solid oxide electrolysis cell (SOEC)

4.3.1 I-V curve and EIS measurement

The I-V curve and EIS characteristic of Ni-Fe-alloy-foam supported SOEC at temperature ranging from 873 to 1173 K with various steam to hydrogen ratio was shown in Fig. 52. The EIS characteristic was fitted into an equivalent circuit of $R_{Ohm}(R_{HF}C_{HF})(R_{LF}C_{LF})$. High frequency (HF) and low frequency (LF) resistance were represented by the first and the second arc, respectively. R_{Ohm} was the ohmic resistance of the cell and the support. The high frequency resistance (R_{HF}) generally refers to the charge transfer process and the electrochemical polarization within electrodes. The low frequency resistance (R_{LF}) refers to the mass transport resistance in both electrodes.

For the I-V curve, the open-circuit voltage of all tests was ~ 0.8 V. Increasing temperature enhanced the current density consumption in the electrolytic mode as presented in Fig. 52(a). The current density at 1.1 V increased from 0.16 to 2.19 as increasing temperature from 873 to 1173 K. The effect of steam content was investigated. As presented in Fig. 52(b), at low current density (< 1.1 V), increasing steam content insignificantly affected the electrochemical performance of the cell, corresponding to our previous work with the cathode supported cell [20]. However, at higher current density, different electrochemical performance with different steam content was seen. As presented in Fig. 52 (b) and (c), 70vol% steam content exhibited lowest cell resistance. The parameters extracted from the Nyquist plot of the Ni-Fe-alloy-foam supported SOEC with different steam content in electrolytic mode (1.1 V) were listed in Table 15. In Fig. 52(c), it was clearly seen that the steam

content in feed affected the mass diffusion process, consistent with increasing R_{LF} in the Nyquist's plot.

Table 15 The parameters extracted from the Nyquist plot of Ni-Fe-alloy-foam supported SOEC with different steam content in electrolytic mode at 1073 K

Steam content	60%vol H ₂ O	70%vol H ₂ O	80%vol H ₂ O
Parameters			
R_{Ohm} (Ωcm^2)	0.132	0.132	0.135
R_{HF} (Ωcm^2)	0.086	0.081	0.083
R_{LF} (Ωcm^2)	0.126	0.111	0.114
Total Resistance (Ωcm^2)	0.344	0.324	0.332

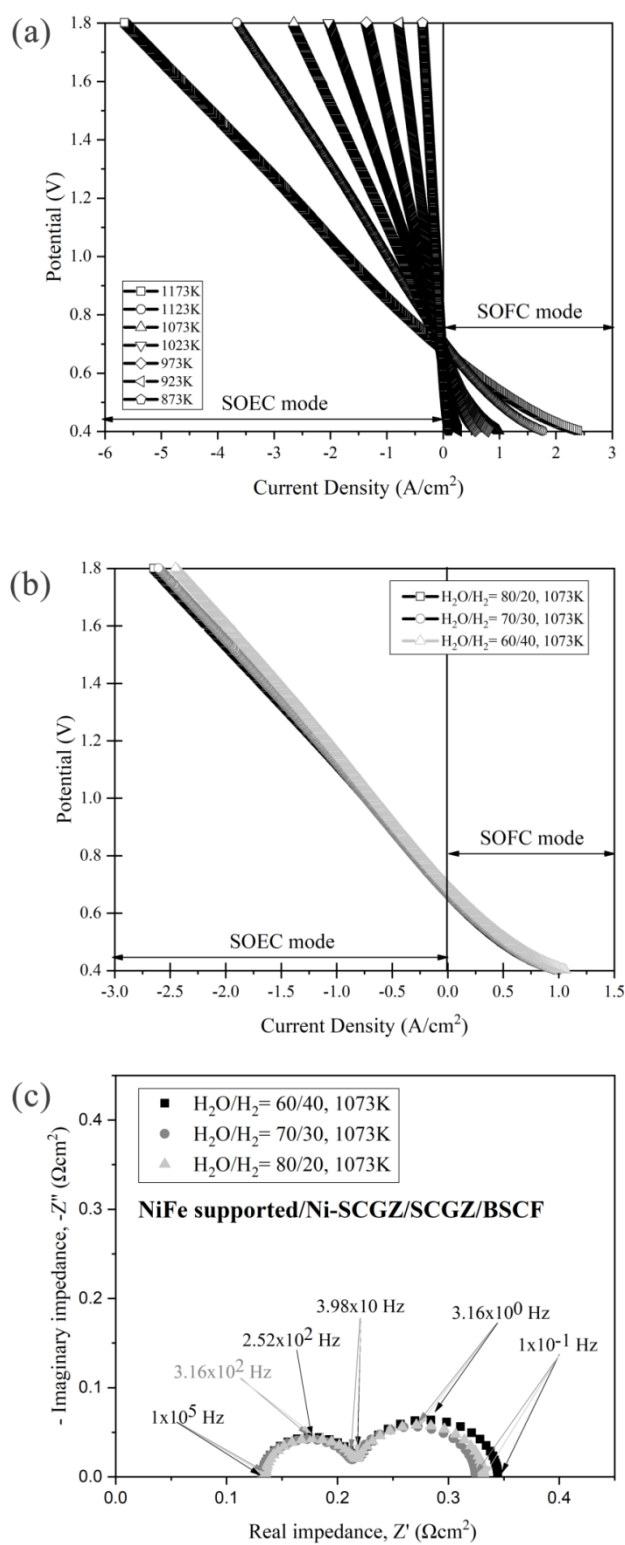


Figure 52 I-V curves of of Ni-Fe-alloy-foam supported SOEC; (a) with $H_2O:H_2 = 70:30$ at various operating temperature, (b) at 1073 K with various

H₂O:H₂ content and (c) Nyquist plot of Ni-Fe-alloy-foam supported SOEC with different steam content in feeding gas under electrolytic mode (1.1V)

4.3.2 Comparison of the electrochemical performance between the Ni-Fe-alloy-foam-support and the cathode-support SOEC

A comparison of the electrochemical performance between the Ni-Fe-alloy foam supported SOEC and a cathode-supported SOEC was investigated. Figs. 53 and 54 show the I-V curves and the Nyquist's plot of both cells, respectively. It can be seen that the alloy-foam supported cell showed much higher electrochemical performance than the cathode-support in both electrolytic and galvanic modes. It should be noted that the total thickness of the alloy-foam supported cell was ~1.2 mm (1 mm of the alloy foam; 150 μm of the cathode; 20 μm of the electrolyte; and, 30 μm of the anode, respectively) while it was 2 mm for the cathode-supported cell. The thickness of the cathode-supported cell has to be much larger than the alloy-foam-supported cell in order to withstand approximately the same pressing load of 3 Nmm⁻²). The Ni-Fe-alloy-foam-supported SOEC exhibited the current density of 0.95 Acm⁻² at potential of 1.1 V and H₂O:H₂ of 70:30 at 1073 K. This was ~1.5 times greater than the cathode-supported cell in electrolytic mode. The hydrogen production rate was 4.95x10⁻⁶ and 3x10⁻⁶ mol s⁻¹ for the the Ni-Fe-alloy-foam-supported SOEC and cathode-supported SOEC, respectively.

The parameters extracted from the Nyquist plots of both cells were listed in Table 16. Total resistance of the foam-supported SOEC was significantly lower than the cathode-supported cell, especially the ohmic resistance. However, the durability of the alloy-foam-supported cell was rather poor as shown in Fig. 55. The potential increased to 1.5 V within 4 h of operation (potential degradation rate of ~0.08 Vh⁻¹).

SEM images of the tested cell were shown in Fig. 56. Delamination of BSCF anode was clearly seen (Fig. 56(d)). It was likely that high current density accelerate the delamination of the BSCF anode. Therefore, the alloy-foam supported cell degrades faster than the cathode-supported cell which operated at a lower current density. High partial pressure of oxygen built up at the interface between the anode and the electrolyte, introducing the anode delamination. It was reported that the SOEC operated in high current density ($0.5\text{-}1\text{ Acm}^{-2}$) accelerates the cell degradation [84]. Moreover, it was reported that a limitation of conventional SOEC under long-term operation is often the oxidization of the cathode layer, decreasing three-phase boundaries (TPBs) and poor durability. Thicker cathode layer in the cathode supported SOEC can slower the cathode degradation rate when compared to the alloy-foam supported SOEC. Teng et al. [85] reported poor durability (0.07 Vh^{-1}) of Ni-YSZ/YSZ/SDC/SSCN electrolyte-supported SOEC under steam to hydrogen of 50:50 at 1073 K with current consumption 0.5 Acm^{-2} . To enhance the durability of Ni-Fe-alloy-foam supported SOEC, the optimized cell configuration such cathode thickness as well as operating condition such as steam to hydrogen ratio in feed and current consumption are required for further investigation. Alternatively, cathode materials are also needed to be an oxidation tolerance material.

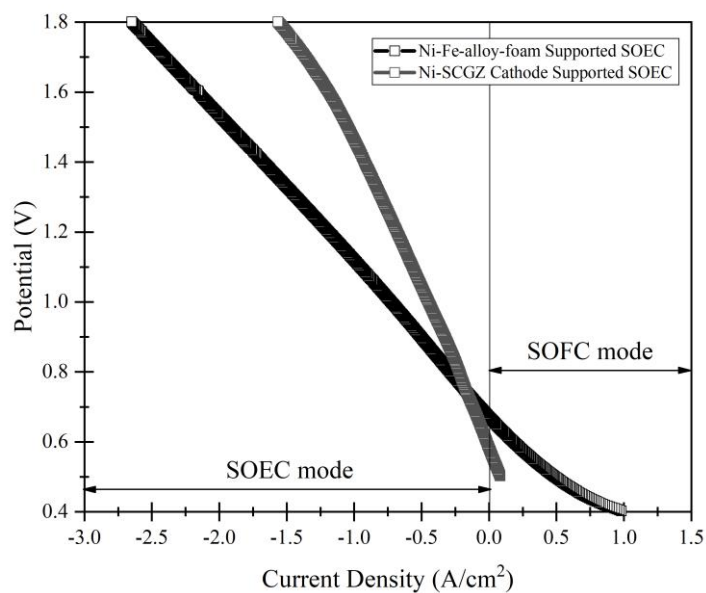


Figure 53 I-V curves of Ni-Fe-alloy-foam supported SOEC and Ni-SCGZ cathode-supported SOEC with H₂O:H₂ = 70:30 at 1073 K



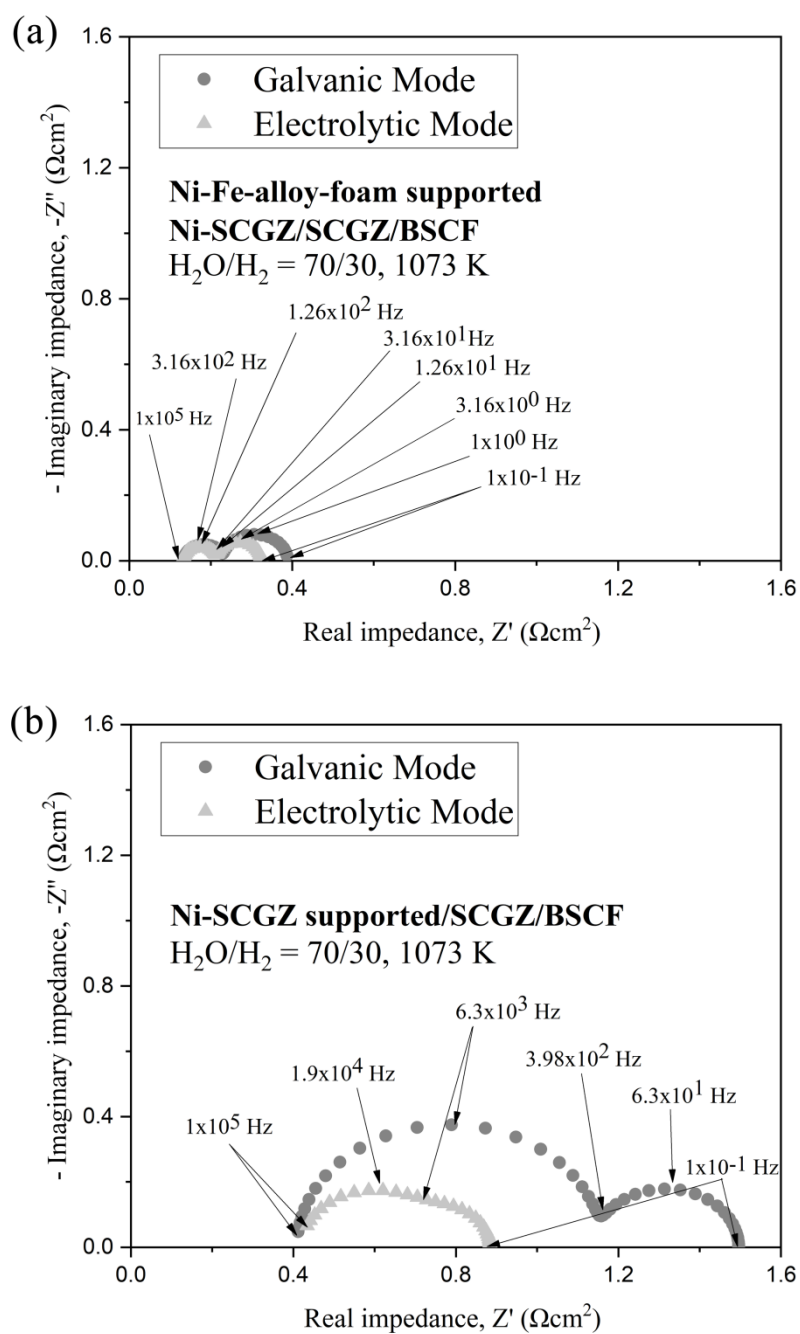


Figure 54 The Nyquist plot at $H_2O:H_2 = 70:30$ and 1073 K: (a) Ni-Fe-alloy-foam supported SOEC and (b) Ni-SCGZ cathode supported SOEC

Table 16 The parameters extracted from the Nyquist plot of Ni-Fe-alloy-foam supported SOEC and Ni-SCGZ cathode supported SOEC with H₂O:H₂ = 70:30 at 1073 K

Parameters	Ni-Fe-foam supported SOEC		Cathode supported SOEC [20]	
	Electrolytic	Galvanic	Electrolytic	Galvanic
	R _{Ohm} (Ωcm^2)	0.132	0.134	0.434
R _{HF} (Ωcm^2)	0.090	0.087	0.294	0.736
R _{LF} (Ωcm^2)	0.163	0.103	0.157	0.339
Total Resistance (Ωcm^2)	0.385	0.324	0.451	1.075

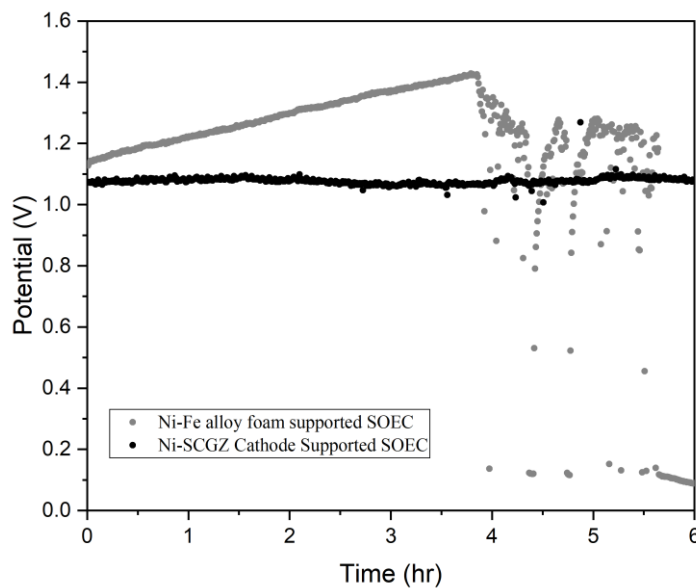


Figure 55 Durability test of Ni-Fe-alloy-foam supported SOEC and Ni-SCGZ cathode supported SOEC operated at 0.9 and 0.6 Acm⁻², respectively with H₂O:H₂ = 70:30 at 1073 K, 10 h.

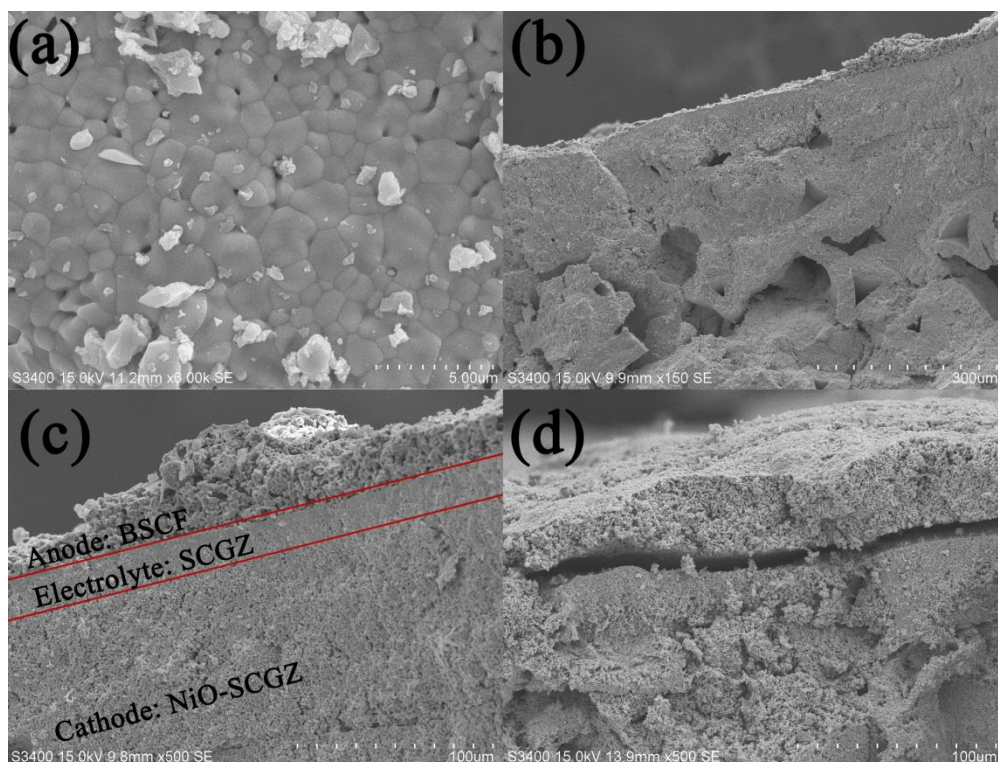


Figure 56 SEM images of Ni-Fe-alloy foam supported SOEC after durability test operated at 0.9 cm^{-2} with $\text{H}_2\text{O}:\text{H}_2 = 70:30$ at 1073 K and 10 h
(a) SCGZ with 0.5 wt.% CuO additive; **(b)** cross sectional image of Ni-Fe-foam supported Ni-SCGZ/SCGZ/BSCF; **(c)** interface between BSCF anode, SCGZ electrolyte and Ni-SCGZ cathode layer; and, **(d)** interface between BSCF anode and SCGZ electrolyte.



Figure 57 Image of Ni-Fe-alloy-foam supported SOEC after durability test operated at 0.9 and 0.3 Acm^{-2} with $\text{H}_2\text{O}:\text{H}_2 = 70:30$ at 1073 K, 10 h



CHAPTER V

CONCLUSIONS

5.1 Conclusion

0.5 wt.% CuO was employed as a sintering additive for SCGZ electrolyte in SOEC. Phase formation, microstructure, relative density, and electrochemical performance of electrolyte-supported SOEC were investigated. Adding 0.5 wt.% CuO helped increasing the sinterability of the electrolyte which could achieve 95% relative density with a large grain size at 1573 K. The average grain size was measured at 5.11 μm when sintering temperature was 1573 K for SCGZ with CuO. Phase transformation and impurity was not detected in the electrolyte after adding CuO. Neither peak shifting nor impurity peak were detected in the XRD patterns. Without CuO addition, the SCGZ could not be densified although sintering temperature was increased up to 1673 K. Adding CuO into SCGZ insignificantly affected the electrochemical performance of the cell. The activation energy of conduction (E_a) of the SCGZ with and without CuO was 74.93 kJ mol⁻¹ and 72.34 kJ mol⁻¹, respectively.

The Ni-Fe-alloy-foam (porosity: 5-130 ppi) supported SOEC (Ni-SCGZ/SCGZ/BSCF) was successfully fabricated using wet chemical coating technique. The Ni-SCGZ cathode was divided into three layers with a gradient of TEC, ranging from the TEC close to the Ni-Fe foam to the SCGZ electrolyte. This could help prevent the defect in the cell during electrolyte sintering process. The electrolyte was sintered using the multi-step firing. The conditions for heat treatment process during fabrication were investigated. Slow heating rate with sufficient compressive loading during sintering process was applied to prevent cracking and wrapping of a

fabricated cell. The average thickness of active functional cathode layer, electrolyte, and anode were 150, 25 and 30 μ m, respectively. Electrochemical performance of the alloy-foam-supported SOEC was investigated. The cell showed high current density of 0.95 A cm^{-2} operated under 1.1 V with $\text{H}_2\text{O}:\text{H}_2 = 70:30$ and 1073 K, corresponding to the hydrogen production rate of $4.95 \times 10^{-6} \text{ mol s}^{-1}$. However, the durability of the cell was rather low. The degradation rate was 0.08 V h^{-1} . The BSCF anode delamination was clearly seen, likely due to high current density operation, inducing high oxygen partial pressure at the anode/electrolyte interface. Thin Ni-SCGZ cathode layer also exhibited higher degradation rate due to cathode oxidation under high steam partial pressure when compared to the thicker cathode-supported cell. Optimized operating conditions are required for a suitable trade-off between high performance and durability in the alloy-foamed supported SOEC.

5.2 Recommendation

For future work, the implementation and optimization of cell structure and operation will be required to improve the cell's durability. In this study, the higher hydrogen production rate of alloy-foam supported SOEC was obtained when compared with cathode-supported SOEC. However, poor durability was likely due to operating in high current density causing the anode degradation. High oxygen build up at the anode induced delamination of the anode and the electrolyte layer. The chemical instability of the BSCF anode also caused the degradation in the material. The cathode material also needs to be higher oxidation tolerance. The suggestion for future work is divided into 2 parts: 1) the optimization of an operating conditions in electrochemical reaction and 2) evaluation of new anode materials.

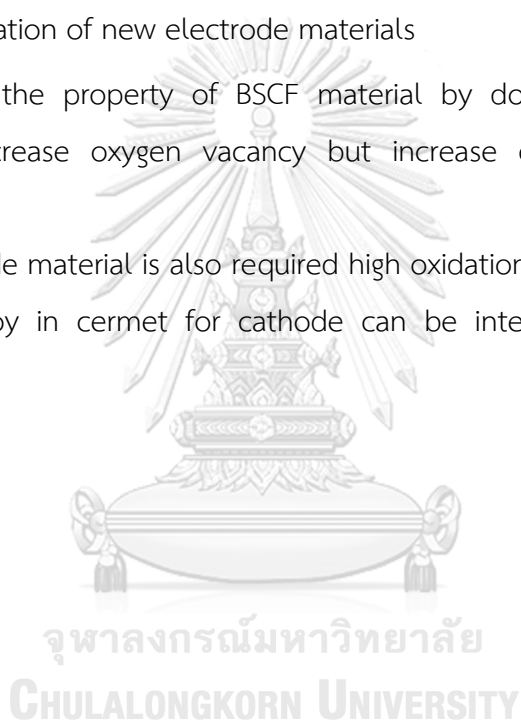
5.2.1 The optimization of an operating condition in electrochemical reaction

The optimum of current density and operating temperature should be investigated for durability improvement. The oxidation of cathode layer has been identified after electrolysis operation. Steam to hydrogen ratio at 70:30 provided a great electrochemical performance. Nevertheless, the ratio should also optimum to suppress the cathode oxidation and coarsening.

5.2.2 Evaluation of new electrode materials

Enhancing the property of BSCF material by doping with higher valence element can decrease oxygen vacancy but increase chemical stability of the material.

The cathode material is also required high oxidation tolerance properties. The use of metal alloy in cermet for cathode can be interesting topic for cathode development.



REFERENCES

- [1] Kim-Lohsoontorn P, Kim Y-M, Laosiripojana N, Bae J. Gadolinium doped ceria-impregnated nickel–yttria stabilised zirconia cathode for solid oxide electrolysis cell. *Int J Hydrogen Energy*. 2011;36:9420-7.
- [2] Laguna-Bercero MA, Skinner SJ, Kilner JA. Performance of solid oxide electrolysis cells based on scandia stabilised zirconia. *J Power Sources*. 2009;192:126-31.
- [3] Bernuy-Lopez C, Knibbe R, He Z, Mao X, Hauch A, Nielsen KA. Electrochemical characterisation of solid oxide cell electrodes for hydrogen production. *J Power Sources*. 2011;196:4396-403.
- [4] Hjalmarsson P, Sun X, Liu Y-L, Chen M. Durability of high performance Ni–yttria stabilized zirconia supported solid oxide electrolysis cells at high current density. *J Power Sources*. 2014;262:316-22.
- [5] Tao Z-T, Jiang Y-M, Lei L, Chen F. $\text{Pr}_{0.5}\text{Ba}_{0.5}\text{Co}_{0.7}\text{Fe}_{0.25}\text{Nb}_{0.05}\text{O}_{3-\delta}$ as air electrode for solid oxide steam electrolysis cells. *Int J Hydrogen Energy*. 2019;44:23539-46.
- [6] Zhou J, Ma Z, Zhang L, Liu C, Pu J, Chen X, et al. Study of CO_2 and H_2O direct co-electrolysis in an electrolyte-supported solid oxide electrolysis cell by aqueous tape casting technique. *Int J Hydrogen Energy*. 2019;44:28939-46.
- [7] Tucker MC. Progress in metal-supported solid oxide fuel cells: A review. *J Power Sources*. 2010;195:4570-82.
- [8] Jo KH, Kim JH, Kim KM, Lee I-S, Kim S-J. Development of a new cost effective Fe–Cr ferritic stainless steel for SOFC interconnect. *Int J Hydrogen Energy*. 2015;40:9523-9.
- [9] Brandner M, Bram M, Froitzheim J, Buchkremer HP, Stöver D. Electrically Conductive Diffusion barrier layers for Metal-Supported SOFC. *Solid State Ionics*. 2008;179:1501-4.
- [10] Dayaghi AM, Kim KJ, Kim S, Park J, Kim SJ, Park BH, et al. Stainless steel-supported solid oxide fuel cell with $\text{La}_{0.2}\text{Sr}_{0.8}\text{Ti}_{0.9}\text{Ni}_{0.1}\text{O}_{3-\delta}$ /yttria-stabilized zirconia composite anode. *J Power Sources*. 2016;324:288-93.
- [11] Kim KJ, Kim SJ, Choi GM. $\text{Y}_{0.08}\text{Sr}_{0.88}\text{TiO}_3\text{–CeO}_2$ composite as a diffusion barrier layer for stainless-steel supported solid oxide fuel cell. *J Power Sources*. 2016;307:385-90.
- [12] Venkatachalam V, Molin S, Chen M, Smirnov I, Larsson P-O, Vang Hendriksen P, et

al. Optimization of ferritic steel porous supports for protonic fuel cells working at 600°C 2014.

- [13] Kim KH, Park YM, Kim H. Fabrication and evaluation of the thin NiFe supported solid oxide fuel cell by co-firing method. *Energy*. 2010;35:5385-90.
- [14] Lee S, Lee K, Jang Y-h, Bae J. Fabrication of solid oxide fuel cells (SOFCs) by solvent-controlled co-tape casting technique. *Int J Hydrogen Energy*. 2017;42:1648-60.
- [15] Jin C, Mao Y, Zhang N, Sun K. Fabrication and characterization of Ni-SSZ gradient anodes/SSZ electrolyte for anode-supported SOFCs by tape casting and co-sintering technique. *Int J Hydrogen Energy*. 2015;40:8433-41.
- [16] Dogdibegovic E, Wang R, Lau GY, Tucker MC. High performance metal-supported solid oxide fuel cells with infiltrated electrodes. *J Power Sources*. 2019;410-411:91-8.
- [17] Esposito L, Boccaccini DN, Pucillo GP, Frandsen HL. Secondary creep of porous metal supports for solid oxide fuel cells by a CDM approach. *Materials Science and Engineering: A*. 2017;691:155-61.
- [18] Tan WC, Saw LH, Thiam HS, Xuan J, Cai Z, Yew MC. Overview of porous media/metal foam application in fuel cells and solar power systems. *Renewable and Sustainable Energy Reviews*. 2018;96:181-97.
- [19] Gondolini A, Mercadelli E, Sangiorgi A, Sanson A. Integration of Ni-GDC layer on a NiCrAl metal foam for SOFC application. *J Eur Ceram Soc*. 2017;37:1023-30.
- [20] Temluxame P, Puengjinda P, Peng-ont S, Ngampuengpis W, Sirimungkalakul N, Jiwaturuk T, et al. Comparison of ceria and zirconia based electrolytes for solid oxide electrolysis cells. *Int J Hydrogen Energy*. 2020.
- [21] Hydrogen. National Center for Biotechnology Information. PubChem Database.
- [22] The Future of Hydrogen. In: (2019) I, editor. Paris: IEA; 2019.
- [23] Barelli L, Bidini G, Gallorini F, Servili S. Hydrogen production through sorption-enhanced steam methane reforming and membrane technology: A review. *Energy*. 2008;33:554-70.
- [24] Efstathiou CMKaAM. Hydrogen Production Technologies: Current State and Future Developments. *Power Options for the Eastern Mediterranean Region*. Limassol, Cyprus: Hindawi Publishing Corporation; 2013. p. 9.
- [25] Sapountzi FM, Gracia JM, Weststrate CJ, Fredriksson HOA, Niemantsverdriet JW.

Electrocatalysts for the generation of hydrogen, oxygen and synthesis gas. *Prog Energy Combust Sci.* 2017;58:1-35.

[26] Colleen S. *Designing and Building Fuel Cells: McGraw-Hill Professional*; 2007.

[27] Dwivedi S. Solid oxide fuel cell: Materials for anode, cathode and electrolyte. *Int J Hydrogen Energy.* 2020.

[28] Zhang L, Wang Z, Cao Z, Zhu L, Li P, Li J, et al. High activity oxide $\text{Pr}_{0.3}\text{Sr}_{0.7}\text{Ti}_{0.3}\text{Fe}_{0.7}\text{O}_{3-\delta}$ as cathode of SOEC for direct high-temperature steam electrolysis. *Int J Hydrogen Energy.* 2017;42:12104-10.

[29] Yu J, Men HJ, Qu YM, Tian N. Performance of Ni-Fe bimetal based cathode for intermediate temperature solid oxide electrolysis cell. *Solid State Ionics.* 2020;346:115203.

[30] Lim CK, Liu Q, Zhou J, Sun Q, Chan SH. High-temperature electrolysis of synthetic seawater using solid oxide electrolyzer cells. *J Power Sources.* 2017;342:79-87.

[31] Jensen SH, Larsen PH, Mogensen M. Hydrogen and synthetic fuel production from renewable energy sources. *Int J Hydrogen Energy.* 2007;32:3253-7.

[32] Jaiswal N, Tanwar K, Suman R, Kumar D, Upadhyay S, Parkash O. A brief review on ceria based solid electrolytes for solid oxide fuel cells. *J Alloys Compd.* 2019;781:984-1005.

[33] Chan Y-H, Lai H-Y, Chen Co-K. Enhancing oxygen iron conductivity of 8YSZ electrolytes in SOFC by doping with Fe_2O_3 . *Computational Materials Science.* 2018;147:1-6.

[34] Badwal SPS, Ciacchi FT. Oxygen-ion conducting electrolyte materials for solid oxide fuel cells. *Ionics.* 2000;6:1-21.

[35] Fini D, Badwal SPS, Giddey S, Kulkarni AP, Bhattacharya S. Evaluation of Sc_2O_3 - CeO_2 - ZrO_2 electrolyte-based tubular fuel cells using activated charcoal and hydrogen fuels. *Electrochim Acta.* 2018;259:143-50.

[36] Anwar M, S.A MA, Muchtar A, Somalu MR. Influence of strontium co-doping on the structural, optical, and electrical properties of erbium-doped ceria electrolyte for intermediate temperature solid oxide fuel cells. *Ceram Int.* 2019;45:5627-36.

[37] Zhang J, Lenser C, Menzler NH, Guillon O. Comparison of solid oxide fuel cell

(SOFC) electrolyte materials for operation at 500 °C. *Solid State Ionics*. 2020;344:115138.

[38] Singh M, Singh AK. Studies on structural, morphological, and electrical properties of Ga³⁺ and Cu²⁺ co-doped ceria ceramics as solid electrolyte for IT-SOFCs. *Int J Hydrogen Energy*. 2019.

[39] Puente-Martínez DE, Díaz-Guillén JA, Montemayor SM, Díaz-Guillén JC, Burciaga-Díaz O, Bazaldúa-Medellín ME, et al. High ionic conductivity in CeO₂ SOFC solid electrolytes; effect of Dy doping on their electrical properties. *Int J Hydrogen Energy*. 2019.

[40] Kim Y-D, Yang J-Y, Lee J-I, Saqib M, Shin J-S, Shin M, et al. Stable ceria-based electrolytes for intermediate temperature-solid oxide fuel cells via hafnium oxide blocking layer. *J Alloys Compd*. 2019;779:121-8.

[41] Cheol SH, Haeng YJ, Tae LK, Lak LH, Ho BK. Effects of Partial Substitution of CeO₂ with M₂O₃ (M = Yb, Gd, Sm) on Electrical Degradation of Sc₂O₃ and CeO₂ Co-doped ZrO₂. *J Korean Ceram Soc*. 2016;53:500-5.

[42] Kim-Lohsoontorn P, Brett DJL, Laosiripojana N, Kim YM, Bae JM. Performance of solid oxide electrolysis cells based on composite La_{0.8}Sr_{0.2}MnO_{3-δ} – yttria stabilized zirconia and Ba_{0.5}Sr_{0.5}Co_{0.8}Fe_{0.2}O_{3-δ} oxygen electrodes. *Int J Hydrogen Energy*. 2010;35:3958-66.

[43] Kim Y-M, Kim-Lohsoontorn P, Baek S-W, Bae J. Electrochemical performance of unsintered Ba_{0.5}Sr_{0.5}Co_{0.8}Fe_{0.2}O_{3-δ}, La_{0.6}Sr_{0.4}Co_{0.8}Fe_{0.2}O_{3-δ}, and La_{0.8}Sr_{0.2}MnO_{3-δ} cathodes for metal-supported solid oxide fuel cells. *Int J Hydrogen Energy*. 2011;36:3138-46.

[44] Li K, Wang X, Jia L, Yan D, Pu J, Chi B, et al. High performance Ni-Fe alloy supported SOFCs fabricated by low cost tape casting-screen printing-cofiring process. *Int J Hydrogen Energy*. 2014;39:19747-52.

[45] Xu N, Chen M, Han M. Oxidation behavior of a Ni-Fe support in SOFC anode atmosphere. *J Alloys Compd*. 2018;765:757-63.

[46] Cho HJ, Kim KJ, Park YM, Choi GM. Flexible solid oxide fuel cells supported on thin and porous metal. *Int J Hydrogen Energy*. 2016;41:9577-84.

[47] Dayaghi A, Kim K, Kim S, Park J, Kim S, Park B, et al. Stainless steel-supported solid oxide fuel cell with La_{0.2}Sr_{0.8}Ti_{0.9}Ni_{0.1}O_{3-δ}/yttria-stabilized zirconia composite anode. *J Power Sources*. 2016;324:288-93.

- [48] Zhou Y, Chen T, Li J, Yuan C, Xin X, Chen G, et al. Long-term stability of metal-supported solid oxide fuel cells employing infiltrated electrodes. *J Power Sources*. 2015;295:67-73.
- [49] Lee K, Kang J, Lee J, Lee S, Bae J. Evaluation of metal-supported solid oxide fuel cells (MS-SOFCs) fabricated at low temperature ($\sim 1,000$ °C) using wet chemical coating processes and a catalyst wet impregnation method. *Int J Hydrogen Energy*. 2018;43:3786-96.
- [50] Cho HJ, Park YM, Choi GM. Enhanced power density of metal-supported solid oxide fuel cell with a two-step firing process. *Solid State Ionics*. 2011;192:519-22.
- [51] Waldbillig D, Kesler O. Characterization of metal-supported axial injection plasma sprayed solid oxide fuel cells with aqueous suspension plasma sprayed electrolyte layers. *J Power Sources*. 2009;191:320-9.
- [52] Hedayat N, Du Y, Ilkhani H. Review on fabrication techniques for porous electrodes of solid oxide fuel cells by sacrificial template methods. *Renewable and Sustainable Energy Reviews*. 2017;77:1221-39.
- [53] Myung J-h, Shin Th, Kim S-D, Park H-G, Moon J, Hyun S-H. Optimization of Ni-zirconia based anode support for robust and high-performance 5×5 cm² sized SOFC via tape-casting/co-firing technique and nano-structured anode. *Int J Hydrogen Energy*. 2015;40:2792-9.
- [54] Myung J-H, Ko H-J, Lee J-J, Lee J-H, Hyun S-H. Synthesis and characterization of NiO/GDC-GDC dual nano-composite powders for high-performance methane fueled solid oxide fuel cells. *Int J Hydrogen Energy*. 2012;37:11351-9.
- [55] Somalu MR, Muchtar A, Daud WRW, Brandon NP. Screen-printing inks for the fabrication of solid oxide fuel cell films: A review. *Renewable and Sustainable Energy Reviews*. 2017;75:426-39.
- [56] Haydn M, Bischof C, Udomsilp D, Opitz AK, Bimashofer G, Schafbauer W, et al. Metal Supported SOFCs: Electrochemical Performance under Various Testing Conditions. *ECS Transactions*. 2017;78:1993-2003.
- [57] Lee Y, Park YM, Choi GM. Micro-solid oxide fuel cell supported on a porous metallic Ni/stainless-steel bi-layer. *J Power Sources*. 2014;249:79-83.

- [58] Tucker MC. Durability of symmetric-structured metal-supported solid oxide fuel cells. *J Power Sources*. 2017;369:6-12.
- [59] Meakin J, Hukins D, Aspden R, Imrie C. Rheological properties of poly(2-hydroxy methacrylate) (pHEMA) as a function of water content and deformation frequency. *Journal of materials science Materials in medicine*. 2003;14:783-7.
- [60] Shrivastava A. 3 - Plastic Properties and Testing. In: Shrivastava A, editor. *Introduction to Plastics Engineering*: William Andrew Publishing; 2018. p. 49-110.
- [61] Mazzeo F. Introductory Guide To Using An Ar Series Rheometer Using Rheology Advantage Software. In: Instruments T, editor. 109 Lukens Drive, New Castle, DE 19720, USA: TA Instruments.
- [62] Abd Mutalib M, Rahman MA, Othman MHD, Ismail AF, Jaafar J. Chapter 9 - Scanning Electron Microscopy (SEM) and Energy-Dispersive X-Ray (EDX) Spectroscopy. In: Hilal N, Ismail AF, Matsuura T, Oatley-Radcliffe D, editors. *Membrane Characterization*: Elsevier; 2017. p. 161-79.
- [63] Ananthapadmanaban D. Summary of Some Selected Characterization Methods of Geopolymers. 2018.
- [64] Epp J. 4 - X-ray diffraction (XRD) techniques for materials characterization. In: Hübschen G, Altpeter I, Tschuncky R, Herrmann H-G, editors. *Materials Characterization Using Nondestructive Evaluation (NDE) Methods*: Woodhead Publishing; 2016. p. 81-124.
- [65] Loganathan S, Valapa RB, Mishra RK, Pugazhenthii G, Thomas S. Chapter 4 - Thermogravimetric Analysis for Characterization of Nanomaterials. In: Thomas S, Thomas R, Zachariah AK, Mishra RK, editors. *Thermal and Rheological Measurement Techniques for Nanomaterials Characterization*: Elsevier; 2017. p. 67-108.
- [66] Waldbillig D, Wood A, Ivey DG. Thermal analysis of the cyclic reduction and oxidation behaviour of SOFC anodes. *Solid State Ionics*. 2005;176:847-59.
- [67] Visvanichkul R, Puengjinda P, Jiwanuruk T, Peng-Ont S, Sirimungkalakul N, Ngampuengpis W, et al. Fabrication of alloy foam-supported solid oxide electrolysis cell (SOEC) for hydrogen production. *The 2nd International Symposium on Hydrogen Energy and Energy Technologies (HEET 2019)*. Osaka, Japan2019.
- [68] Myung J-h, Ko HJ, Park H-G, Hwan M, Hyun S-H. Fabrication and characterization of planar-type SOFC unit cells using the tape-casting/lamination/co-firing method. *Int J*

Hydrogen Energy. 2012;37:498-504.

[69] Vu H, Nguyen D, Fisher JG, Moon W-H, Bae S, Park H-G, et al. CuO-based sintering aids for low temperature sintering of BaFe₁₂O₁₉ ceramics. Journal of Asian Ceramic Societies. 2013;1:170-7.

[70] Liou Y-C, Wu C-T, Huang Y-L, Chung T-C. Effect of CuO on CaTiO₃ perovskite ceramics prepared using a direct sintering process. J Nucl Mater. 2009;393:492-6.

[71] Amsif M, Marrero-López D, Ruiz-Morales JC, Savvin SN, Núñez P. Effect of sintering aids on the conductivity of BaCe_{0.9}Ln_{0.1}O_{3-δ}. J Power Sources. 2011;196:9154-63.

[72] Liu S-S, Li H, Xiao W-D. Sintering effect on crystallite size, hydrogen bond structure and morphology of the silane-derived silicon powders. Powder Technol. 2015;273:40-6.

[73] Presto S, Viviani M. Effect of CuO on microstructure and conductivity of Y-doped BaCeO₃. Solid State Ionics. 2016;295:111-6.

[74] Zhang W, Sun C. Effects of CuO on the microstructure and electrochemical properties of garnet-type Li_{6.3}La₃Zr_{1.65}W_{0.35}O₁₂ solid electrolyte. J Phys Chem Solids. 2019;135:109080.

[75] Zhang C, Sunarso J, Zhu Z, Wang S, Liu S. Enhanced oxygen permeability and electronic conductivity of Ce_{0.8}Gd_{0.2}O_{2-δ} membrane via the addition of sintering aids. Solid State Ionics. 2017;310:121-8.

[76] Nicollet C, Waxin J, Dupeyron T, Flura A, Heintz J-M, Ouweltjes JP, et al. Gadolinium doped ceria interlayers for Solid Oxide Fuel Cells cathodes: Enhanced reactivity with sintering aids (Li, Cu, Zn), and improved densification by infiltration. J Power Sources. 2017;372:157-65.

[77] Zhang X, Decès-Petit C, Yick S, Robertson M, Kesler O, Maric R, et al. A study on sintering aids for Sm_{0.2}Ce_{0.8}O_{1.9} electrolyte. J Power Sources. 2006;162:480-5.

[78] Choi H-J, Na Y-H, Kwak M, Kim TW, Seo D-W, Woo S-K, et al. Development of solid oxide cells by co-sintering of GDC diffusion barriers with LSCF air electrode. Ceram Int. 2017;43:13653-60.

[79] Bhaskar Reddy S, Paramanano Singh P, Raghu N, Kumar V. Effect of type of solvent and dispersant on NANO PZT powder dispersion for tape casting slurry. Journal of Materials Science. 2002;37:929-34.

- [80] Maiti AK, Rajender B. Terpeneol as a dispersant for tape casting yttria stabilized zirconia powder. *Materials Science and Engineering: A*. 2002;333:35-40.
- [81] Visvanichkul R, Puengjinda P, Jiwanuruk T, Peng-Ont S, Sirimungkalakul N, Ngampuengpis W, et al. Effect of CuO as Sintering Additive in Scandium Cerium and Gadolinium-Doped Zirconia-Based Solid Oxide Electrolysis Cell for Steam Electrolysis. *Processes*. 2019;7:868.
- [82] Zhu JH, Geng SJ, Lu ZG, Porter WD. Evaluation of Binary Fe–Ni Alloys as Intermediate-Temperature SOFC Interconnect. *J Electrochem Soc*. 2007;154:B1288.
- [83] Moon H, Kang D-W, Park H-G, Hyun S-H. Stress and camber analysis of anode-supported electrolytes by tape-casting and co-firing techniques. *Int J Hydrogen Energy*. 2011;36:10991-7.
- [84] Graves C, Ebbesen SD, Mogensen M. Co-electrolysis of CO₂ and H₂O in solid oxide cells: Performance and durability. *Solid State Ionics*. 2011;192:398-403.
- [85] Teng Z, Xiao Z, Yang G, Guo L, Yang X, Ran R, et al. Efficient water splitting through solid oxide electrolysis cells with a new hydrogen electrode derived from A-site cation-deficient La_{0.4}Sr_{0.55}Co_{0.2}Fe_{0.6}Nb_{0.2}O_{3-δ} perovskite. *Materials Today Energy*. 2020;17:100458.



APPENDICES

จุฬาลงกรณ์มหาวิทยาลัย
CHULALONGKORN UNIVERSITY



จุฬาลงกรณ์มหาวิทยาลัย
CHULALONGKORN UNIVERSITY

APPENDIX A: CALCULATION

A.1 Average grain size

The average grain size of electrolyte's surface from SEM image was calculated by linear intersection method with Image J program.

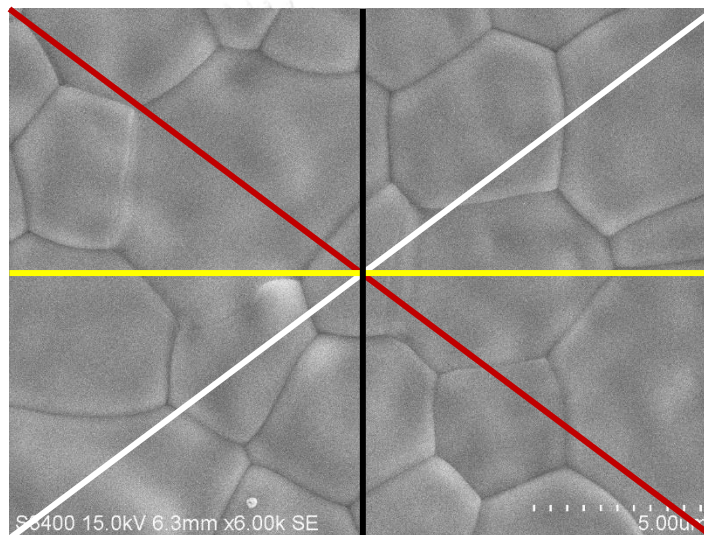


Figure A.1 SEM image of SCGZ with 0.5 wt.% of CuO after sintered at 1573 K, 4 h

White line was 26.60 μm with through 5 grains. Red line was 26.64 μm with through 6 grains. Black line was 16 μm with 5 grains. Yellow line was 21.31 μm with 4 grains. The average grain size was obtained by equation A.1.

$$\text{Average grain size} = \frac{\sum_{i=1}^n \frac{\text{Length of line } n}{\text{The number of grain intersecting the line are counted}}}{n} \quad (\text{A.1})$$

A.2 Relative density of electrolyte densification

The relative density of electrolyte was identified using equation A.2. The actual density was the bulk density that calculated from their measured weight and the volume of electrolyte pellets. The theoretical density was measured with lattice parameters of SCGZ structure. The theoretical density of SCGZ was 5.67 g/cm^3 . A relative density of each sintered electrolyte was reported as Table A.1

$$\text{Relative density} = \frac{\text{Actual density}}{\text{Theoretical density}} \times 100 \quad (\text{A.2})$$

Table A.1 Relative Density (%) of sintered electrolytes

Sintering Temperature (K)	Relative Density (%)	
	SCGZ	SCGZ/CuO 0.5 wt.%
1423	74.52	84.43
1473	80.57	88.7
1523	83.25	90.98
1573	85.07	95.42
1623	86.94	92.31
1673	87.25	90.75

A.3 Ionic conductivity and activation energy of conduction

A.3.1 Ionic conductivity

The ionic conductivity of electrolyte supported SOEC was calculated with the resistance from SOEC range in IV-curve as shown in fig. A.2. This resistance was conducted from slope of IV curve. It was assumed that polarization resistance is much less than the Ohmic resistance.

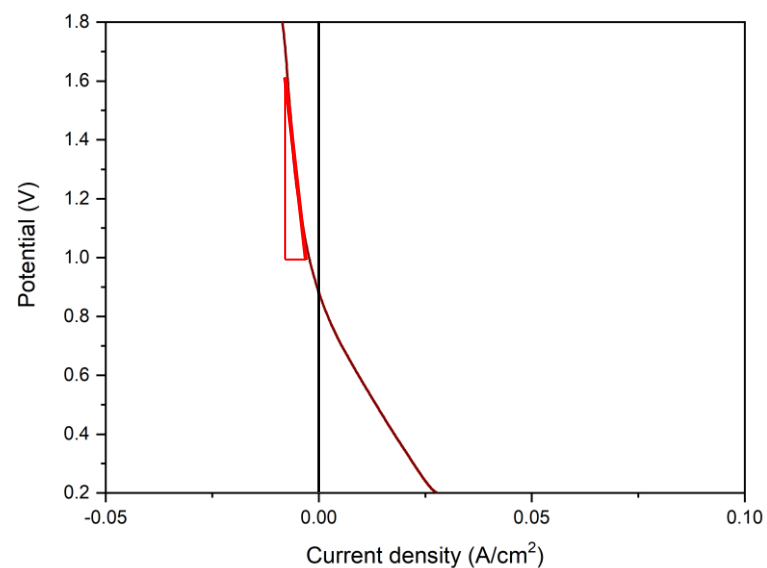


Figure A.2 I-V curves of the SCGZ with 0.5 wt.% CuO electrolyte-supported SOEC conducted at 1073 K under a constant steam to hydrogen ratio (70:30)

The resistance was applied in Arrhenius equation for calculation of Ionic conductivity.

Arrhenius equation:

$$\sigma = \frac{L}{RA} \quad (\text{A.3})$$

When σ = conductivity (S cm^{-1}),

L = cell thickness (cm),

A = area of electrode (cm^2),

A.3.2 Activation energy of conduction

With obtained ionic conductivity in section A.3.1, the conductivity in different temperature was calculated and plotted as shown in Fig. A.3.

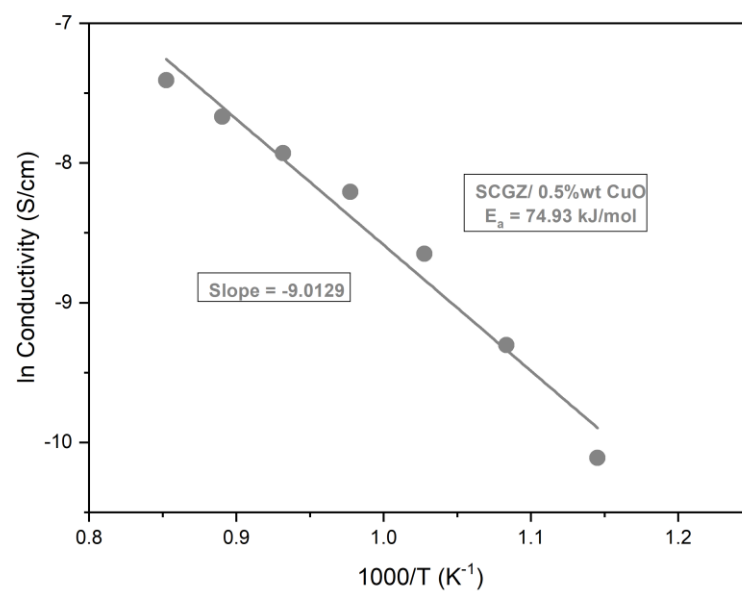


Figure A.3 Activation energy of conduction (E_a) for the SOEC having 0.5 wt.% CuO-added SCGZ electrolyte

This graph related with the activation energy of conduction equation as shown in equation A.4.

$$\ln(\sigma) = \frac{-E_a}{RT} + \ln\left(\frac{A}{L}\right) \quad (\text{A.4})$$

When σ = ionic conductivity (S cm^{-1}),
 L = cell thickness (cm),
 A = area of electrode (cm^2),
 T = temperature (K),
 E_a = activation energy of conductivity (J mol^{-1}),
 R = gas constant ($8.314 \text{ J K}^{-1} \text{ mol}^{-1}$).

It was found that slope of graph equal -9.0192, and then activation energy of conduction was calculated by comparing equation with eq. (A.4). $E_a = -9.0192 \times (-8.314)$ and $E_a = 74.93 \text{ kJ/mol}$

A.4 %Mass changing of fired and reduced foam

The foam was weighted before and after firing and reducing process. Mass changing after each process was determined based on the initial mass of alloy foam support. The mass changing was calculated by equation A.5 and A.6 for firing process and reducing process, respectively.

$$\text{Mass changing after firing} = \frac{\text{Mass of fired foam} - \text{Mass of initial alloy foam}}{\text{Mass of initial alloy foam}} \times 100 \quad (\text{A.5})$$

$$\text{Mass changing after reducing} = \frac{\text{Mass of reduced foam} - \text{Mass of initial alloy foam}}{\text{Mass of initial alloy foam}} \times 100 \quad (\text{A.6})$$

A.5 Thermal expansion coefficient of cathode layer

Thermal expansion coefficient (TEC) of each cathode layers was calculated by weight ratio of Nickle and SCGZ (cermet composition).

For 1st cathode layer, cermet was 75wt.% NiO and 25 wt.% SCGZ. TEC of pure NiO and SCGZ were also 15 and 10.33 10^{-6} K, respectively Therefore, TEC of cathode layer was calculated as following below;

$$\begin{aligned} \text{TEC of 1st cathode layer (} 10^{-6}\text{K)} &= 0.75(15) + 0.25(10.33) \\ &= 13.83 \end{aligned}$$

A.6 Cell degradation rate

Durability test result was shown in fig. A.3. The slope of potential versus operating time was cell degradation rate.

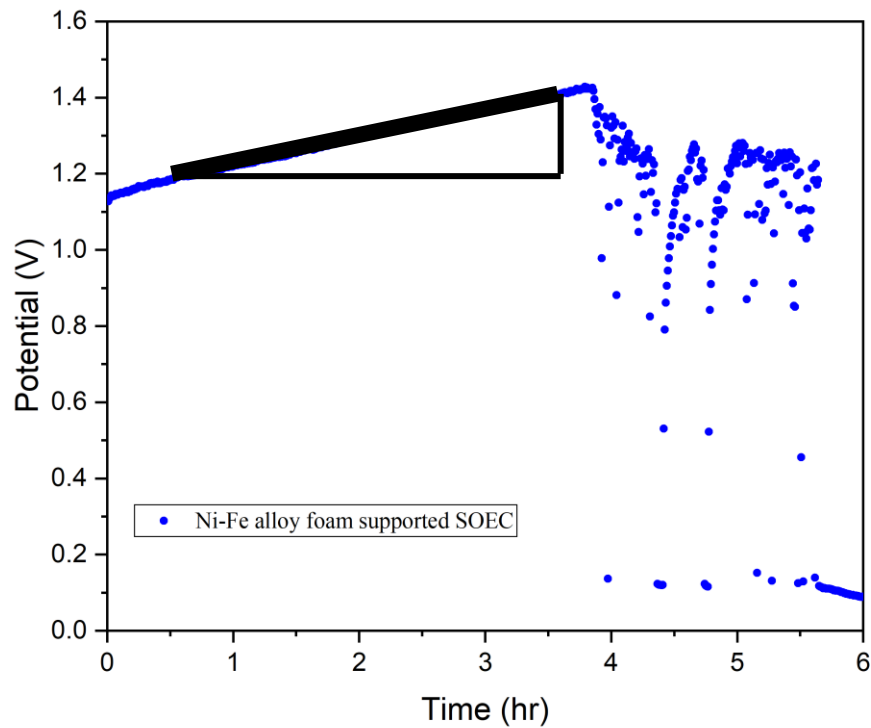


Figure A.3 Durability test of Ni-Fe-alloy-foam supported SOEC operated at 0.9 Acm^{-2} , respectively with $\text{H}_2\text{O}:\text{H}_2 = 70:30$ at 1073 K , 10 h .

A.7 Hydrogen production rate

Hydrogen production rate can be calculated from current consumption in IV-curve result as shown in fig. A.4. The Faraday's law (equation A.7) was applied in this calculation.

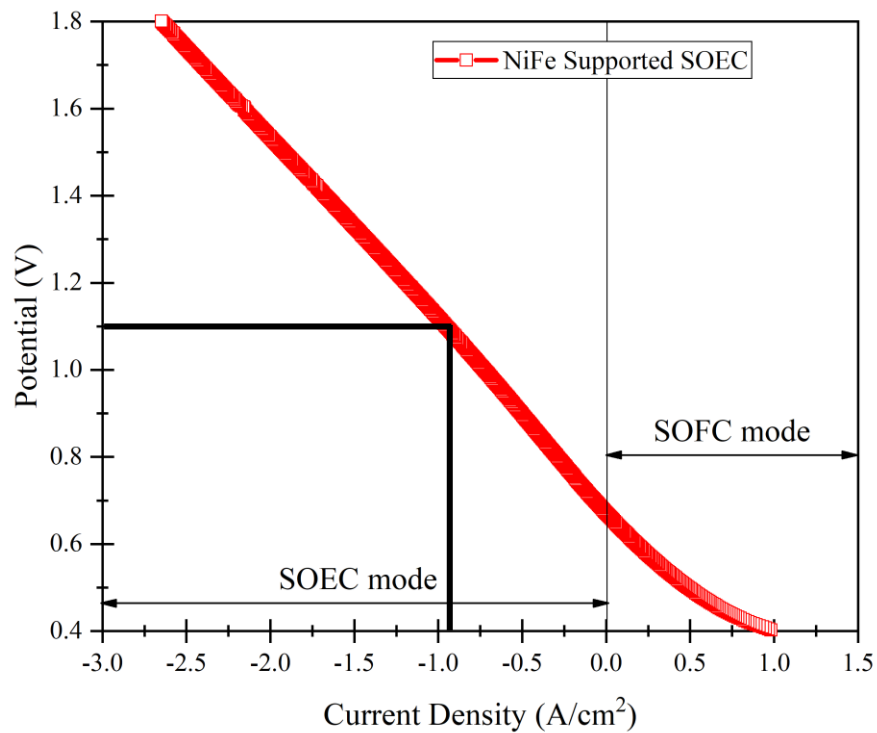


Figure A.4 IV-curve of Ni-Fe-alloy-foam supported SOEC with H₂O:H₂ = 70:30 at 1073 K.

Faraday's laws of electrolysis

$$m = \frac{I}{nF}$$

(A.7)

When m = Amount of mole is generated per area,

I = Current (A or Coulomb/s),

n = Amount of electron is generated in reaction (in this case $n = 2$),

F = Faraday's constant (96,485 C/mol)

At 1.1V, current density was 0.95 Acm^{-2} . Therefore hydrogen production rate was equal; $0.95/(2 \times 96,485) = 4.92 \times 10^{-6} \text{ mol s}^{-1}$

APPENDIX B: SLURRY FORMULA

B.1 Cathode slurries

Table B.1 Cathode slurries formula

Slurry Composition (wt.%)	1 st layer (NiO-SCGZ 1)	2 nd layer (NiO-SCGZ 2)	3 rd layer (NiO-SCGZ 3)
NiO powder	52.50	42.29	32.92
SCGZ powder	17.50	17.71	17.08
Toluene	21.06	28.08	35.10
Ethanol	4.62	6.16	7.70
α -terpineol	0.18	0.24	0.30
PEG 400	4.14	5.52	6.90

B.2 Electrolyte slurry

Table B.2 Electrolyte slurry formula

Material	wt.%
SCGZ/CuO 0.5 wt.%	19.30
Xylene	60.23
Buthanale	16.99
PVPD	0.97
Butvar 98	0.58
PEG	1.93

B.3 Anode slurry

Table B.3 Anode slurry formula

Material	wt.%
BSCF powder	50
α -terpineol	50

VITA

NAME Ramin Visvanichkul

DATE OF BIRTH 29 June 1995

PLACE OF BIRTH Yala, Thailand

INSTITUTIONS ATTENDED Faculty of Engineering, Chulalongkorn Univeristy
Faculty of Engineering, Mahidol Univeristy
Princess Chulabhorn's college, Satun

HOME ADDRESS 36 Phangmuang 1 Rd, Sateng Sub-district, Muang Yala
District, Yala province 95000

PUBLICATION

1. R. Visvanichkul, S. Peng-Ont, W. Ngampuengpis, N. Sirimungkalakul, P. Puengjinda, T. Jiwanuruk, T. Sornchamni, P. Kim-Lohsoontorn. Effect of CuO as sintering additive in scandium cerium and gadolinium-doped zirconia-based solid oxide electrolysis cell for steam electrolysis. Processes. 2019; 7(12):868.
2. R. Visvanichkul, S. Peng-Ont, W. Ngampuengpis, N. Sirimungkalakul, P. Puengjinda, T. Jiwanuruk, T. Sornchamni, P. Kim-Lohsoontorn. Fabrication of alloy foam-supported solid oxide electrolysis cell (SOEC) for hydrogen production. The 2nd International Symposium on Hydrogen Energy and Energy Technologies (HEET 2019), Osaka, Japan, Dec 12-13, 2019